Rotating Discs Actuators:

Direct Numerical Simulation for Turbulent Skin-Friction Drag Reduction

Andrea Levoni, 4447514

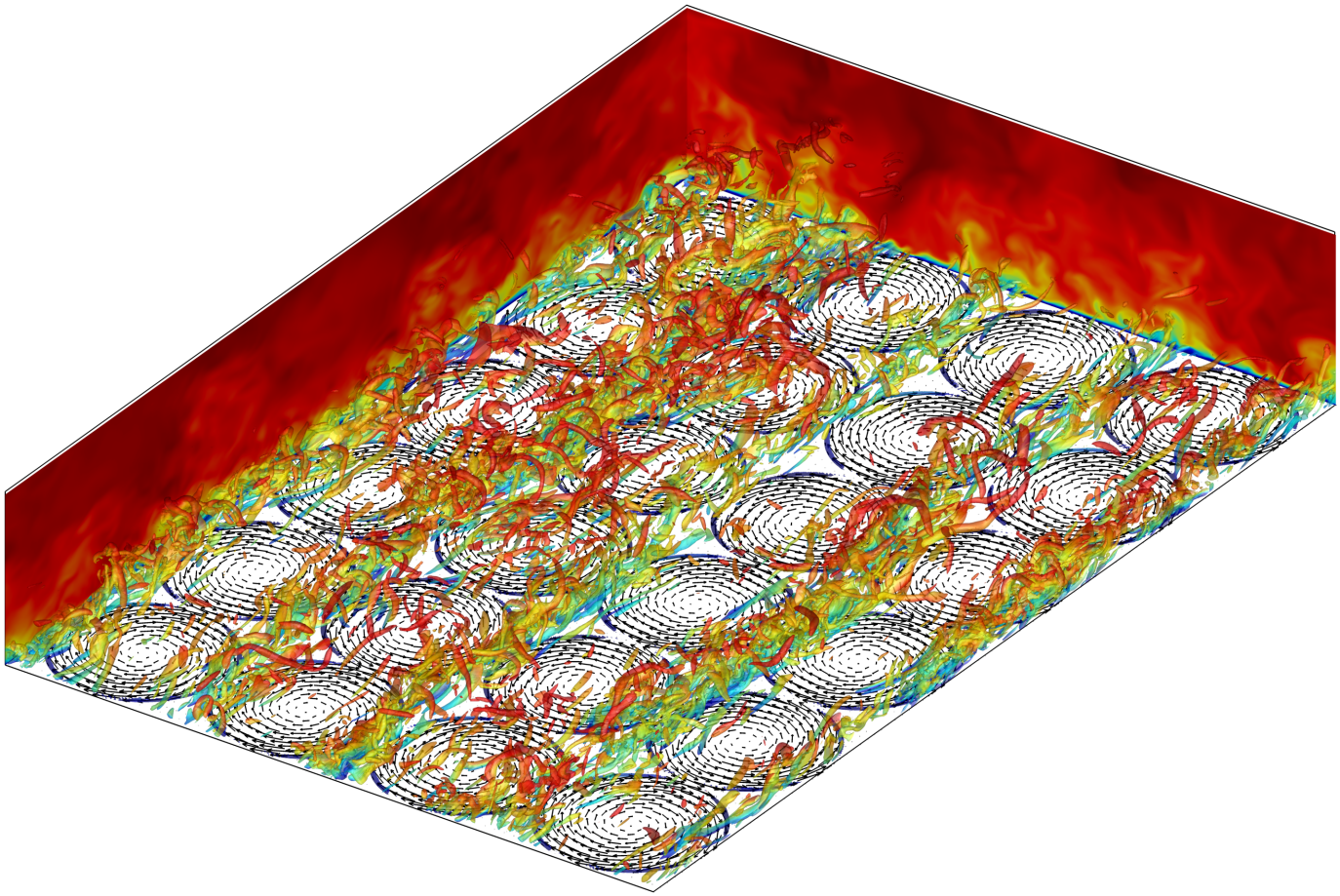

TU Delft

Rotating Discs Actuators:

Direct Numerical Simulation for Turbulent Skin-Friction Drag Reduction

by

Andrea Levoni

to obtain the degree of Master of Science
at the Delft University of Technology,

Student number:	4447514
Project duration:	September 21, 2020 – June 25, 2021
Thesis supervisor:	Dr. D. Modesti TU Delft, supervisor

TU Delft

Acknowledgements

In this few paragraphs I would like to express my gratitude to the many people who were close to me in this six year long period. The memories that remain with me from my time in The Netherlands is something I will forever cherish.

First and foremost, I would like to extend my gratitude to Davide for giving me great support and very valuable feedback all throughout the thesis. Also, I would like to thank my housemates Jacopo, Jasper and Klemens from whom I have learnt a lot, and I couldn't have asked for better housemates. I would also like to thank to everyone close to me, and in particular to my friends Giulio, Enrico, Bart, Arthur, Victor and Katy. I am proud to have spent this time with you all. A hug also goes to my childhood friends from my Modena who, despite the distance have always made me feel right at home whenever I went back to Italy. Thank you Jenny for always being by my side and supporting me through these years.

Finally, I cannot be thankful enough to my whole family, from whom i have always felt love and support whenever i needed it, and to my parents. I will forever be grateful for this opportunity you gave me and for this piece of advice, which I always kept close.

Non chi comincia, ma quel che persevera

(Not those who begin, but those who persevere)

Cover image: three dimensional instant flow visualization of a portion of the domain for the disc on case $D^+ = 546$,$W^+ = 10.5$ at $Re_\tau = 550$.

Abstract

In the aviation, maritime and oil&gas sector, the potential benefit in yearly savings deriving from the reduction of turbulent skin-friction drag through active flow control are estimated in the millions of U.S. Dollars and million tonnes of CO2 emissions. Research in this topic has brought forward numerous techniques, offering enticing drag reduction performance. However, no technique has yet proven to be suitable for large scale application in the aviation sector. A small research stream has been initiated in the field of rotating disc actuators for skin-friction drag reduction. Currently, research on this topic is limited to low Reynolds number numerical simulations, that are not representative of flight conditions.

This thesis project aims at investigating the disc actuator performance in terms of drag reduction and power balance at friction Reynolds numbers higher than current literature on disc actuators. This has been achieved through direct numerical simulations, using an incompressible channel flow solver adapted for the implementation of the disc actuators. In total two disc configurations have been tested at friction Reynolds number Re_τ ≈180, 550 and Re_τ ≈1000. The disc diameter and tip velocity scaled in viscous units are kept constant across the Re_τ range.

The simulation results confirm the positive drag reduction performance observed in previous literature at Re_τ ≈180. With increasing Re_τ, a decrease in drag reduction performance is observed, with skin-friction drag reduction going from 21.6% at Re_τ=180 to 16.01% Re_τ=1000. The net power saving of the disc actuators show small variation with increasing Re_τ, with an optimal net power saving at $Re_\tau = 550$ at $\approx 1.9\%$. Visualizations of local velocity profiles and local time averaged velocity have highlighted the disc influence to be limited in the region below $y^+ < 400$. Thus, the performance of disc actuators at friction Reynolds number higher than Re_τ=1000 should be less influenced by the Reynolds number. Comparison with experimental testing of disc actuators from a parallel thesis study have shown good qualitative agreement between experimental and computational results. Lastly, the consistency in the drag reduction, net power balance result and disc velocity distribution within the boundary layer seem to reinforce the hypothesis that the disc performance scales with the disc diameter and tip velocity expressed in wall units.

The outlook of this research shows that the performance of disc actuators at friction Reynolds numbers more representative for flight applications puts disc actuators on par with other passive skin-friction drag reduction techniques such as riblets in terms of net power saving. However, the reinforcement of the hypothesis that disc performance scales in wall units may result in too small actuators for flight conditions, resulting in more difficult full scale implementation.

Andrea Levoni
Den Haag, June 2021

Intentionally left blank

Table of Contents

Nomenclature

Abbreviations

CFD Computational Fluid Dynamics

CFL Courant-Friedrichs-Lewy number

CO2 Carbon dioxide

DNS Direct Numerical Simulation

FIK Fukagata–Iwamoto–Kasagi

IATA International Air Transport Association

MAC Marker And Cell method

Roman Symbols

B Additive constant in the log law for wall-bounded flows

C Spanwise wall oscillation sinusoidal amplitude

c Annular buffer region width

C^+ Spanwise wall oscillation amplitude, normalized by the viscous length-scale

$C_{f,D,d}$ Disc component of the disc-on case case skin-friction coefficient

$C_{f,D,l}$ Laminar component of the skin-friction coefficient

$C_{f,D,t}$ Turbulent component of the disc-on case case skin-friction coefficient

$C_{f,D}$ Disc-on case skin-friction coefficient

$C_{f,s,l}$ Laminar component of the smooth-wall case skin-friction coefficient

$C_{f,s,t}$ Turbulent component of the smooth-wall case skin-friction coefficient

$C_{f,s}$ Smooth-wall case skin-friction coefficient

$c_{f,x}$ Local skin-friction coefficient

C_f Skin-friction coefficient

C_m Maximum spanwise wall oscillation amplitude

$\mathcal{DR}$ Drag reduction

$\mathcal{DR}_d$ Disc component of drag reduction

$\mathcal{DR}_l$ Laminar component of drag reduction

$\mathcal{DR}_t$ Turbulent component of drag reduction

D Disc actuator diameter

D^+ Disc actuator diameter, normalized by the viscous length-scale

$dr(\%)$ Local drag reduction

f Statistically stationary variable

h Channel half height

h_{rib} Riblet height

L_x Streamwise length of the channel

L_y Height of the channel

L_z Spanwise width of the channel

N_x Number of mesh points in the streamwise direction

N_y Number of mesh points in the wall-normal direction

N_z Number of mesh points in the spanwise direction

$\mathcal{P}_{loc}$ Local distribution of power spent to move the discs with respect to the power required to drive the flow within the channel

$\mathcal{P}_{net}$ Difference between the power saved due to disc rotation, which at constant massflow rate is equal to the drag reduction, and the power spent

$\mathcal{P}_{sp,t}$ Percentage of power spent to move the discs with respect to the power required to drive the flow within the channel

$\mathcal{P}_x$ Power required to drive the fluid in x-direction

p Pressure

p' Turbulent pressure fluctuations

p_d Disc pressure component

q_d^+ In-plane disc velocity magnitude, normalized by the friction velocity

R Disc radius coordinate

R_{disc} Maximum disc radius

Re Reynolds number

Re_τ Friction Reynolds number

Re_b Bulk Reynolds number

s_{rib} Riblet crest spacing

T Spanwise wall oscillation period

t Time

T_{end} End of the time averaging

u_i' Turbulent velocity fluctuations components in the three coordinate directions

u^+ Streamwise velocity, normalized by the friction velocity

u_i Velocity components in the three coordinate directions

u_τ Friction velocity

U_b Bulk flow velocity

u_c Velocity at the center of the channel

$u_{d,i}$ Disc flow velocity component

u^+_{disc} Disc-on simulation velocity, normalized by the friction velocity

u^+_{smooth} Smooth wall simulation velocity, normalized by the friction velocity

$\mathcal{W}$ Power required to move the discs against the viscous resistance of the fluid

W Disc tip velocity

W^+ Disc tip tangential velocity, normalized by the friction velocity

W_{max} Maximum disc tip tangential velocity

$w_{R,t}$ Local disc tangential velocity

x Streamwise direction

x_i Coordinate directions vector

y Wall-normal direction

y^+ Wall-normal distance, normalized by the viscous length-scale

z Spanwise direction

Greek Symbols

α_{rib} Riblet closure angle

ΔU^+ Hama roughness function at $y^+ = 100$

δ_v Viscous lengthscale

κ von Kármán constant

ν Kinematic viscosity

ω Angular velocity of the discs

ω^+ Angular velocity, normalized by the friction velocity

$\Pi\delta_{1,i}$ Body force driving the flow in the streamwise direction

ρ Density

τ Total shear stress

$\tau_{tot_{i,j}}$ Total Reynolds stress

τ_w Wall shear stress

List of Figures

List of Tables

1

Introduction

According to the industry fact sheet published by the International Air Transport Association (IATA, 2019), the yearly worldwide fuel expenditure, shown Figure 1.1 from 2005 to 2019, has risen from 135 to 188 billion US dollars between 2018 and 2019. In the latter year, the fuel consumption of commercial aviation only was equivalent to 96 billion gallons of fuel, equivalent to 914 million tonnes of CO2 emissions. Despite the significant impact of the COVID-19 virus on the commercial aviation sector, pre-pandemic forecasts from ICAO (2019) suggest that this upwards trend in fuel consumption and number of flights will continue. The Paris agreements have set clear objectives that, despite the current technological advancements, will likely not be met (European Commission & Innovation, 2021). Policymakers and aviation regulators are active players in encouraging and funding, among others, fundamental research programs to advance novel technologies to achieve a significant impact on the fuel consumption of the aviation sector (European Commission & Innovation, 2021). Research on skin-friction drag reduction in fluid dynamics has been a particularly active area for research since the 1950s, given the considerable economical and environmental benefits of a successful full-scale implementation. Considering the estimate from Schrauf (2006) that skin-friction drag constitutes $\sim 50\%$ of the total drag for aircraft, it becomes straightforward that a projected 10 % reduction in skin-friction drag can lead to 9.8 billions US dollars in savings for the whole civil aviation industry, as well as a total yearly reduction in CO2 emissions up to 45.7 million tonnes. The benefits of this research are not solely limited to civil aviation. According to Ketut et al. (2017), the yearly fuel consumption for maritime vessels equates approximately 200 to 300 million metric tons of fuel , which is mostly used to overcome skin-friction drag on the ship's hull. In fact, $\sim$90% of the total drag for large vessels is constituted by skin-friction drag (Monty et al., 2016). A successful implementation of a skin-friction reducing device can thus lead to a significant reduction in the price of goods shipped at sea, together with a more positive impact on environment. Lastly, another industry which can significantly benefit from advancements in this field is the oil industry, as most of the energy spent to drive oil inside pipes is spent to overcome the turbulent skin-friction drag with the pipe walls (Keefe, 1998).

1.1 Flow Control

The large push for improving skin-friction drag reduction have contributed to the flourishing of flow control research. Flow control techniques are devised for interaction with the flow in order to obtain a specified goal. In aerodynamics, typical examples of flow control aim at skin-friction drag reduction, delay of separation, noise reduction, delay of transition to turbulence. Gad-el-Hak (2000) provides a comprehensive overview of flow control techniques and devices, drawing a clear distinction of such techniques based on the energy expenditure for their operation, and the control system they employ for their operation. This subdivision is shown in Figure 1.2. Active techniques require an energy input and some actuation mechanism, whereas passive techniques

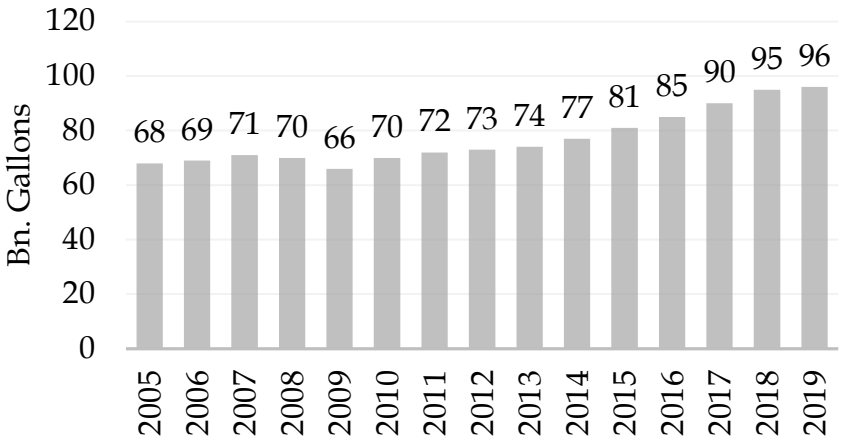

Figure 1.1: Global fuel consumption in billion gallons of fuel from 2005 to 2019 (IATA, 2019).

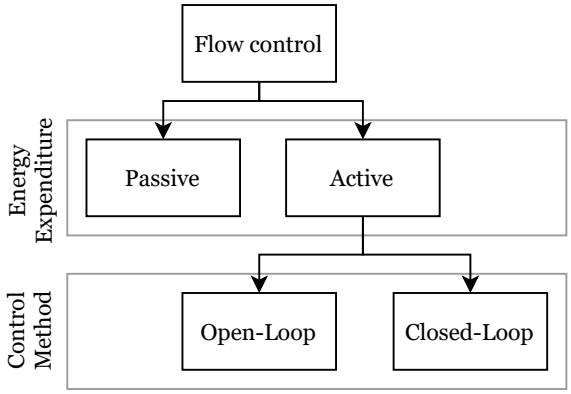

Figure 1.2: Schematics of flow control techniques, adapted from Gad-el-Hak (2000)

do not, and for this reason they are less complex and more attractive.

The following paragraphs will contain a brief revision of three main flow control technologies are relevant to the scope of the thesis: riblets, oscillating walls and rotating discs. This very last technique is also the subject of the study performed and therefore will be given a more special attention.

The most promising passive skin-friction drag reduction technique is constituted by Riblets. These are the sole skin-friction drag reduction method that has successfully been tested on full-scale, yielding a beneficial skin-friction drag reduction effect (Viswanath, 2002). Riblets consist of small grooves aligned with the flow direction, and are characterized by a groove height in the order of micrometers. A schematics of this device is shown in Figure 1.3. Computational and wind tunnel experiments at low Reynolds numbers have shown skin-friction drag reductions up to 12% (García-Mayoral & Jiménez, 2011; Raayai-Ardakani & McKinley, 2019; Sasamori et al., 2014; Walsh & Lindemann, 1984). Luchini et al. (1991) highlighted how the sharpness is a primary factor in the skin-friction drag reduction performance. Furthermore in its paper Luchini explains that the main working principle is the induction of a slip velocity on the riblets crests. This leads to a reduced shear stress translating to skin-friction drag reduction. Flight test has been performed with this technique on low speed propellers and commercial aircrafts (Viswanath, 2002). Flight testing showed that with a $\sim$ 70% covering of the plane wetted surfaces, 2% total drag reduction was achieved through fuel consumption calculations (Szodruch, 1991). This value is in line with the expectations as the skin-friction drag reduction decreases with Reynolds number. Further studies on different configuration of riblets were performed

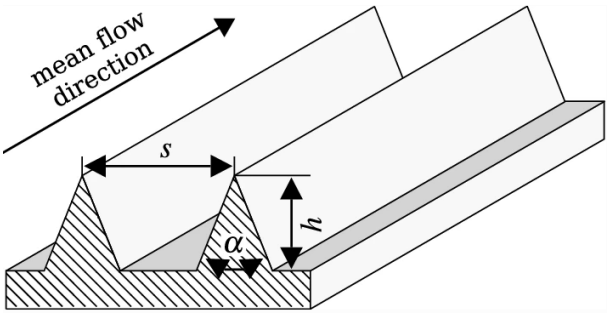

Figure 1.3: Schematics of riblets cross section, with crest spacing s (s_{rib}), groove height h (h_{rib}) and closure angle α (α_{rib}). Extracted from Gatti et al. (2020)

on converging-diverging or 'herringbone' riblets (Benschop & Breugem, 2017), as well as sinusoidal riblets (Sasamori et al., 2014), also showing promising results. Despite the successful drag reduction performance, one of the major drawbacks of this technique is the difficulty in manufacturing micrometer scale grooves (Bechert & Reif, 1985). Furthermore the sensitivity of the riblets performance to dirt accumulation in the grooves and the damage to the crests (Bechert & Hage., 2006; Robert, 1992) prevented their industrial use so far.

Active closed-loop flow control techniques for skin-friction drag reduction are not yet fully developed and have not reached real world implementation yet. Wall normal transpiration was initially proposed by Choi et al. (1994). Only tested in a computational setting and making use of ideal sensors and ideal actuators at the wall, this technique applied opposition control to inhibit the formation of low speed ejection and high speed sweeps through a combination of blowing and suction to counter these velocity fluctuations. The effectiveness of this control system however depends heavily on the sensor and actuation algorithm, which are still not yet fully developed. Although still far from real world application, the technique proposed by Choi et al. (1994) shows that closed-loop control is, at least in theory, effective for skin-friction drag reduction.

A significant breakthrough for open-loop flow control has been achieved with introduction of spanwise wall oscillations, with the induction of a sinusoidal wave-like spanwise velocity at the wall. The technique was introduced first by Jung et al. (1992). Imposition of wall oscillation with period T and sinusoidal amplitude $C = C_m \sin(2\pi/\mathrm{T})$, with C_m being the maximum oscillation amplitude, could lead to skin-friction drag reductions of up to 40% (Akhavan et al., 1993; Baron & Quadrio, 1995; Choi et al., 1998). The main working principle is considered by Ricco (2004) to be the superposition of the Stokes layer generated by the spanwise oscillating plate and the turbulent boundary layer which disrupts the turbulence regeneration cycle via manipulation of coherent structures such as streaks and sweeps (Karniadakis & Choi, 2003). Ricco (2004) adds that another mechanism is the tilting effect on the streaks, which are cyclically inclined at an angle in phase with the oscillation of the plate. Parametric computational studies from Jung et al. (1992) in turbulent channel flow settings and experimental observations from Choi et al. (1998) have shown that the skin-friction coefficient reduction is dependent on the viscous unit scaled wall speed $C^+ = (\Delta z^+/2)\,\omega^+$, where z^+ is the spanwise displacement and ω^+ is the viscous scaled angular velocity of wall oscillations. They reported a skin-friction drag reduction up to 40% at friction Reynolds number $Re_\tau = 180$, which is defined as $Re_\tau = hu_\tau/\nu$, where h is the turbulent channel half height, u_τ is the friction velocity and ν is the fluid kinematic viscosity. Further investigations into the skin-friction drag reduction and power balance were performed by Quadrio (2004), who tested 37 computational cases where the two main parameter are independently varied, while also accounting for power savings. The power balance shows a net saving of 7.3%, however this balance does not account for power losses in the motors

or mechanical friction and wall inertia, which may be crucial factors harming the feasibility of this technique for full scale applications. Although pipe applications are possible due to the circular nature of the wall boundaries (Choi & Graham, 1998), wall applications are still not fully researched.

Disc actuators are the main focus of this thesis study. This technique has been first introduced by Keefe (1998). The setup of this technique consists in an array of discs of diameter D mounted flush to a flat surface, each driven by a motor and with tip velocity $W = D\omega/2$, where ω is the disc angular velocity. Spanwise adjacent discs rotate in the same direction, with alternating direction of rotation in the streamwise direction. An image of the setup is shown in Figure 1.4.

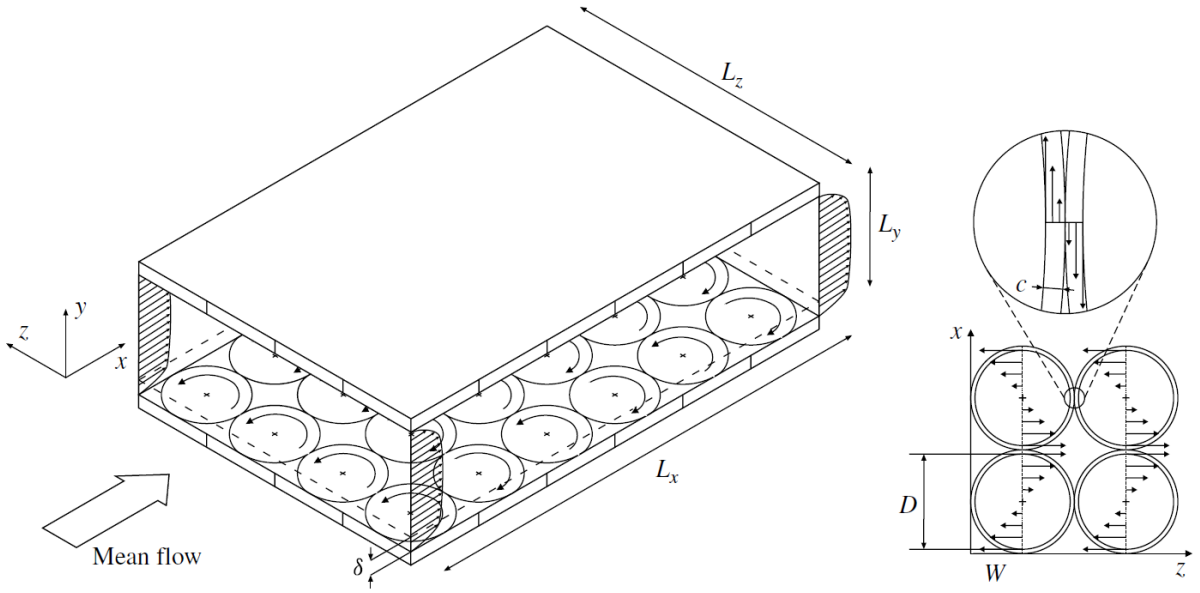

Figure 1.4: Schematics of rotating discs arrangement in the simulations. Extracted from Ricco and Hahn (2013)

Keefe's initial concept sought to implement a closed-loop control technique with skin-friction sensors on the plate, however his proposal was lacking control methods and results. This led to little to no research on the topic until a study from Ricco and Hahn (2013) 15 years later. The authors performed computational simulations on a variant of the system envisaged by Keefe. In the setup from Ricco and Hahn, the discs would rotate at a fixed angular velocity, with an open-loop control system that does not require a shear stress sensor. Ricco and Hahn (2013) performed a parametric study based on Direct Numerical Simulations (DNS) of the disc array placed in turbulent channel flow at friction Reynolds number $Re_\tau = 180$. The authors varied the diameter of the discs and the disc tip velocity independently, obtaining a 2 dimensional map for the skin-friction drag reduction. The authors found an optimum skin-friction drag reduction at 23% for non-dimensional disc diameter $D^+ = 801$ (normalized by δ_v) and non-dimensional tip velocity $W^+ = 10.2$ (normalized by the friction velocity u_τ). A map of their drag reduction performance is presented in Figure 1.5.

In their investigations, Ricco and Hahn (2013) found that for fixed tip velocity, a positive reduction in drag is only achieved beyond a threshold. With a fixed diameter instead, skin-friction drag reduction increases with W^+. The optimal net power balance of 10% is found for slightly different D^+ and W^+ than the drag reduction optimum. Observations from Ricco and Hahn (2013) show that the effects of disc rotation seems to reduce the intensity of low speed streaks as they travel along the discs central part and are less affected when travelling over the stationary

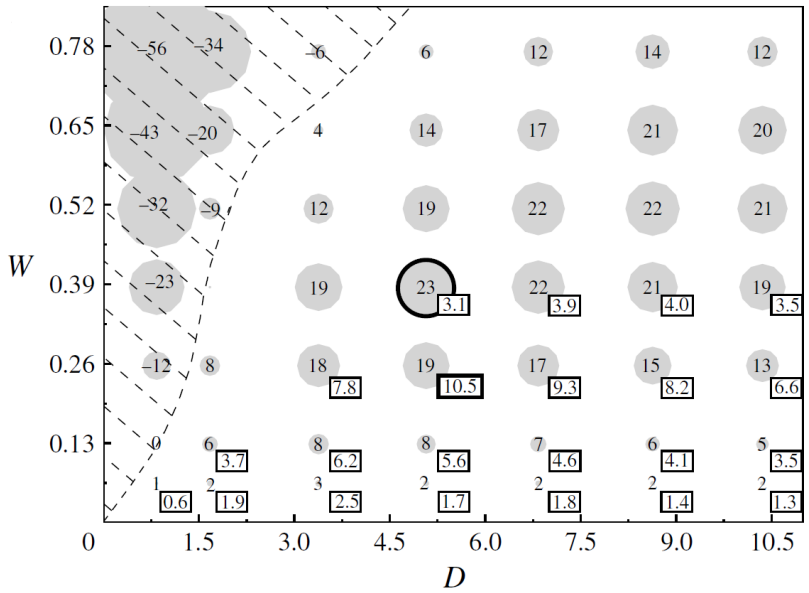

Figure 1.5: Drag reduction map for disc tip velocity W and disc inner diameter D. The grey circles size are proportional to the drag reduction achieved in that point. The values in the squares show the positive power balance outputs. The hatched region outlines combinations leading to drag increase. Extracted from Ricco and Hahn (2013)

plate in between discs. By use of the Fukagata-Iwamoto-Kasagi identity (Kaoru et al., 2002), the authors show that the drag reduction is mostly driven by the reduction in turbulent stresses, whereas the disc-flow stresses are responsible for a small drag increase. The major contribution to these disc stresses comes from the inter-disc structures which appear in the gap between adjacent discs. Wise and Ricco (2014) provide a discussion of the roles of the disc boundary layer and of the inter-disc structures in the drag reduction mechanisms. Figure 1.6 shows the two principal drag reduction effects in disc flow and their scaling.

Firstly, the disc boundary layer forms a high shear rate region. It is possible to approximate the effect of this quantity using laminar analysis, where Wise and Ricco (2014) affirm that this layer resembles the Stokes layer at high actuation frequencies, in a similar manner to what was seen for oscillating walls (Ricco & Quadrio, 2008). Firstly, the rotation of the disc favours the induction of high speed downwards flow from the higher layers towards the disc center (Wise & Ricco, 2014). Centrifugal forces due to the disc rotation induce additional forcing in the spanwise direction. Furthermore, there is a radial dependence of the forcing amplitude, shown in Figure 1.6 by the shading on the disc: The local effectiveness of the drag reduction is reduced for angles which are not oriented with the streamwise direction, as spanwise oscillations bring about a third drag reduction with respect to streamwise oscillations (Zhou & Ball, 2008). The streamwise vortical structures, as explained by Ricco and Hahn (2013) and Wise et al. (2014) are an indirect product of the disc rotational motion. Wise and Ricco (2014) regard these structures as synthetic jets, directed in positive wall-normal and streamwise directions (Wise et al., 2018). These structures contribute to the retardation of the inter-disc flow with respect to the mean flow, however they result in a detrimental contribution to the drag reduction for the disc flow component.

Wise et al. (2014) perform an additional parametric study where the plate coverage is investigated at Re_τ=180. Their findings show that with reducing the wall area covered by the discs, with a distance between disc centers of $1.5D$ can add 5% additional skin-friction drag

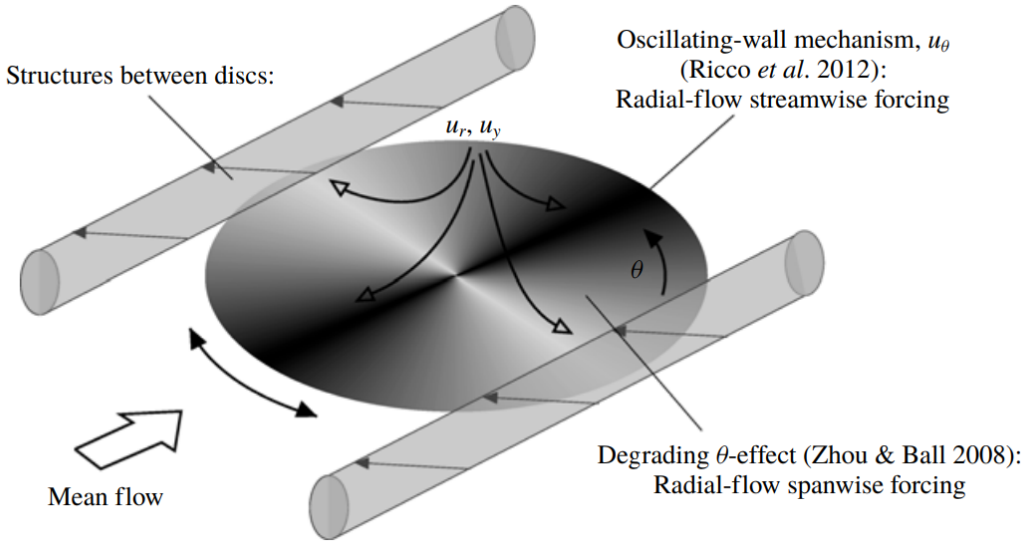

Figure 1.6: Schematics of the drag reduction mechanisms involved in disc actuators for skin-friction drag reduction. Extracted from Wise et al. (2018)

reduction. Furthermore the findings show that the inter-disc structures only occur at the disc edges, where the disc moves against the mean flow. The discs present a series of advantages according to Ricco and Hahn (2013): it's possible to adjust their speed to optimize and target different boundary layer statuses and failure of a disc does not lead to a detriment to the performance of the craft. Next to this upside potential, several drawbacks are also mentioned. The discs present a mechanical complexity that must be accounted for: the influence of fatigue and wear of the system can pose a reliability risk that cannot be yet fully assessed. Furthermore Ricco and Hahn (2013) add that applications of the discs in transonic regime could give rise to high aerothermodynamic heating due to flow reaching local supersonic velocity over the discs.

Further studies explored variants of the rotating disc actuators: Wise and Ricco (2014) has performed tests on a variant of the discs where the rigid discs undergo sinusoidal oscillations, rather than full rotation at a fixed speed. The research involved a parametric study of the disc diameter and the tip velocity, as well as the oscillation period at Re_τ=180. For this study the skin-friction drag reduction reached is 20%, with net energy savings of 6%. Similarly to rotating discs, the skin-friction drag reduction mechanism is a combination of the shearing effect of the boundary layer created by the disc motion onto the wall turbulence and the disc-flow Reynolds stresses produced by the elongated structures that were also seen in the rotating discs by Ricco and Hahn (2013). A potential benefit for oscillating discs is the small displacement of the disc edge, as this allows the filling of the annular gap with an elastic membrane, which can reduce the detrimental effect of the gap in real conditions.

Annular actuators are a variation introduced by Wise and Ricco (2014) and later advanced by Olivucci et al. (2019). In disc actuators, the rotation draws flow towards the wall at the central portion of the discs causing a local increase in skin-friction coefficient. Annular actuators have been observed by Wise and Ricco (2014) to reduce the detrimental effects of this wall-ward velocity. The results show improved drag reduction performance, reaching 20% for an optimal inner-to-outer disc radius ratio of 0.6. The net power saving is also improved by the reduced surface area that needs to be actuated compared to the full discs. Annular actuators have been further studied by Olivucci et al. (2019), who also investigated combinations of this device in combination with opposition control and hydrophobic surfaces. The spanwise velocity

oscillations effectively induce something resemblant to a Stokes layer, with the resulting effect of the central stationary part of the rings being almost re-laminarized (Olivucci et al., 2019). Furthermore, the analysis of the structures forming on the actuator edges showed that these carry a large portion of turbulent kinetic energy, and provide a negative contribution to the skin-friction drag reduction.

Active techniques involving discs for skin-friction drag reduction have shown promising results, as multiple variables have been proposed and simulated computationally. A common remark shared by all authors in the literature about disc actuators is the necessity of investigating the performance at higher friction Reynolds numbers. The main objective of this thesis work is thus to add to the body of knowledge on rotating disc actuators, investigating the performance at a higher friction Reynolds number up to $Re_\tau \approx 1000$ to understand how the beneficial effects of discs scale with Reynolds number.

1.2 Problem Statement

This section provides the description and listing of the research questions and research objectives for the thesis project. Analysis of previous literature on disc actuators highlighted a significant research gap: While many different disc configurations as well as multiple combinations of tip velocity and disc diameter have been simulated, there is a complete lack of information on disc actuator performance with increasing friction Reynolds number, since all the research on disc actuators so far is limited to friction Reynolds numbers $Re_\tau \approx 180$. The project goal is thus:

"To investigate how the skin-friction drag reduction performance of rotating discs scale with increasing Reynolds number.

For this project, the research questions that will be pursued are:

RQ1 How does the skin-friction drag reduction performance of rotating disc actuators change with increasing friction Reynolds number?

RQ2 How does the net power balance performance of rotating disc actuators change with increasing friction Reynolds number?

To answer the research questions mentioned above, Direct Numerical Simulations (DNS) in turbulent channel flow will be carried out at friction Reynolds numbers higher than what previously studied in literature, up to $Re_\tau \approx 1000$, which is unprecedented for this flow configuration.

1.3 Thesis Layout

The layout of the thesis is as follows: Chapter 2 will introduce the theoretical background and lay the foundations for the thesis project. Here basic scaling quantities, averaging operators and flow decomposition will be introduced. Afterwards Chapter 3 will discuss the numerical methodology used for the simulations, as well as introduce the modelling of the disc actuators in the turbulent channel flow setting, as well as the validation of the numerical code. Chapter 4 will present and discuss the results of the simulations. Finally, Chapter 5 will draw conclusions and provide answers to the research questions mentioned above. Furthermore, it will provide recommendations for further research on this topic.

2

Theoretical Background

This Chapter will treat the theoretical background which serves as the foundation for the thesis work. First, Section 2.1 will present the incompressible Navier–Stokes equations. Afterwards, Section 2.2 will introduce the concept of Turbulent Channel Flow, together with basic flow quantities and averaging operators.

2.1 Incompressible Navier–Stokes equations

Turbulent flows are characterized by the chaotic motion of fluid particles. Nevertheless the mathematical equations describing this physical process are deterministic. Incompressible flows are governed by the Navier–Stokes equations:

$$\frac{\partial u_i}{\partial t} + \frac{\partial u_i u_j}{\partial x_j} = -\frac{1}{\rho}\frac{\partial p}{\partial x_i} + \nu\frac{\partial^2 u_i}{\partial x_j^2} + \Pi\delta_{1,i}, \tag{2.1}$$

$$\frac{\partial u_j}{\partial x_j} = 0, \tag{2.2}$$

where u_i represents the velocity components in the three coordinate directions x_i=$[x, y, z]$, p the pressure field, ρ the fluid density, ν the kinematic viscosity of the fluid, and $\Pi\delta_{1,i}$ is the body force driving the flow in the streamwise direction. The body force is computed at each time step to maintain a constant mass flow rate in the channel.

2.2 Turbulent Channel Flow

Turbulent Channel Flow is a canonical configuration flow type used to study wall turbulence in computational settings (Pope, 2000). In this configuration, the flow is bounded by two infinitely large parallel walls and flows uniformly in a single direction. This is simulated within a rectangular box domain. No-slip boundary conditions are imposed at the top and bottom walls, while periodic boundary conditions are imposed in the streamwise and spanwise direction.

The domain, as shown in Figure 2.1 has height of $2h$, with the walls located at the top and bottom heights $(y = -h)$ and $(y = h)$, with h being the channel half height. The flow in the channel is homogeneous in the streamwise and spanwise direction. Furthermore statistical symmetry occurs about the mid plane in y.

In a fully developed turbulent channel, the instantaneous flow is chaotic. It is therefore common practice to introduce a statistical visualization of the flow via averaging the incompressible Navier–Stokes equations in the homogeneous spatial directions and in time. The averaging operators defined here and the flow decomposition are necessary for the definition of the averaged

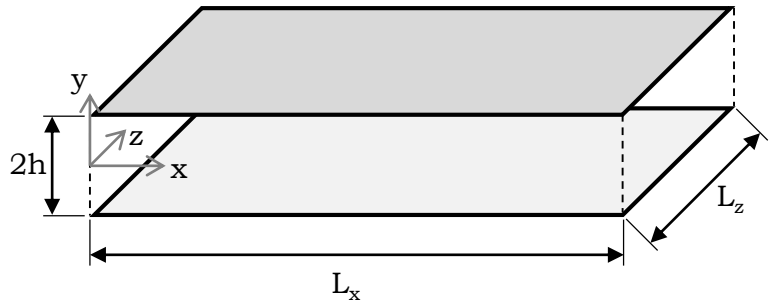

Figure 2.1: Schematics of a turbulent channel flow setup.

Navier–Stokes equations and, in the context of disc actuators, the definition of the disc performance parameters. For a statistically stationary variable $f(x, y, z, t)$ over a time interval from $t = 0$ to $t = T_{end}$, the time average is

$$\bar{f}(x, y, z) = \frac{1}{T_{end}} \int_0^{T_{end}} f(x, y, z, t) \mathrm{d}t. \tag{2.3}$$

Secondly, the spatial averaging operator is expressed as

$$\langle f \rangle (y) = \frac{1}{L_x L_z} \int_0^{L_x} \int_0^{L_z} \bar{f}(x, y, z) \mathrm{d}z \mathrm{d}x. \tag{2.4}$$

Furthermore, through the Reynolds decomposition it is possible to express the velocity flow field $u_i(x, y, z, t)$ as the superposition of the mean velocity $\langle u_i \rangle (y)$, and the turbulent fluctuations $u_i'(x, y, z, t)$

$$u_i(x, y, z, t) = \langle u_i \rangle (y) + u_i'(x, y, z, t). \tag{2.5}$$

Similarly, the same approach can be applied to the pressure field, with $\langle p \rangle (y)$ being the average pressure in the channel and $p'(x, y, z, t)$ the pressure fluctuations

$$p(x, y, z, t) = \langle p \rangle (y) + p'(x, y, z, t). \tag{2.6}$$

In channel flow, custom is to use the Reynolds number based on the definition of bulk flow velocity U_b. This velocity is defined as:

$$U_b = \frac{1}{h} \int_0^h \langle u \rangle \, \mathrm{d}y, \tag{2.7}$$

where $\langle u \rangle$ is the spatially averaged streamwise velocity. This leads to the bulk Reynolds number Re_b

$$Re_b = \frac{2hU_b}{\nu}. \tag{2.8}$$

For a fully developed turbulent channel flow, time–averaged flow quantities are statistically independent in x and z. This means that the mean quantities $\langle . \rangle$ are independent of the streamwise and spanwise position. Hence, the mean momentum equation is expressed as:

$$0 = \nu \frac{\mathrm{d}^2 \langle u \rangle}{\mathrm{d}y^2} - \frac{\mathrm{d}}{\mathrm{d}y} \langle u'v' \rangle - \Pi. \tag{2.9}$$

From this equation, the total shear stress $\tau(y)$ can be defined as:

$$\tau = \rho\nu \frac{\mathrm{d} \langle u \rangle}{\mathrm{d}y} - \rho \langle u'v' \rangle, \tag{2.10}$$

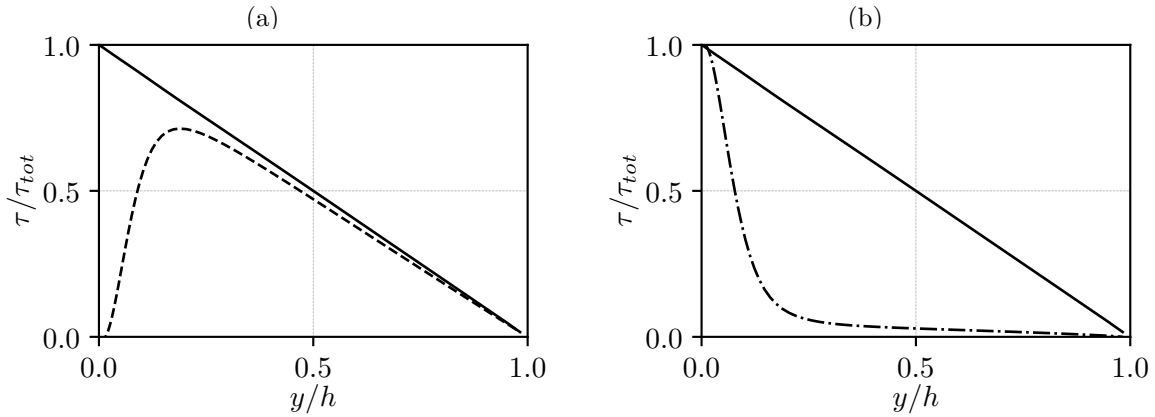

Figure 2.2: Distribution of the viscous (- - -) (a) and Reynolds (-·-·) (b) stresses compared to the total stress (——) within the boundary layer for $Re_\tau = 180$.

Further manipulation of Equation (2.10) (Pope, 2000) allows to show that the total stress is linear:

$$\tau(y) = \tau_w \left(1 - \frac{y}{h}\right). \tag{2.11}$$

Recalling Equation (2.10), the shear stress is the sum of two components. The first one, $\rho\nu \mathrm{d}\langle u\rangle / \mathrm{d}y$ is the viscous stress term. The second term $\rho\langle u'v'\rangle$ is defined as the Reynolds stress. At the wall the Reynolds stress is zero, leaving the viscous stress as the only term in the equation. The wall shear stress $\tau_{(y=0)}$, commonly denominated τ_w is defined as

$$\tau_w = \rho\nu \left(\frac{\mathrm{d}\langle u\rangle}{\mathrm{d}y}\right)_{y=0}. \tag{2.12}$$

From the wall shear stress the skin-friction coefficient C_f can be defined as

$$C_f = \frac{\tau_w}{\left(1/2\rho U_b^2\right)}. \tag{2.13}$$

The coefficient expressed in Equation (2.13) is relevant to channel flow applications, as the bulk flow velocity is used, defined in Equation (2.7).

The region close to the wall is characterized by small eddies in the order of the Kolmogorov length scale. The prevalence of the viscous stresses in the region is significant but only in the near wall region as also shown in Figure 2.2. Firstly, it is possible to define the friction velocity u_τ as

$$u_\tau = \sqrt{\frac{\tau_w}{\rho}}. \tag{2.14}$$

Moreover, it is also important to define a new reference length, called the viscous length scale δ_v. This quantity represent the size of the smallest eddies in the flow:

$$\delta_v = \frac{\nu}{u_\tau}. \tag{2.15}$$

This length scale can be used to derive a new Reynolds number which can be interpreted as the ration between the largest (h) and the smallest (δ_v) length scales in the flow. The Reynolds

number based on this viscous lenghtscales is by definition equal to one, but the friction Reynolds number Re_τ is defined as

$$Re_\tau = \frac{u_\tau h}{\nu} = \frac{h}{\delta_v}. \tag{2.16}$$

Another consequence of the introduction of the viscous length scale is the possibility to scale the physical quantity y by the viscous length scale to obtain the viscous wall distance y^+, which is better suited to distinguish the different sub-layers formed within the boundary layer.

$$y^+ \equiv \frac{y}{\delta_v}. \tag{2.17}$$

Now that all the basic quantities have been defined, it is possible to analyze more in detail the structure of the velocity profile within the wall bounded turbulence. This is important as it is possible to distinguish into different sub-layers depending on the characteristics of the velocity profile and each sub layer is home to a set of different flow occurrences.

The region closest to the wall is defined as the inner layer. This region is characterized by the full dependence of the velocity profile on the viscous length scale. Recalling the definition of y^+, it is possible to define a new non-dimensional velocity value $\langle u^+ \rangle$, which is defined as

$$\langle u^+ \rangle = \frac{\langle u \rangle}{u_\tau}. \tag{2.18}$$

Within the inner layer, different regions can be identified: the viscous wall region, contained within $y^+ < 50$, is defined as the region where the viscous contribution to the wall shear stress is dominant. This can be visually seen in Figure 2.2. In the $y^+ < 5$ zone, the velocity profile is solely dependent on the distance from the wall with the relation $\langle u^+ \rangle \approx y^+$, this region is commonly referred to as the viscous sublayer. This relation is shown in the semi-log plot in x in Figure 2.3.

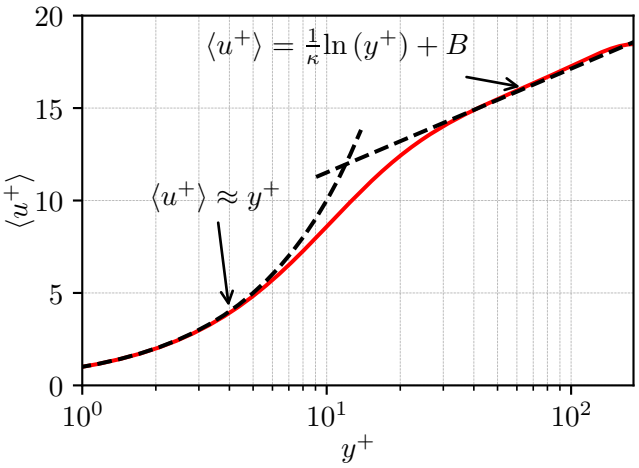

Figure 2.3: Semi-log plot of the velocity profile for a turbulent boundary layer, showing the viscous sub-layer and the log law layer. Extracted from Cousteix (2003)

Further from the wall, as $y^+ > 30$, the velocity profile becomes:

$$\langle u^+ \rangle = \kappa^{-1} \ln(y^+) + B, \tag{2.19}$$

where $\kappa \approx 0.41$ is the von Kármán constant and $B \approx 5.2$ is an integration constant. This logarithmic velocity profile is commonly referred to as the log-law region, and is generally seen to be valid at high Reynolds numbers for $y^+ > 30$ and $y/h < 0.3$. In the semi-log plot, the log law region can be identified in the semi-logarithmic velocity profile shown in Figure 2.3 as a straight line. The gap between the viscous sublayer and the log-law layer is filled by the buffer layer. This region is the most dynamic portion as turbulence production and velocity variance have their maximum there (Perlin et al., 2016).

Within the chaotic motion of the fluid particles, the flow arranges itself into flow structures which have common recognizable characteristics and patterns (Pope, 2000). These patterns are identified as coherent structures. Work from Robinson et al. (1992) classifies the structures seen in simulated turbulent channel flow. For the present literature study, four main coherent structures which are of interest for the present thesis: Low speed streaks, Ejections, high speed sweeps and elongated vortical structures. Low speed streaks are low speed velocity perturbations, located in the near-wall region, at y^+ values between 0 and 10. These streaks are characterized by a spanwise separation of $\approx 100\delta_v$, and can achieve lengths up to 1E3 - 1E4 δ_v (Perlin et al., 2016). Figure 2.4 shows the streamwise instantaneous velocity at a wall-parallel plane at y^+=12 for Re_τ=180. The darker regions identify the location of low speed streaks, which indeed show the separation and length mentioned above.

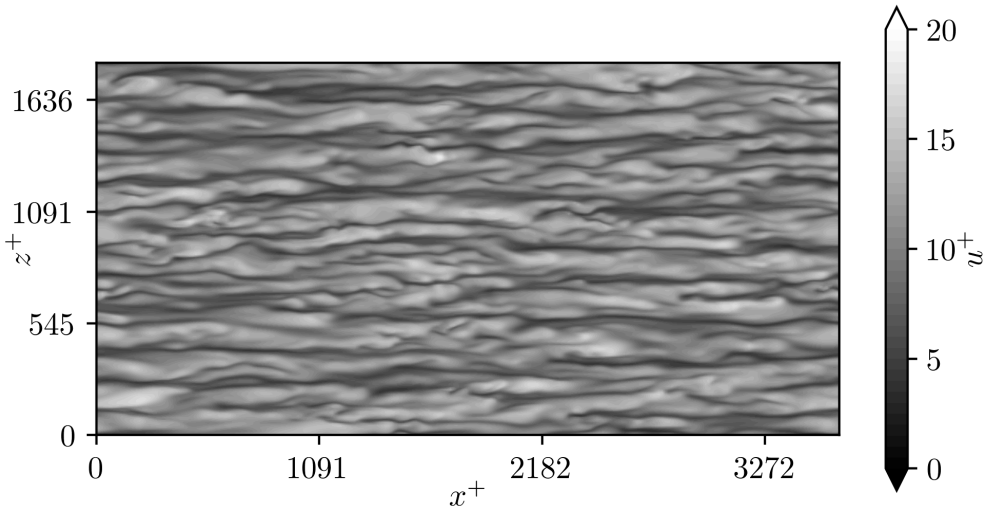

Figure 2.4: Instantaneous flow visualization of u^+ for the smooth-wall simulation at Re_τ=180, taken at a wall-parallel plane at y^+=12, with flow direction from left to right. The darker regions of lower velocity show the location of low speed streaks.

3

Numerical Methodology

This chapter will focus on the description of the methodology followed in the numerical simulations used for this research. It will include a detailed description of the computational setup in Section 3.1, and a verification of the open-source code used for this thesis project, compared against literature data in Section 3.2.

3.1 Computational Setup

Direct numerical simulation relies upon the solution of the Navier–Stokes equation and the resolution of all turbulent scales of motion. Among the other simulation types, DNS is by far the simplest because it does no require any additional models, however its implementation was not possible until advancements in large-scale computing were made (Pope, 2000). Next to being the most accurate, DNS is also the most computationally intensive method of simulation, and as such this method is today mostly limited to basic academic research and to application on canonical flows such as boundary layer, pipe flow and channel flow. In this thesis, the plane channel flow configuration used will be the same as the one used by Ricco and Hahn (2013).

The simulations performed in this thesis project are performed using an incompressible turbulent channel flow solver, which has been previously used to carry out DNS of turbulent channel flow at high Reynolds number (Bernardini et al., 2014). As displayed in Figure 2.1 the solution domain is a rectangular box, of dimensions $L_x \times 2h \times L_z$. The Navier–Stokes equations are solved by applying a variable pressure gradient to the channel in the streamwise direction such that the bulk flow velocity remains constant through the simulation. The equations are discretized using the Marker and Cell (MAC) method, and are solved using the pressure correction method from Harlow and Welch (1965). The time integration uses a low-storage third-order Runge-Kutta scheme, with a continuously adjusting time step to keep the Courant–Friedrichs–Lewy (CFL) number constant at 1.5. The present flow solver is parallelized using the MPI paradigm. The simulations at Re_τ=180 have been run on the TU-Delft aerodynamics cluster, whereas simulations at Re_τ=550 and Re_τ=1000 have been performed on the Dutch national supercomputer Cartesius. The domain was subdivided using a one dimensional slab division for the simulations at Re_τ=180, while for the simulations at Re_τ=550 and Re_τ=1000 a pencil subdivision was used.

The flow solver is modified to implement the discs on the walls by modifying the spanwise and streamwise velocities as boundary conditions. The dimension of the simulated disc actuators stems from the research work in Ricco and Hahn (2013), where the optimum has been found at $D^+ = D/\delta_v$=801, and $W^+ = D/2u_\tau$=10.2. A second disc configuration was selected for the simulations at D^+=546, W^+=10.2, and has been chosen as this disc dimension was analyzed more in detail by Ricco and Hahn (2013). The discs cover the bottom and top channel walls and the size of the computational box is chosen to fit an integer number of discs both in the streamwise and spanwise directions. The disc are arranged in rows of alternate direction of

rotation. A schematic of the disc arrangement on the wall is provided in Figure 3.1. For the disc actuators, the time average $\overline{f}$ introduced in Equation (2.3) indicates the average in time and over the minimum repeating unit of two discs with opposing rotation directions (phase), which is indicated in Figure 3.1 by the red box contoured by the red dashed line.

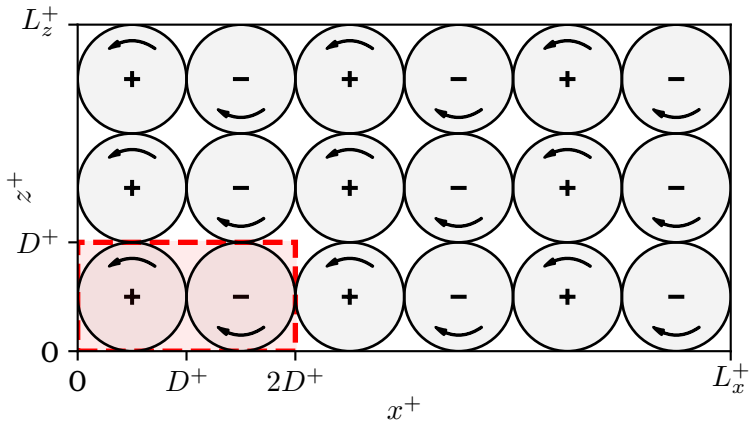

Figure 3.1: Graphics description of the boundary conditions imposed for disc-on simulations. The disc are arranged in rows of alternating counter-clockwise and clockwise adjacent rotating discs, shown in the figures by the arrows and by the + and - sign respectively in the center of the discs. The red shaded region identifies the minimum repeating unit of two aligned discs with opposite sense of rotation.

The tangential velocity of the disc reaches a maximum at the outer diameter, which results in a sharp velocity discontinuity at the location where the disc edge meets the stationary wall. As suggested by Ricco and Hahn (2013), to avoid Gibbs oscillation phenomena at the interface in the simulation results it is useful to include a thin annular region between the disc and the smooth wall modelled as a linear velocity decrease from the maximum tip velocity to zero. The tangential velocity can thus be expressed as a function of the disc radius according to Equation (3.1).

$$w_{R,t} = \begin{cases} 2WR/D & R \leq D/2 - c \\ W(D/2 + c - R)/c & D/2 - c \leq R \leq D/2 \end{cases} \tag{3.1}$$

Here, $w_{R,t}$ is the local tangential velocity, c is the width of the buffer region width expressed in terms of R/R_{disc}, W is the tangential velocity. In accordance to Ricco and Hahn (2013), the suggested width of the annular buffer region is $c = 0.06R/R_{disc}$. Figure 3.2 shows the visualization of the velocity $w_{R,t}/W_{max}$: $w_{R,t}/W_{max}$ increases linearly with $R/R_{disc} < 0.94$. The velocity then decreases linearly to zero in the range $0.94 < R/R_{disc} < 1$.

The domain discretizations in the streamwise and spanwise direction is uniform, with cell sizes defined as $\Delta x = L_x/N_x$ and $\Delta z = L_z/N_z$, where N_x and N_z are the number of mesh points in the streamwise and spanwise direction. In the wall-normal direction the cell spacing is clustered towards the walls using an error function stretching. The details of the simulations carried out is summarized in Table 3.1: the cases are identified by a code formed by a prefix, the value of the approximate Re_τ of the simulation, followed by an underscore and a number referring to the disc diameter. Smooth wall cases are defined with the prefix S, while disc cases are referred to with prefix D. Prefix RH identifies the reproduction of reference simulations from Ricco and Hahn (2013), used for the validation of the flow solver.

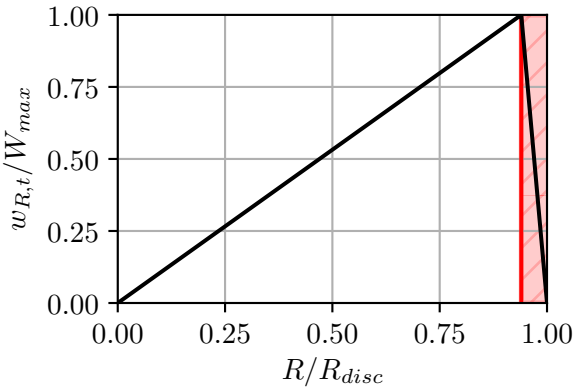

Figure 3.2: Tangential velocity $w_{R,t}/W_{max}$ distribution along the disc radius, with the red shaded region showing the buffer velocity region.

Case	Re_τ	Re_b	D^+	W^+	$\omega h/U_b$	R/h	L_x/h	L_z/h	N_x	N_z	N_y	Δx^+	Δz^+	$\Delta t u_\tau/h$
S180	180	4285	-	-	-	-	20.28	10.14	480	480	128	7.6	3.8	12.62
RH158_8	158	4285	801.0	10.2	0.15384	2.535	20.28	10.14	480	480	128	7.6	3.8	11.03
RH158_5	158	4285	546.0	10	0.23076	1.69	20.28	10.14	480	480	128	7.6	3.8	11.45
D180_8	182	5015	801.0	10.72	0.17528	2.225	17.80	8.90	480	480	128	6.7	3.3	14.55
D180_5	187	5015	545.4	10.46	0.25742	1.515	18.18	9.09	480	480	128	6.8	3.4	14.91
S550	555	15400	-	-	-	-	14.60	7.30	2688	1344	264	2.9	2.9	8.29
D550_8	541	17100	803.0	11.24	0.48715	0.730	17.52	8.76	2400	1200	264	4.0	4.0	10.12
D550_5	551	16950	544.5	10.93	0.71842	0.945	15.84	7.92	2160	1080	264	4.0	4.0	10.41
S1000	1008	30750	-	-	-	-	17.60	8.80	2160	2160	384	8.1	4.0	2.46
D1000_5	1001	33050	550.0	10.59	1.70528	0.275	17.60	8.80	2160	2160	384	8.1	4.0	2.41

Table 3.1: DNS simulations dataset: The first column lists the identifiers for each run. The RH prefix identifies the simulations from Ricco and Hahn (2013). The S and D prefix stand for smooth-wall and disc-on respectively, followed by the Re_τ of the simulation and _5/_8 indicates the size of the disc. Re_τ is the friction Reynolds number. Re_b is the bulk Reynolds number. D^+ is the non-dimensionalized disc diameter. W^+ is the non-dimensional tip velocity. $\omega h/U_b$ is the angular velocity of the discs normalized by the bulk velocity. R/h is the disc radius normalized by the channel half height. L_x/h is the channel length, L_z/h is the channel width. N_x and N_z are the streamwise and spanwise cell numbers respectively. N_y is the number of cells in the wall-normal direction. Δx^+ and Δz^+ are the streamwise and spanwise resolution in viscous units. Lastly, $\Delta t u_\tau/h$ is the averaging time interval.

3.2 Code Verification

The verification of the present flow solver is performed through a comparison with the DNS smooth channel flow simulations performed by Hoyás and Jiménez (2006), at the three simulated friction Reynolds numbers. The parameters compared are the $\langle u^+ \rangle$ velocity profile, and the Reynolds stresses.

Figure 3.3 shows the velocity profile for the three smooth flow simulations, showing a good agreement between the dash-dotted black lines, corresponding to the simulations from Hoyás and Jiménez (2006) and the red line corresponding to the results using the solver. The results shown are in excellent agreement at all Reynolds numbers. A small disagreement can be noticed in Figure 3.3c with a divergence in the wake region, because the reference data are at Re_τ=950, instead of 1000.

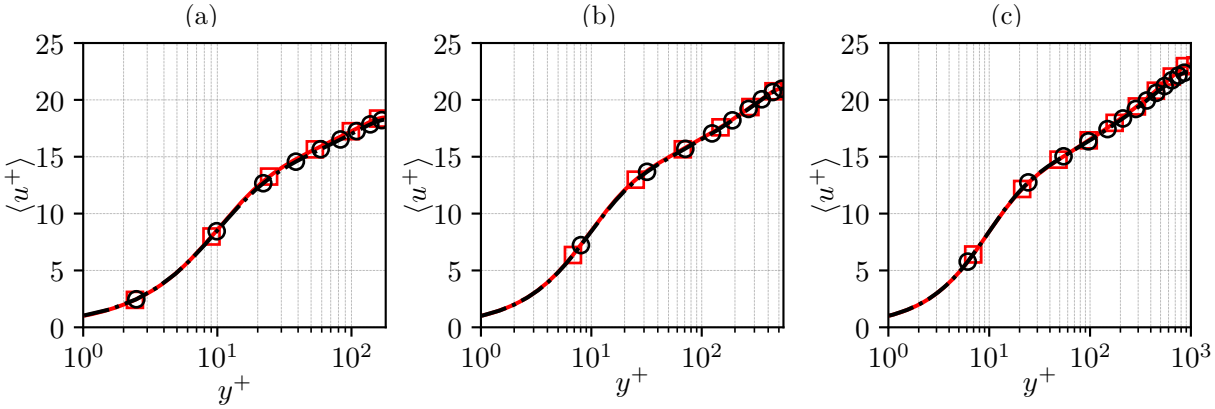

Figure 3.3: $\langle u^+ \rangle$ comparison between DNS data from Hoyás and Jiménez (2006) (-·-·) and the smooth wall results produced by the present flow solver (—) for cases S180 (a), S550 (b), and S1000 (c).

A further comparison is provided in Figure 3.4c, where the Reynolds stresses are reported. Once again there is very good agreement with reference data available in the literature.

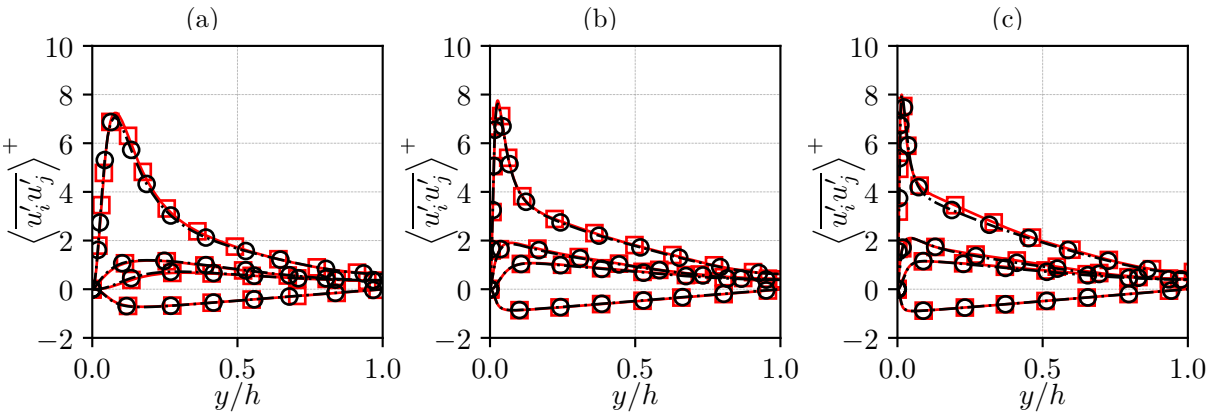

Figure 3.4: Reynolds stress comparison between DNS data from Hoyás and Jiménez (2006) (-·-·) and the smooth wall results produced by the present flow solver (—) for cases S180 (a), S550 (b), and S1000 (c).

The second step in the validation process is a direct comparison with one disc case from Ricco

and Hahn (2013) for disc diameter of D/h=3.38 and tip velocity W/U_b=0.39. The reference simulation has domain size of $L_x/h = 6.79\pi$,$L_z/h = 2.26\pi$ with spatial resolution $\Delta x^+ = 11.5$, $\Delta z^+ = 5.75$, and $N_x = 334$, $N_y = 129$, $N_z = 222$. The present flow solver instead has domain size $L_x = 20.14$, $L_z = 10.14$, with cell numbers $N_x = N_z = 480$, $N_y = 128$, with Re_b=4285.5 and Re_τ=158. Figure 3.5 shows the comparison of the Reynolds stresses between the data from Ricco and Hahn (2013) and the simulation used for validation. The largest difference can be seen in the $\langle\overline{u'u'}\rangle^+$ profile, which appears slightly lower compared to the reference simulation. This can be attributed to a small difference in Re_τ. The other parameters show a good agreement between the reference data and the simulation data. In terms of performance, the calculated drag reduction from the reference simulation is 19.5%. The calculated drag reduction in the validation simulation is 17.9%. The difference between the simulation can be attributed to the small difference in resolution, as well as the computational box size.

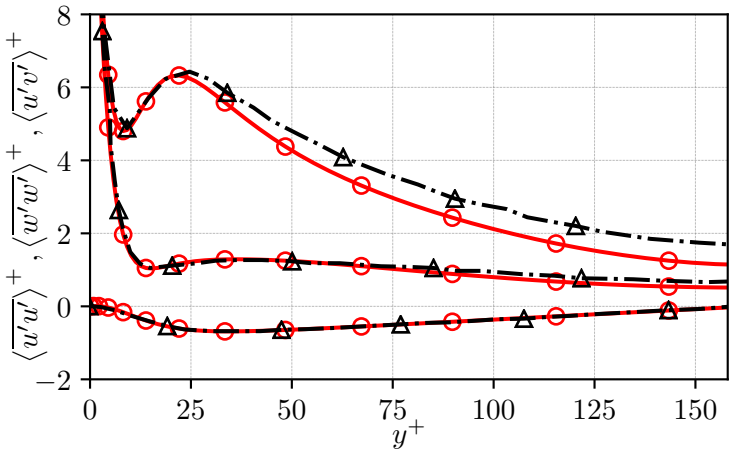

Figure 3.5: $\langle\overline{u'u'}\rangle^+$, $\langle\overline{w'w'}\rangle^+$, $\langle\overline{u'v'}\rangle^+$ comparison between the simulations from Ricco and Hahn (2013) (-·-·), and the smooth wall results produced by the present flow solver (—) for D/h=3.38 and W/U_b=0.39

3.2.1 Mean Momentum Balance

The Reynolds stresses $\langle\overline{u'v'}\rangle^+$ can be used to calculate the mean momentum balance for each simulations. This can provide insight as to whether the simulation is fully converged. The mean momentum balance for the for cases D180_5, D550_5 and D1000_5 is shown in Figure 3.6(a),(b),(c) in y/h scale, and in Figure 3.6(d),(e),(f) shown in Logarithmic y^+ scale. In the same figure, the dash-dotted lines display the mean momentum balance for smooth wall cases S180, S550 and S1000. The mean momentum balance for cases D180_8 and D550_8 are shown in Figure 3.6(g),(h) in outer units, and in Figure 3.6(g),(h) in wall units. The logarithmic scale plots show the crossover point between the Reynolds stress and the viscous stresses, which is at lower y^+ for the disc-on case. Furthermore the distance between the crossover point remains roughly similar across the Re_τ range.

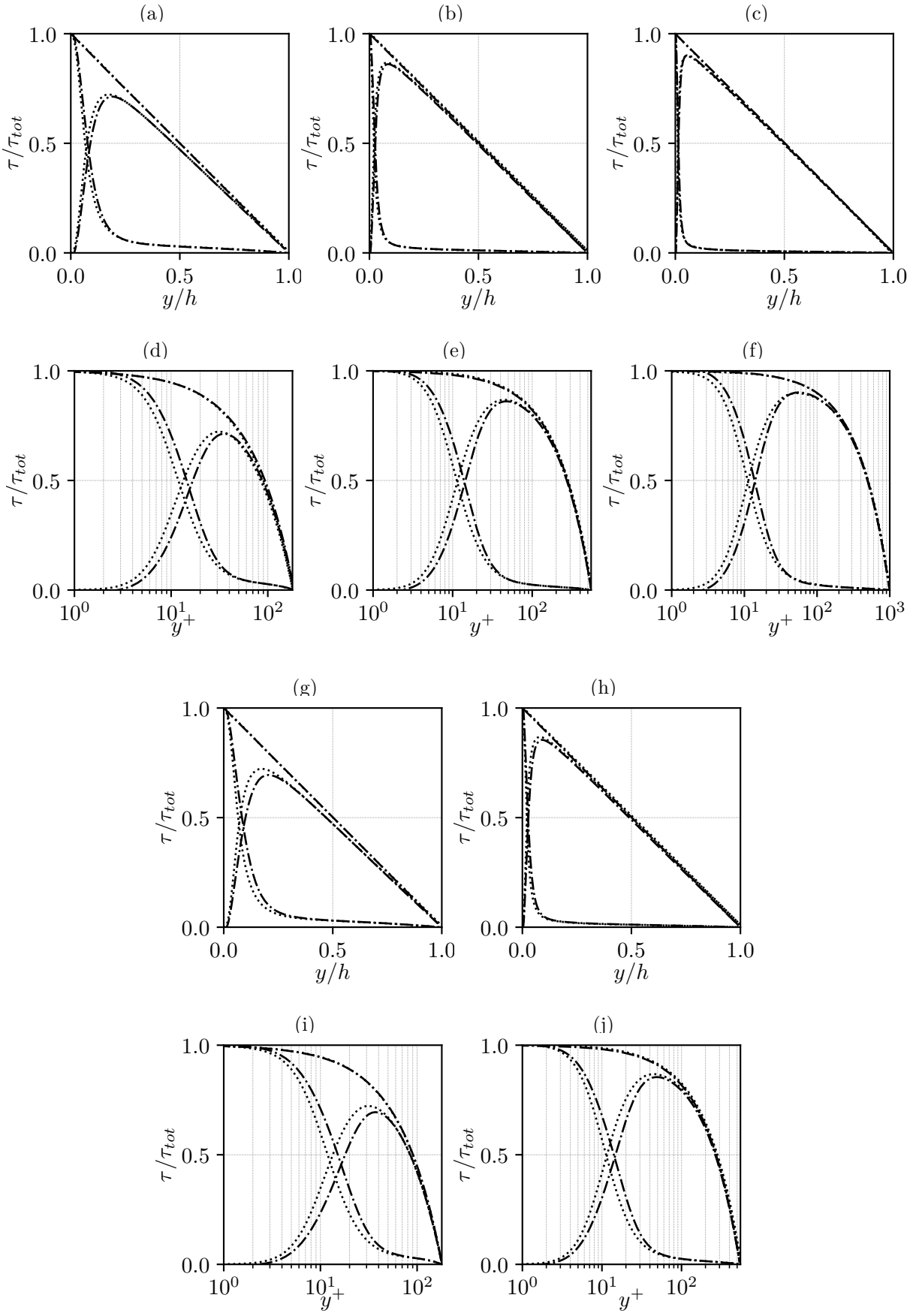

Figure 3.6: Mean momentum balance plots for the disc-on simulations (⋯⋯), and smooth wall simulations (-·-·) plotted both in viscous and outer units: (a),(d) D180_5, S180. (b),(e) D550_5, S550. (c),(f) D1000_5, S1000. (g),(i) D180_8, S180. (h),(j) D550_5, S550.

4

Results Discussion

This chapter presents and discusses the results of the simulations summarized in Table 3.1. First, in Section 4.1 the velocity profiles of the simulation will be presented. Section 4.2 will present global and local skin-friction coefficient results. Drag reduction performance is analyzed in Section 4.3. Analysis of the local disc velocity and deriving quantities is presented in Section 4.4. The Reynolds stresses are shown in Section 4.5. The power balance calculation results are reported in Section 4.6. Lastly, instantaneous flow visualizations are analyzed in Section 4.7. For sake of conciseness, field visualizations of velocity, skin-friction, local power and the analysis of Reynolds stresses are presented only for cases D180_5, D550_5 and D1000_5. All the field visualizations have the flow moving from the left to the right in the positive x direction, unless specified otherwise in the figure caption.

4.1 Velocity Profiles

The first set of results to be analyzed is the time and spatially averaged $\langle u^+ \rangle$ velocity profiles. Figure 4.1 shows the velocity profile for both disc-on simulations, shown by the black patterned lines, and for the smooth wall simulations, shown in red continuous line, for Re_τ=180, 550 and 1000. For all disc-on runs there is a noticeable upwards shift of the log-law region, which indicates a higher center channel velocity, and therefore a lower wall shear stress for the same bulk flow velocity.

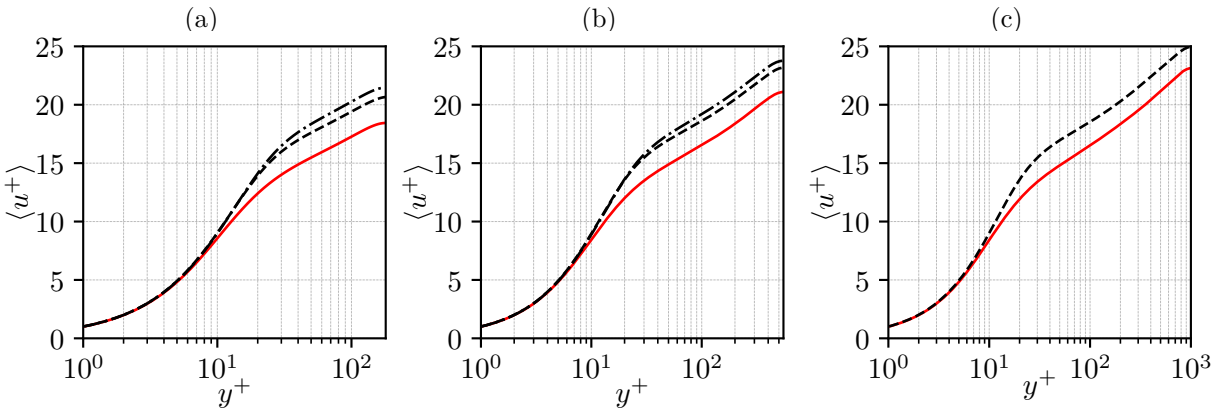

Figure 4.1: $\langle u^+ \rangle$ comparison between smooth wall run (—), D^+=801, W^+=10.5 (- - -) and D^+=546, W^+=10.5 (-·-·) at Re_τ=180 (a), Re_τ=550 (b) and Re_τ=1000 (c).

Comparison between the two disc dimensions at Re_τ=180 and Re_τ=550 shows that the $D^+ = 801$ simulation has a higher upward velocity shift than the $D^+ = 546$ cases. This result confirms

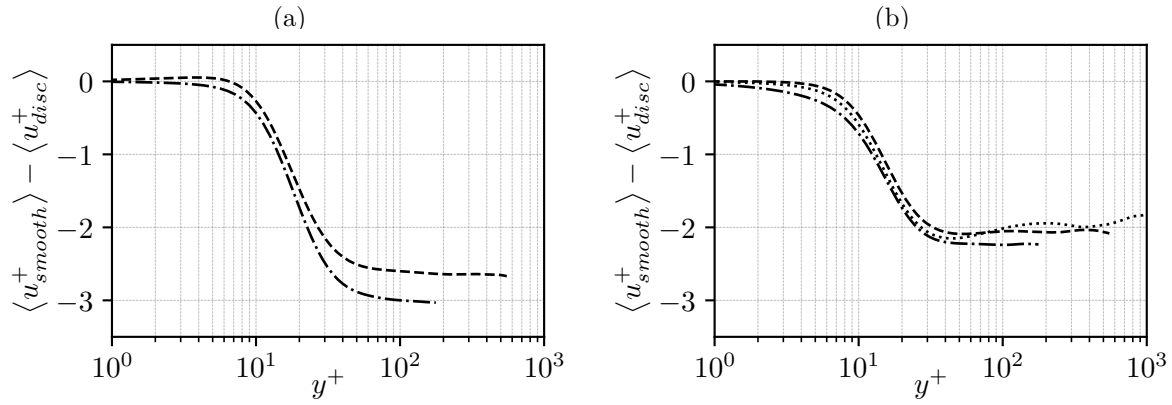

Figure 4.2: Velocity profile difference between the smooth wall velocity $\langle u^+_{smooth} \rangle$ and the disc $\langle u^+_{disc} \rangle$ velocity profiles for D^+=801, W^+=11 (a) and D^+=546, W^+=11 (b) across the Re_τ range: Re_τ=180 (-·-·-), Re_τ=550 (- - -), Re_τ=1000 (·····).

the observations from Ricco and Hahn (2013) at Re_τ=180, who observed lower skin-friction, thus a higher upward shift in the log-law region for disc diameter $D^+ = 801$. Figure 4.2 displays the difference in $\langle u^+_{smooth} \rangle - \langle u^+_{disc} \rangle$ between the smooth wall velocity profile and the disc on velocity profile for the two disc parameters tested for all three Re_τ tested. Near the wall the velocity difference is negligible, but in the log-law region a steady constant value is reached. These results are indicating a positive drag reduction performance for both disc configuration and for all the tested Re_τ values. For both disc diameters, the velocity profile difference decreases with increasing Reynolds number, suggesting that the drag reduction performance deteriorates at higher Re_τ. In the next section, local and total skin-friction coefficient will be analyzed to further characterize the drag reduction performance.

4.2 Skin-friction coefficient

As a further step in determining the disc actuators' drag reduction performance at Re_τ higher than 180, total and local skin-friction coefficient distribution are analyzed. Initially an overview of the total C_f across the Re_τ and Re_b range is provided in Figure 4.3.

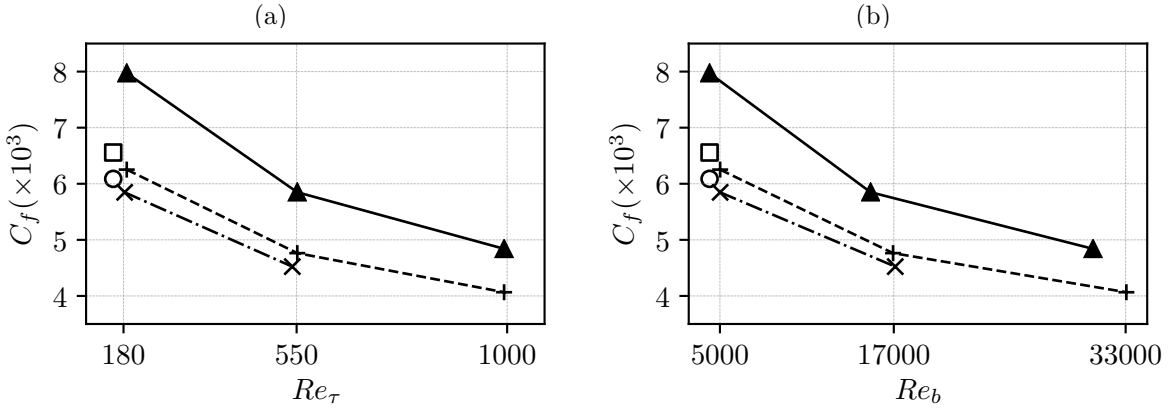

Figure 4.3: Skin friction coefficient for the individual cases across the Re_τ (a) and Re_b (b) range: Smooth wall (——), D^+=546 (- - -), D^+=801 (-·-·-). The empty circle and empty square indicate the skin-friction coefficients for the reference cases of Ricco and Hahn (2013) RH158_8 and RH158_5 respectively.

Smooth wall case results show the natural decrease in C_f with increasing the friction Reynolds number in channel flow. Disc-on cases show a similar descending trend, with a lower C_f than smooth wall results for the same Re_τ and Re_b. Furthermore, the disc-on C_f shows a less steep decline between Re_τ=180 and Re_τ=1000 resulting in a consistent decrease in difference between smooth wall and the disc-on skin-friction coefficients, as Re_τ and Re_b increase.

Time averaging of the velocity field allow to calculate the local streamwise skin-friction coefficient at the wall. The streamwise local skin-friction coefficient is defined as

$$c_{f,x}(x,z) = \frac{2\nu}{U_b^2} \left.\frac{\mathrm{d}\bar{u}}{\mathrm{d}y}\right|_{y=0}. \tag{4.1}$$

Recalling that the surface integral of the local skin-friction coefficient is the total C_f

$$C_f = \frac{1}{2D^2} \int_0^D \int_0^{2D} c_{f,x}(x,z)\mathrm{d}x\mathrm{d}z. \tag{4.2}$$

Figure 4.4 show the local mean streamwise skin-friction coefficient $c_{f,x}$ in the left panels (a), (c) and (e), whereas the panels on the right (b), (d) and (f) show $\left(C_{f,s} - c_{f,x}(x,z)\right)/C_{f,s}$, which is the difference between the smooth wall ($C_{f,s}$) and the local disc-on skin-friction coefficient ($c_{f,x}$). The quantities are shown over the minimum repeating two-disc unit shown in Figure 3.1. The figures on the left provide insight on the topology of the wall shear stress on the discs, whereas the figures on the right allow to visualize locations of the disc where local drag reduction is achieved.

The local $c_{f,x}(x,z)$ show a clear pattern with one maximum and one minimum at two distinct position on the upstream and downstream discs. The location of highest skin friction is found on the quarter-disc region downstream of the disc center, where the streamwise wall velocity component is moving opposite to the channel flow direction. In this area, the disc wall velocity is directed not only against the streamwise component of the flow, but also against the lateral component, induced by the sideways motion of the upstream half of the disc. This results into an area of maximum skin-friction located at $\approx 45^o$ with respect to the z axis. Similarly, a low skin-friction zone is located on the upstream half of the disc, where the streamwise disc motion moves with the mean flow. At this location the disc is moving faster than the fluid layers above, which results in a negative $c_{f,x}(x,z)$ patch, where the flow is effectively separated. Comparing the left panels of Figure 4.4 with the right ones, it becomes clear that the low wall shear stress regions corresponds to areas of high local skin-friction drag reduction.

Across the Re_τ range, the topology of the local skin friction distribution remains mostly unchanged, with the skin-friction extremes tapering down as Re_τ increases. The trend is more evident when extracting the value of $c_{f,x}$ across a x line across the disc centers, shown in Figure 4.5. In this figure one can see that the upstream half of the disc is characterized by low skin-friction coefficient, lower than the smooth wall value for the same Re_τ. The local $c_{f,x}$ reaches a minimum at approximately $1/4D^+$ and is followed by a quasi-linear increase up to a maximum of $c_{f,x}$ at the location where the discs interface each other, in the downstream half of the disc. The pattern is the same on both discs despite the opposite sense of rotation. This is a pure consequence of the symmetric nature of the disc actuators.

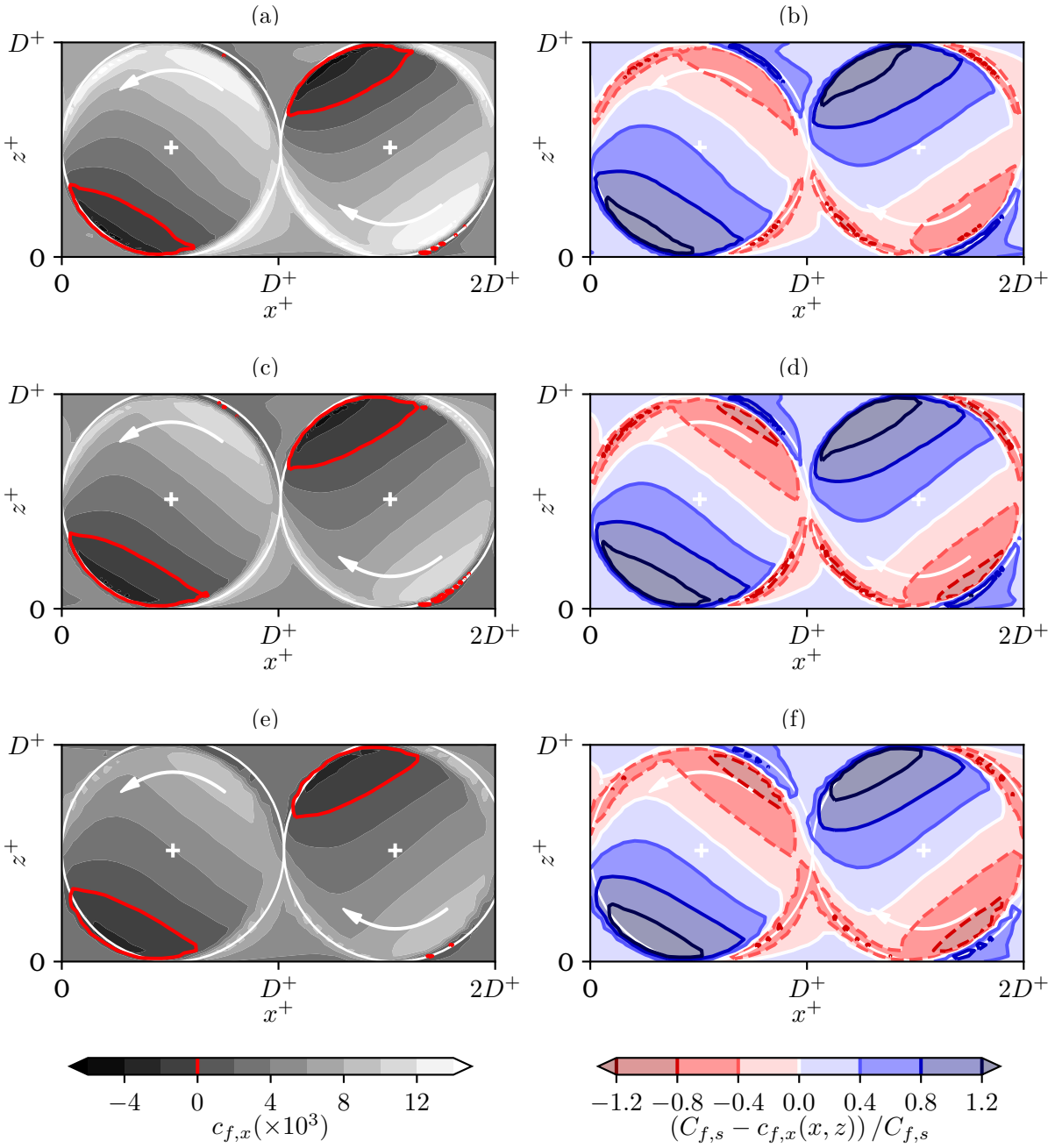

Figure 4.4: Ensemble averaged plots of $c_{f,x}(x,z)$ (a),(c),(e) and $(C_{f,s} - c_{f,x}(x,z))/C_{f,s}$ (b),(d),(f). The first row shows results for the case D180_5, the second D550_5 and D1000_5.

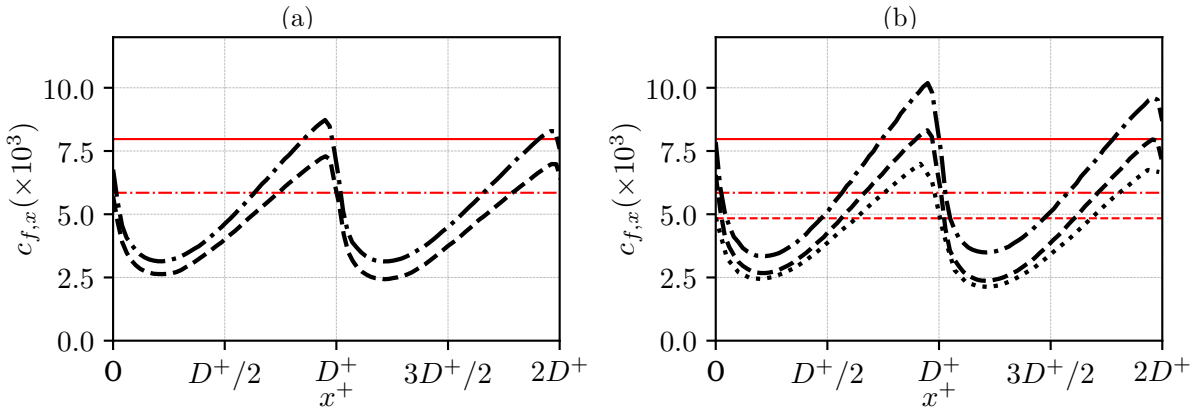

Figure 4.5: $c_{f,x}$ distribution as a function of the streamwise direction, at a spanwise location corresponding to the disc center for $D^+ = 801, W^+ = 11$ (a), and $D^+ = 546, W^+ = 11$ (b) across the Re_τ range: Re_τ=180 (-·-·), Re_τ=550 (- - -), Re_τ=1000 (·····). The red horizontal lines show the smooth-wall skin-friction coefficient for the correspondent Re_τ.

Overall, observations from the local skin-friction distribution suggest that an optimal device at low Re_τ will behave similarly also at higher Re_τ values, albeit with a reduced performance.

4.3 Drag Reduction

Turbulent skin-friction drag is the force stemming from the no-slip condition at the wall. Local skin-friction drag reduction $dr(\%)(x,z)$ is defined within the domain as the percentage difference between the mean smooth-wall skin-friction coefficient and the local axial skin-friction coefficient, defined in Equation (4.1).

$$dr(\%)(x,z) = 100\frac{C_{f,s} - c_f(x,z)}{C_{f,s}}. \tag{4.3}$$

The total drag reduction $\mathcal{DR}(\%)$ is the average of $dr(\%)(x,z)$ over the wall, defined as the percentage variation between the smooth-wall value skin-friction coefficient and the skin-friction when the discs are actuated (Olivucci et al., 2019). Positive values of $\mathcal{DR}(\%)$ indicate drag reduction, whereas negative values correspond to a drag increase.

$$\mathcal{DR}(\%) = \frac{1}{2D^2}\int_0^{2D}\int_0^{2D} dr(\%)(x,z)\mathrm{d}x\mathrm{d}z, \tag{4.4}$$

$$\mathcal{DR}(\%) = 100\frac{C_{f,s} - C_f}{C_{f,s}}. \tag{4.5}$$

Figure 4.6(a) illustrates the drag reduction, calculated with Equation (4.5) for both disc configurations across the Re_τ range. The $\mathcal{DR}\%$ performance worsens consistently with increasing friction Reynolds number. Furthermore, the slope at which $\mathcal{DR}\%$ reduces appears to be dependent on the disc parameters, with cases of disc diameter $D^+ = 801$ worsening at a slightly higher rate than the cases with $D^+ = 546$. Figure 4.6(b) shows the Hama roughness function (i.e. mean velocity shift between smooth and rough wall) at y^+=100, where Negative ΔU^+ corresponds to drag reduction. The dependency on Re_τ of ΔU^+ is similar to $\mathcal{DR}\%$ but with opposite sign.

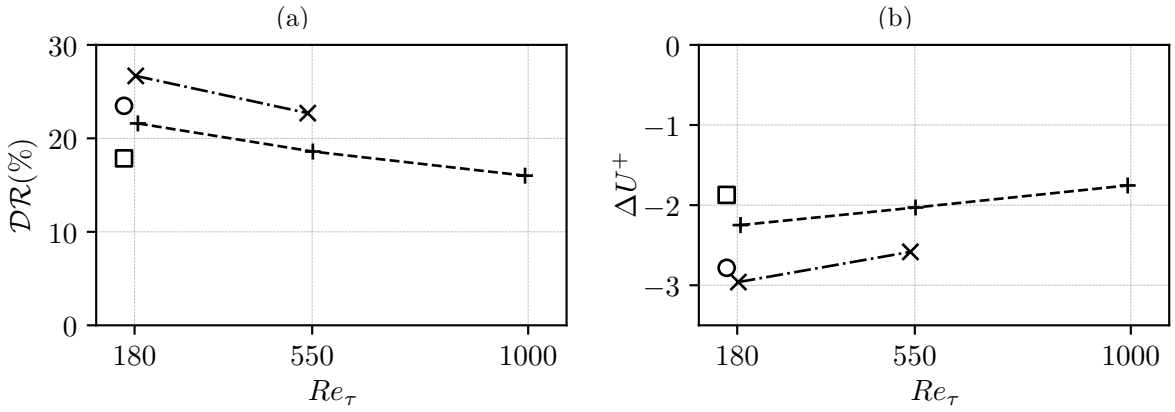

Figure 4.6: $\mathcal{DR}(\%)$ (a) and ΔU^+ at y^+=100 (b) for $D^+ = 801, W^+ = 11$ (-·-·-) and $D^+ = 546, W^+ = 11$ (- - -). The empty circle and empty square indicate $\mathcal{DR}(\%)$ and ΔU^+ for cases RH158_8 and RH158_5 respectively, from Ricco and Hahn (2013)

4.3.1 FIK Identity

Drag reduction can be split into contributions stemming from the disc and turbulent Reynolds stresses in the mean momentum balance equation. Ricco and Hahn (2013) have derived a simple identity to correlate the turbulence statistical quantities with the effect on drag reduction based on the Fukugata–Iwamoto–Kasagi identity (FIK) (Kaoru et al., 2002), adapted for the implementation of disc actuators.

For the derivation of this identity, the velocity flow decomposition shown in Equations (2.5) is adapted with the addition of the disc component of the velocity. The channel velocity flow field $u_i\,(x, y, z, t)$ is now expressed as

$$u_i\,(x, y, z, t) = \overline{u}\,(x, y, z) + u'\,(x, y, z, t)\,, \tag{4.6}$$

where,

$$\overline{u}\,(x, y, z) = \langle u_i \rangle\,(y) + u_{d,i}\,(x, y, z)\,, \tag{4.7}$$

where $u_{d,i}\,(x, y, z)$ is the disc flow component, which becomes zero for the smooth flow simulations. The pressure decomposition is also adapted with the addition of a disc pressure component, calculated in an analogous way to the disc flow velocity component:

$$p(x, y, z, t) = \langle p \rangle\,(y) + p_d(x, y, z, t) + p'(x, y, z, t). \tag{4.8}$$

Now, for the derivation of the FIK identity. Recalling the streamwise momentum equation:

$$\frac{\partial(u)}{\partial t} + \frac{\partial(u^2)}{\partial x} + \frac{\partial(uv)}{\partial y} + \frac{\partial(uw)}{\partial z} = -\frac{\partial(p)}{\partial x} + \nu\left(\frac{\partial^2 u}{\partial x^2} + \frac{\partial^2 u}{\partial y^2} + \frac{\partial^2 u}{\partial z^2}\right). \tag{4.9}$$

Through insertion the disc velocity decomposition of Equation (4.6) and the pressure decomposition of Equation (4.8) in Equation (4.9), followed by averaging in time and homogeneous directions over the two half channels, leads to:

$$\Pi = \nu\frac{\partial}{\partial y}\left[\langle\overline{u'v'}\rangle - \langle u_d v_d\rangle - \frac{\partial\,\langle u\rangle}{\partial y}\right]. \tag{4.10}$$

Ricco and Hahn (2013) further add that the only difference between the original FIK identity and Equation (4.10) is the additional disc Reynolds stress component, leading to the skin-friction

coefficient $C_{f,D}$ for the disc-on case being expressed as

$$C_{f,D} = C_{f,D,l} + C_{f,D,d} + C_{f,D,t} \tag{4.11}$$

Where $C_{f,D,l}, C_{f,D,d}, C_{f,D,t}$ are the laminar, disc and turbulent components of the skin-friction coefficients. These are defined as:

$$C_{f,D,l} = \frac{12}{Re_b} \tag{4.12}$$

$$C_{f,D,d} = -\frac{12}{U_b^2 h}\int_0^h (1-y)\left[\langle u_d v_d\rangle\right] \mathrm{d}y, \tag{4.13}$$

$$C_{f,D,t} = -\frac{12}{U_b^2 h}\int_0^h (1-y)\left[-\left\langle \overline{u'v'}\right\rangle\right] \mathrm{d}y. \tag{4.14}$$

For the smooth wall case total skin-friction $C_{f,s}$ there is no disc component, and only the turbulent ($C_{f,s,t}$) and laminar stress ($C_{f,s,l}$) components, are present. As the Re_b is adjusted to maintain constant Re_τ between the smooth wall and disc-on simulations, the disc-on and smooth wall laminar components will be different. . The smooth flow skin-friction coefficient thus becomes:

$$C_{f,s} = C_{f,s,l} + C_{f,s,t} = \frac{12}{Re_b} - \frac{12}{U_b^2 h}\int_0^h (1-y)\left[\left\langle \overline{u_s' v_s'}\right\rangle\right] \mathrm{d}y. \tag{4.15}$$

Combining Equations (4.11), (4.15) into (4.5) results in

$$\mathcal{DR}(\%) = 100\frac{C_{f,s} - C_{f,D}}{C_{f,s}} = 100\frac{C_{f,s,l} + C_{f,s,t} - C_{f,D,l} - C_{f,D,d} - C_{f,D,t}}{C_{f,s,l} + C_{f,s,t}}, \tag{4.16}$$

Decomposing the numerator in its disc skin-friction component yields:

$$\mathcal{DR}_d(\%) = 100\frac{-C_{f,D,d}}{C_{f,s,l} + C_{f,s,t}}, \tag{4.17}$$

The turbulent component leads to:

$$\mathcal{DR}_t(\%) = 100\frac{C_{f,s,t} - C_{f,D,t}}{C_{f,s,l} + C_{f,s,t}}. \tag{4.18}$$

And finally, the laminar component of the drag reduction becomes:

$$\mathcal{DR}_l(\%) = 100\frac{C_{f,s,l} - C_{f,D,l}}{C_{f,s,l} + C_{f,s,t}}. \tag{4.19}$$

The drag reduction components calculated using the FIK identity are presented in Figure 4.7 for case $D^+ = 801$, $W^+ = 11$in panel (a) and case $D^+ = 546$, $W^+ = 10.5$ in panel (b). The solid line shows the total drag reduction. The disc contribution, indicated by the dotted line, shows a negative (drag increasing) value, which remains stationary for all Reynolds numbers at around -2/-3%. The laminar component is shown in the dashed line, and contributes positively to the drag reduction due to the difference in Re_b needed to maintain Re_τ constant between smooth wall and disc-on simulations. Finally, the dash dotted line instead shows the turbulent contribution to the drag reduction. This component is the main driver behind the negative trend of drag reduction with increasing Re_τ, which according to Equation (4.14) stems from a reduction of the turbulent Reynolds stresses compared to the smooth wall case. The same figure shows the results of the reproductions of the simulations from Ricco and Hahn (2013), as

these simulations are conducted at constant Re_b, the laminar component is zero.

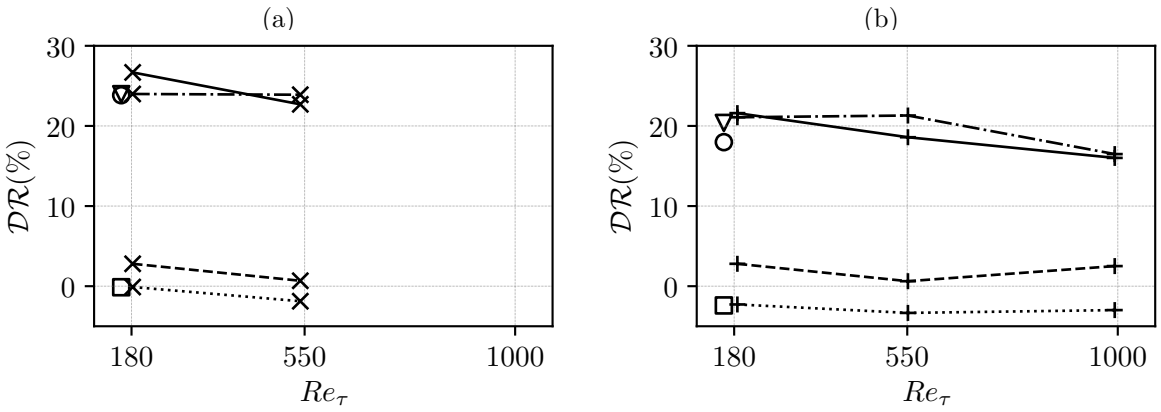

Figure 4.7: FIK Identity decomposition for D^+=801, W^+=11 (a) and D^+=546, W^+=11 (b) across the Re_τ range in terms of $\mathcal{DR}(\%)$ (——), $\mathcal{DR}_d(\%)$ (·····), $\mathcal{DR}_t(\%)$ (-·-·), $\mathcal{DR}_l(\%)$ (- - -), defined in Equations (4.16), (4.17), (4.18) and (4.19) respectively. The triangle, square and circle indicate the total, disc and turbulent components for the reproductions of the constant Re_b simulations from Ricco and Hahn (2013).

The drag reduction results and the skin–friction coefficient results are summarized in Table 4.1.

Case	Re_τ	D^+	W^+	$C_f(\times 10^3)$	$\mathcal{DR}(\%)$	$\mathcal{DR}_d(\%)$	$\mathcal{DR}_t(\%)$	$\mathcal{DR}_l(\%)$
S180	180	-	-	7.971	-	-	-	-
RH158_8	158	801.0	10.2	6.187	23.836	-0.129	23.965	0
RH158_5	158	546.0	10	6.663	17.976	-2.399	20.375	0
D180_8	182	801.0	10.72	5.847	26.681	-0.103	23.988	2.794
D180_5	187	545.4	10.46	6.252	21.598	-2.279	21.082	2.794
S550	555	-	-	5.848	-	-	-	-
D550_8	541	803.0	11.24	4.523	22.697	-1.874	23.894	0.677
D550_5	551	544.5	10.93	4.763	18.590	-3.334	21.301	0.622
S1000	1008	-	-	4.839	-	-	-	-
D1000_5	1001	550.0	10.59	4.066	16.011	-2.983	16.486	2.508

Table 4.1: Summary of the disc runs drag reduction performance. $C_f(\times 10^3)$ indicates the skin-friction coefficient. $\mathcal{DR}(\%)$ is the total drag reduction, as defined in Equation (4.5). $\mathcal{DR}_d(\%)$, $\mathcal{DR}_t(\%)$ and $\mathcal{DR}_l(\%)$ are the disc, turbulent and laminar drag reduction components calculated with the FIK identity in Equations (4.17), (4.18) and (4.19) respectively.

4.4 Local Velocity Distribution

The local velocity distribution is calculated with time averaging of Equation (2.3) applied to the two-disc domain. Field visualizations within the averaging domain are presented and discussed in Subsection 4.4.1. After, groups of time-averaged velocity profiles are shown in Subsection 4.4.2. The aim of this section is to visualize and quantify the extension of the disc influence within the channel.

4.4.1 Field visualizations

The main flow features of the time averaged disc flow are presented here. Ricco and Hahn (2013) as well as Olivucci et al. (2019) have shown the presence of negative disc velocity structures at the disc lateral boundary, where there is a sharp change in wall velocity as the tangential velocities of spanwise-adjacent discs have equal magnitude but opposite direction. These structures are henceforth referred to as inter-disc structures or inter-disc ejections.

These structures are clearly visible in Figure 4.8, which is showing a 3D field view of the two-disc domain. The figure shows Iso-surfaces of $q_d^+ = 2.3$, defined as the magnitude of the in-plane disc velocity, colored by colored by the disc pressure component p_d/τ_w.

$$q_d^+ = \sqrt{\left(u_d^+\right)^2 + \left(w_d^+\right)^2}. \tag{4.20}$$

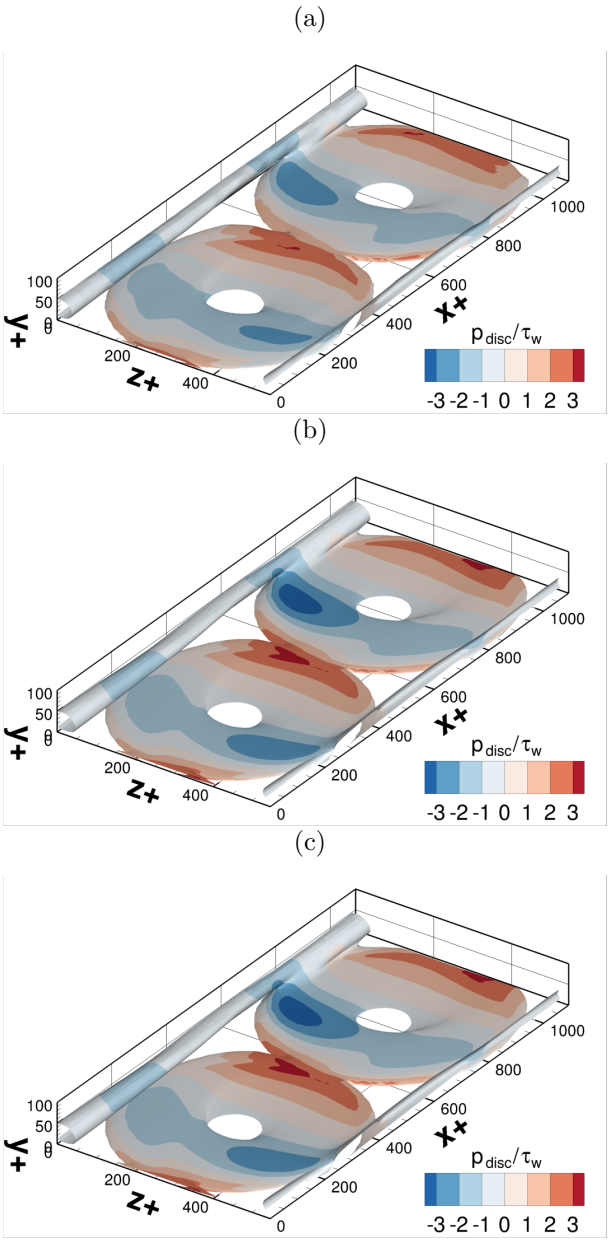

Figure 4.8: 3D iso-surfaces visualization of $q_d^+ = 2.3$, colored by p_d/τ_w, for the runs D180_5 (a), D550_5 (b) and D1000_5 (c).

The iso-surface shape is in line with the observations from Ricco and Hahn (2013), with an annular-shaped structure located right above the discs. Olivucci et al. (2019) argues that these structures are generated by the rotating motion of the actuators induce local diffusive shearing. The inter-disc structures located on each side of the disc actuators are defined in previous literature as ejections, as they are characterized by negative streamwise and positive wall-normal disc velocities. The pressure field displayed on the iso-surfaces also shows lower pressure in the first half of the disc, with a local minimum in the second quarter of the disc, where the disc rotation is going against the flow stream in the channel.

A better visualization of q_d^+ is shown in Figure 4.9(a),(c),(q) where wall-parallel $x-z$ slice through the domain is taken at $y^+ = 5$. The red line identifies where $q_d^+ = 2.3$. The in-plane velocity increase with the disc radius, attaining its minimum at an offset from the disc center, which is marked by a white cross.

Figure 4.9 (b), (d), (f) shows $x-z$ slices of u_d^+ in planes taken at $y^+ = 25$. Looking at the inter-disc structures of Figure 4.8 this coordinate intersects the middle of these structures. It can be noted from the figures across the Re_τ range that the disc flow velocity is positive at the disc center, however in the inter-disc structures the velocity becomes negative. In the same figure, the continuous black line indicates where $q_d^+ = 2.3$ at that y^+coordinate.

Figure 4.10 shows the same u_d quantity for the three Re_τ values tested in viscous units, but on two $z-y$ planes taken through the center of the first disc ($x^+ = D^+/2$) shown on the left and at the interface between the two discs ($x^+ = D^+$) shown on the right. The arrows represent the local w_d^+, v_d^+ velocity field. The same quantity is plotted in outer units in Figure 4.11. The Re_τ=180 and Re_τ=550 cases are plotted to half channel height. The velocity plots for Re_τ=1000 in wall units show that the disc velocity activity is concentrated close to the wall. For this reason, Figure 4.11(e),(f) are plotted in the range $0 \geq y/h \geq 0.6$.

Figures 4.10(a),(b) at Re_τ=180 show the presence of the velocity induced by the discs in the near wall region, below $y^+ \approx$10. In this region the disc induced disc velocity, especially on the center disc slice is extremely active. One disc radius downstream the velocity activity induced by the disc is significantly reduced as the wall is stationary underneath. However a pocket of positive disc velocity remains on the left of the domain in the region $4 \leq y^+ \leq 10$. The positive disc velocity region shown in Figure 4.9 (b) sits above the disc center in the region $15 \leq y^+ \leq 80$, and remains roughly unchanged going downstream.

Figure 4.10 shows the two disc side ejections on each side of the domain, characterized by negative u_d and positive v_d (as shown by the arrows). The center of these structures is located at $y^+ \approx 28$ on each side. For the D180_5 case shown in Figure 4.10(b), four rolling motions are distinguishable. Two small rolling motions sit just on the inboard side of the ejections at the same height as the center of the ejection structure. Further away from the wall and above the disc center, sits a couple of two counter-rotating large rolling motions, each with center at $y^+ \approx 80$. Similar rolling motions have been observed by Olivucci et al. (2019) in their ring actuator study.

The disc flow velocity characteristics remain reasonably similar for the simulations at higher Re_τ, with the heights of the inter-disc ejections remaining at the same levels. The main noticeable difference can be seen in the $x^+ = D^+$ sections, where the region of high positive disc velocity at the disc center becomes progressively smaller.

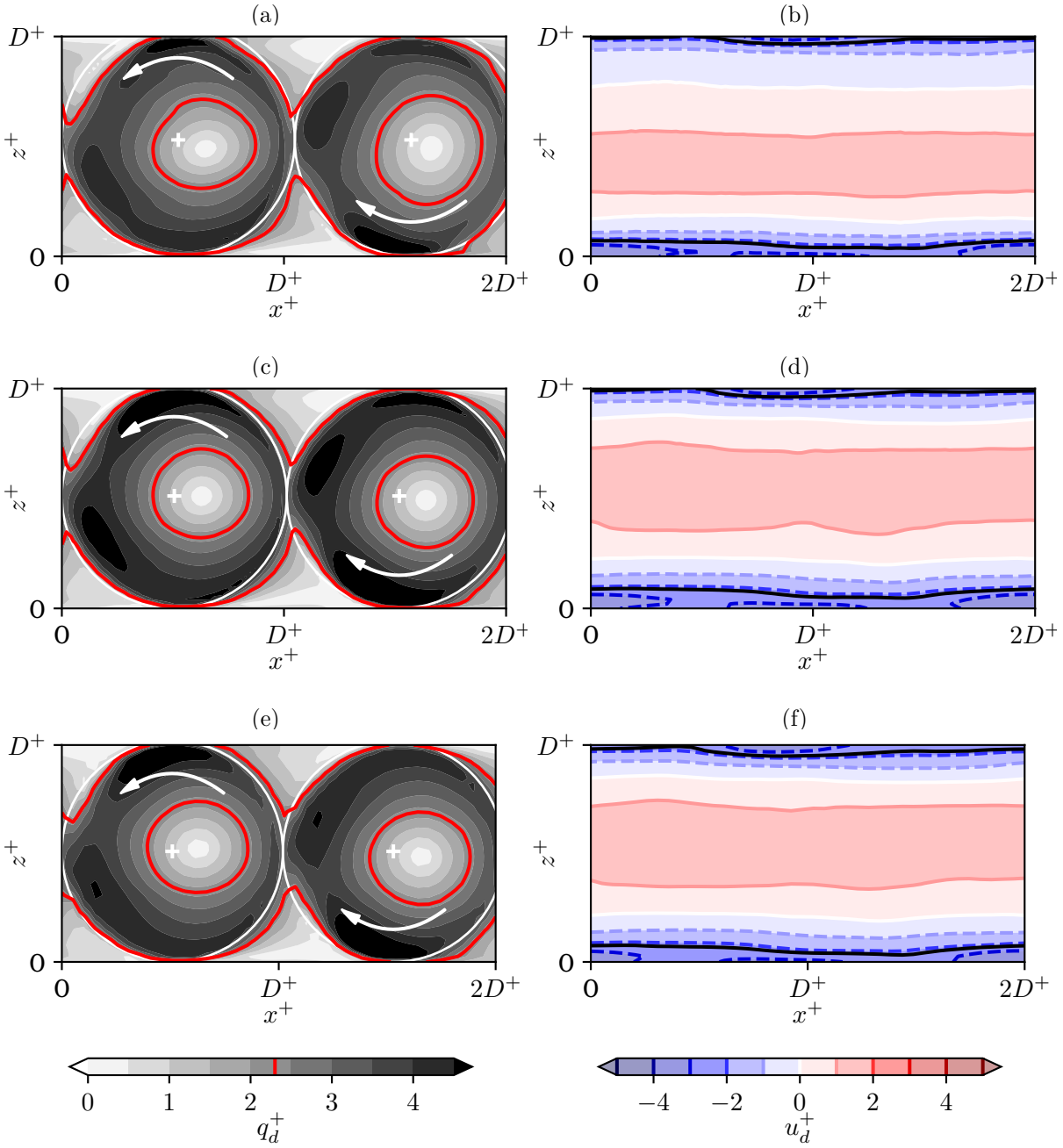

Figure 4.9: Ensemble averaged plots on wall-parallel planes taken at y^+=5 for q_d^+ (left side figures) and at y^+=25 for u_d^+ (right side figures). The rows correspond to cases D180_5, D550_5 and D1000_5 respectively.

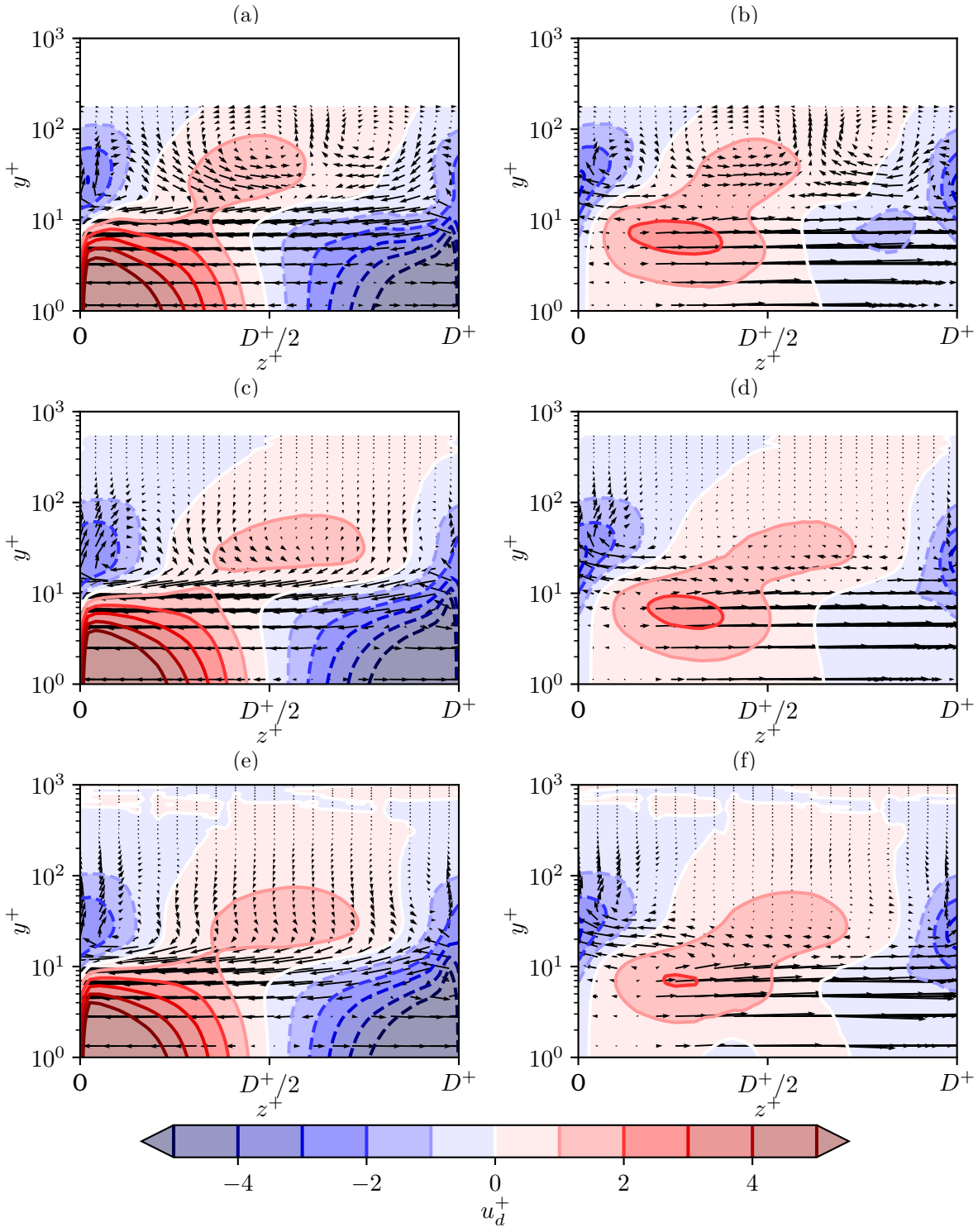

Figure 4.10: $z-y$ planes of time-averaged streamwise disc velocity taken at $x^+ = D^+/2$ (a),(c),(e) and $x^+ = D^+$ (b),(d),(f), shown with logarithmic y^+ scaling. The arrows indicate v_d and w_d velocity components. All cases are only shown up to $y^+ = 180$

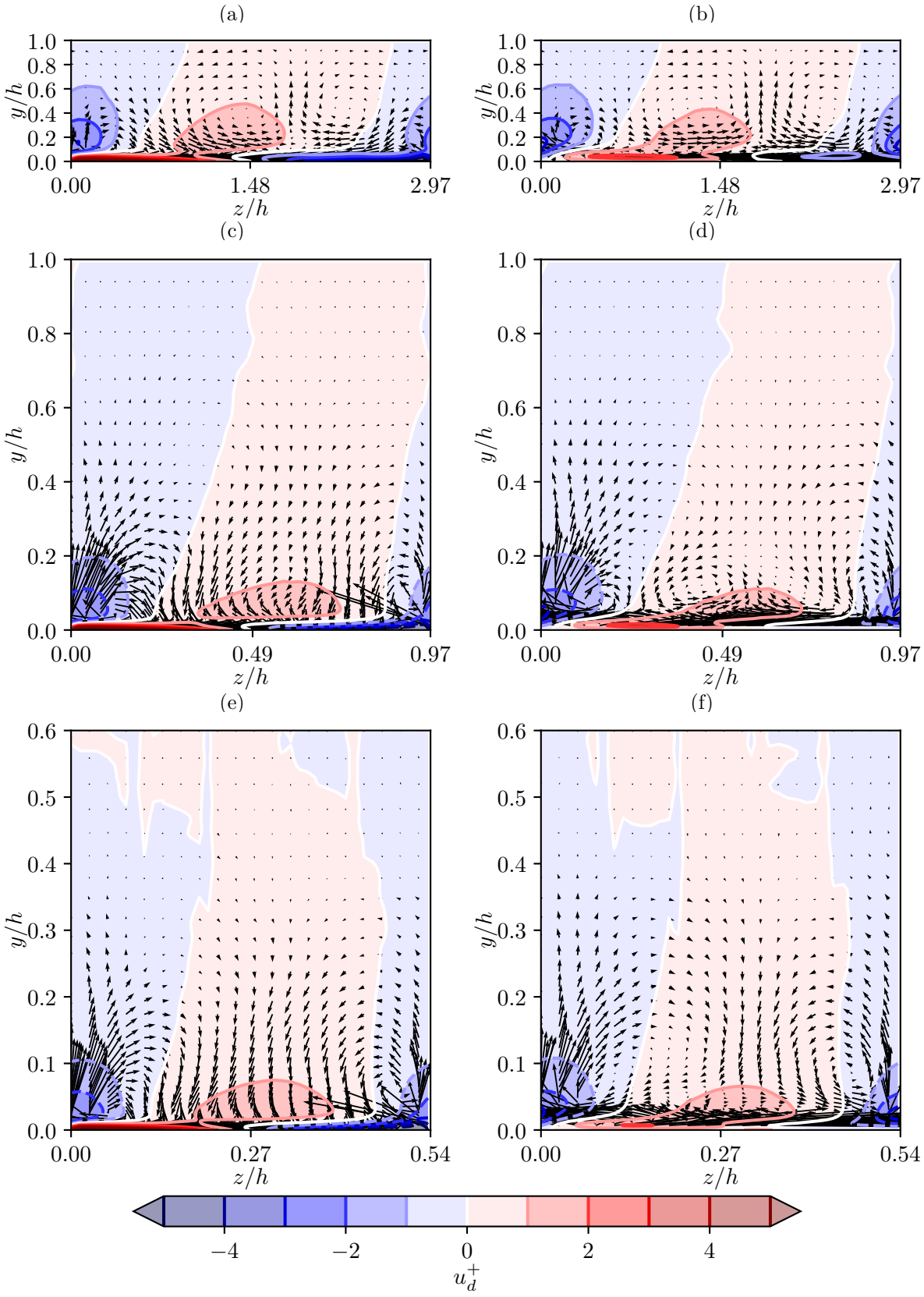

Figure 4.11: $z-y$ planes of time-averaged streamwise disc velocity taken at $x^+ = D^+/2$ (a),(c),(e) and $x^+ = D^+$ (b),(d),(f), shown with linear y^+ scaling. The arrows show the direction and magnitude of the spanwise and wall-normal disc velocity.

4.4.2 Time-averaged velocity profiles

In this subsection, the local velocity profiles for the total $\overline{u}^+(x,z)$ and disc $\overline{u_d}^+(x,z)$ velocities, normalized by the mean u_τ, are plotted together for each x,z location within the two-disc domain. The result is bundles of velocity profiles for both $D^+ = 546$ and $D^+ = 801$ families, where the grey region bounded by the dotted lines indicates the range between the maximum and minimum velocity. The dash-dotted line instead represents one standard deviation from the mean, indicated by the continuous red line. The larger the spread between minimum and maximum, the more intense is the influence of the disc flow onto the channel flow.

Figure 4.12 shows the streamwise velocity profile $\overline{u}^+(x,z)$ distribution over y^+ for the cases D180_5, D550_5 and D1000_5 in panels (a), (b) and (c) respectively. The spread of the bundle at $y^+ = 1$ is constant across the Re_τ range, which is expected since the disc angular velocity and diameter have been scaled in viscous units. At Re_τ=180 the spatial inhomogenuity occurs up to the center of the channel, suggesting that at such low friction Reynolds number, the disc influence extends to the whole channel. As Re_τ increases, the velocity profile collapses onto the mean profile in the region y^+≈350-400, above which the mean velocity profiles are homogeneous in x and z directions.

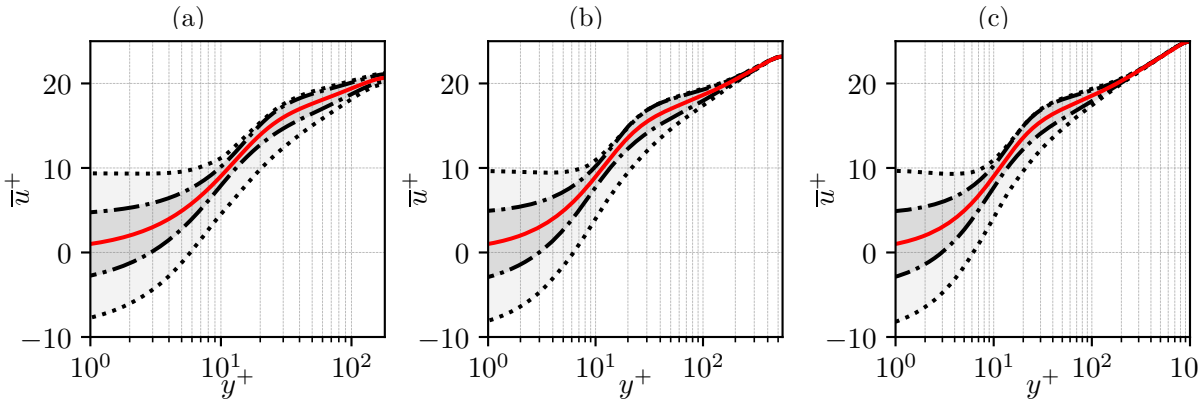

Figure 4.12: Local $\overline{u}^+(x,z)$ velocity profile distribution for cases D180_5 (a), D550_5 (b) and D1000_5 (c). The dotted lines represent the maximum and minimum velocity attained at the respective y^+ locations. The dash-dotted line represent one standard deviation from the mean velocity, in the continuous red line (—)

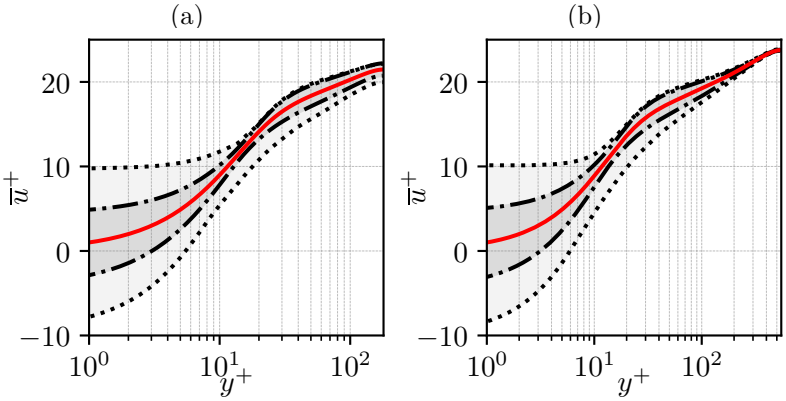

Figure 4.13: Local $\overline{u}^+(x,z)$ velocity profile distribution for cases D180_8 (a), D550_8 (b). The dotted lines represent the maximum and minimum velocity attained at the respective y^+ locations. The dash-dotted line represent one standard deviation from the mean velocity, in the continuous red line (—)

Figure 4.13 shows the same $\overline{u}^+(x,z)$ bundle distribution for cases D180_8 (a) and D550_5 (b). At Re_τ=180 the spread at center channel is visibly larger than case D180_5. At Re_τ=550 the bundle collapses in the same region as the $D^+ = 546$ cases, at approximately $y^+ \approx 350 - 400$, suggesting a small dependency of the disc influence is independent of the disc diameter. The lack of data simulation at Re_τ=1000 for $D^+ = 801$, however, does not allow to consolidate this observation.

Extraction and plotting of the disc component of the velocity using Equation (4.6) results in the velocity distribution shown in Figure 4.14 for $D^+ = 546, W^+ = 10.5$ and Figure 4.15 for the $D^+ = 801, W^+ = 11$ families. Firstly, the mean disc velocity distribution in the streamwise direction is zero for all cases, as the disc rotation induces an equal amount of velocity in positive and negative streamwise direction. All Re_τ show a similar scatter from the mean at $y^+ = 1$, which however becomes skewed towards the negative side in the region around $y^+ \approx 10^1$. This may be an effect of the negative streamwise disc velocity present in the inter disc regions. These figure allow to better identify the y^+ range at which the disc influence ceases.

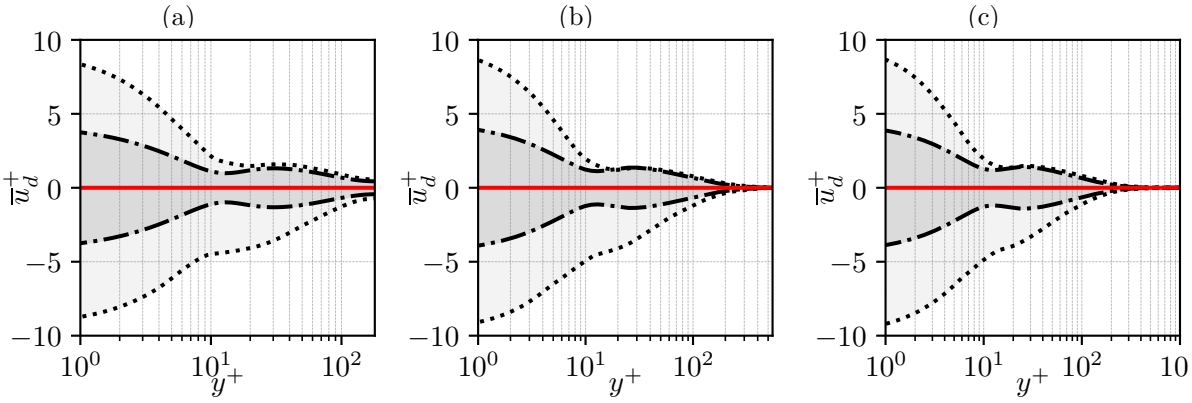

Figure 4.14: Local $\overline{u}_d^+$ velocity profile distribution for cases D180_5 (a), D550_5 (b) and D1000_5 (c). The dotted lines represent the maximum and minimum velocity attained at the respective y^+ locations. The dash-dotted line represent one standard deviation from the mean velocity, in red (—)

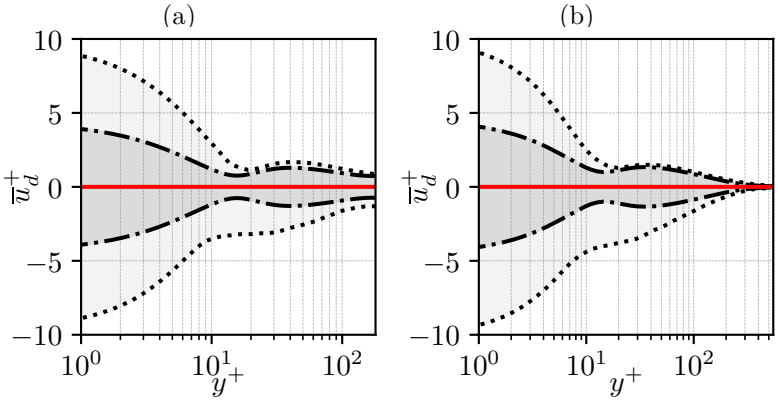

Figure 4.15: Local $\overline{u}_d^+$ velocity profile distribution for cases D180_8 (a), D550_8 (b). The dotted lines represent the maximum and minimum velocity attained at the respective y^+ locations. The dash-dotted line represent one standard deviation from the mean velocity, in red (—)

The distribution of the spanwise disc velocity $\overline{w}_d^+(x,z)$ is a second set of data determine the extension of the disc influence within the channel. As the mean spanwise velocity for channel

flows is zero, the disc and total spanwise velocity coincide. Figure 4.16 and Figure 4.17 show that the spanwise velocity distribution collapses onto the mean much earlier, at $y^+ \approx 20$. The location of the collapse of spanwise velocity distribution on the mean remains constant across the Re_τ range as well as the D^+ parameter chosen. This allows to identify the direct influence of the disc motion, independently of the effects of the inter-disc ejections.

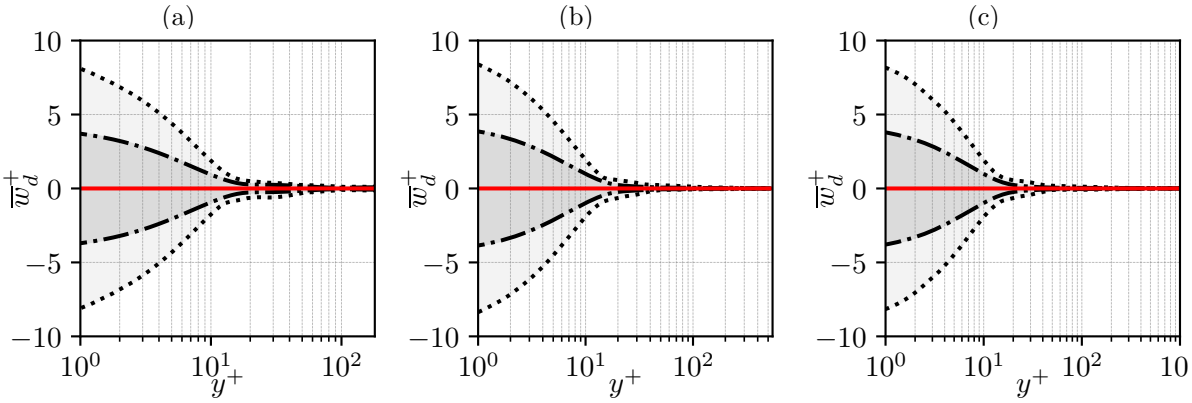

Figure 4.16: Local $\overline{w}_d^+(x,z)$ velocity profile distribution for cases D180_5 (a), D550_5 (b) and D1000_5 (c). The dotted lines represent the maximum and minimum velocity attained at the respective y^+ locations. The dash-dotted line represent one standard deviation from the mean velocity, in red (—)

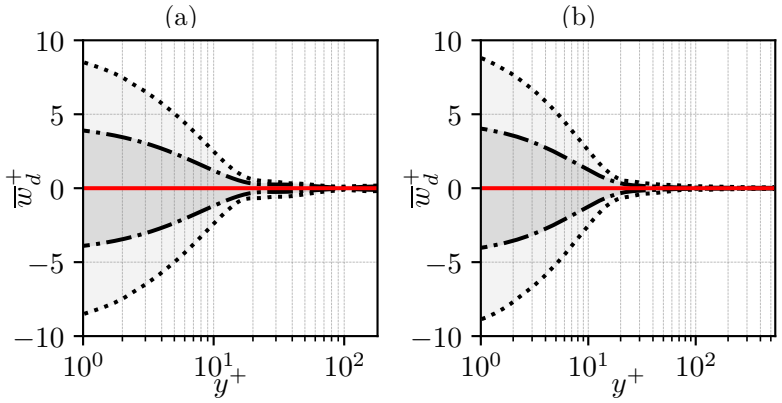

Figure 4.17: Local $\overline{w}_d^+(x,z)$ velocity profile distribution for cases D180_8 (a), D550_8 (b). The dotted lines represent the maximum and minimum velocity attained at the respective y^+ locations. The dash-dotted line represent one standard deviation from the mean velocity, in red (—)

Next to the velocity bundle distribution in viscous units, Figure 4.18 shows the x-averaged velocity defect $\left(\widetilde{u}_c(z) - \tilde{u}(y,z)\right)/\tilde{u}_\tau(z)$ for different spanwise positions on the disk. Here, $\widetilde{u}_c(z) = \widetilde{u}(y=0,z)$ is the velocity at the center of the channel at a determinate z location, $\tilde{u}(y,z)$ is the velocity profile averaged in the x-direction, whereas $\tilde{u}_\tau(z)$ is the local friction velocity averaged in the x-direction at each z location. The $\tilde{f}$ operator is defined for a given variable f as:

$$\tilde{f}(z,y) = \frac{1}{2D}\int_0^{2D} \bar{f}(x,y,z)\mathrm{d}x. \tag{4.21}$$

This set of figures reinforce the observations the disc velocity extends its influence to the center of the channel for low Re_τ, and that already from Re_τ=550, the collapse of the bundle onto one

single profile suggests that the central portion of the channel is no longer affected by the disc presence. From this, one can conclude that the influence of the friction Reynolds number will become less important at high values of Re_τ.

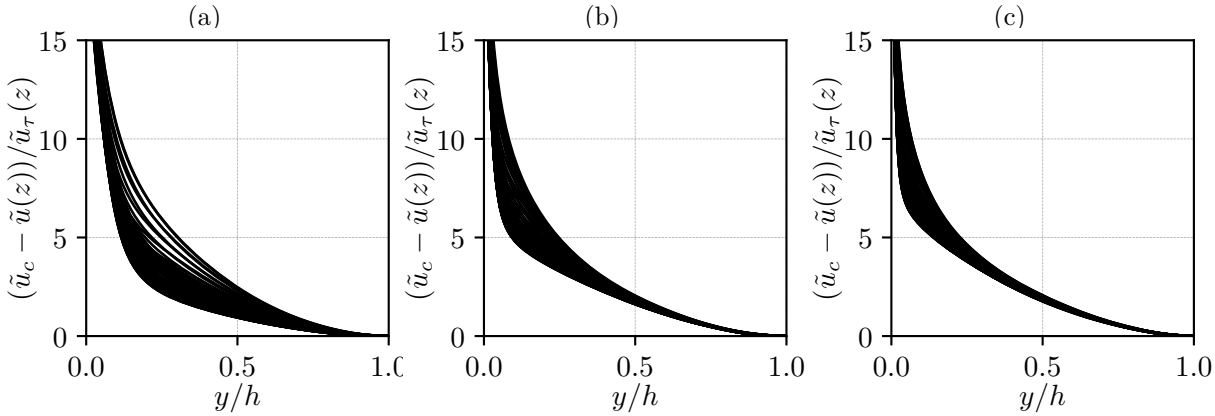

Figure 4.18: X-averaged velocity defect distribution for different spanwise positions on the disc for cases D180_5 (a), D550_5 (b) and D1000_5 (c).

4.5 Reynolds Stresses

In this section the Reynolds stresses for the disc simulations will be analyzed. For sake of conciseness, only the Reynolds stresses for the D180_5, D550_5 and D1000_5 cases are included for analysis. First, the distribution of the Reynolds stresses in the wall-normal direction is discussed in Subsection 4.5.1. A deeper analysis in the spatial distribution of the Reynolds stresses in the domain, via the use of slice planes, is provided in Subsection 4.5.2. Lastly, a brief comparison between computational and experimental results from Sem (2021) is provided in 4.5.3.

The presence of the disc actuators introduces a disc component of the Reynolds stress which is introduced in the derivation that follows. From Equation (4.6), time averaging of $u_i' u_j'$ yields

$$\overline{u_i' u_j'} = \overline{(u_i - \overline{u}_i) - (u_j - \overline{u}_j)} = \overline{u_i u_j} - \overline{u}_i\,\overline{u}_j. \tag{4.22}$$

Introducing the disc velocity component $u_{d,i}$ defined in Equation (4.7),

$$\overline{u_i' u_j'} = \overline{u_i u_j} - (\langle u_i \rangle + u_{d,i})\,(\langle u_j \rangle + u_{d,j}) \tag{4.23}$$

Carrying out the multiplication, applying the $\langle . \rangle$ operator and rearranging the terms one obtains:

$$\langle \overline{u_i u_j} \rangle + \langle u_i \rangle \langle u_j \rangle = \left\langle \overline{u_i' u_j'} \right\rangle - \langle u_{d,i} u_{d,j} \rangle\,. \tag{4.24}$$

This results in three distinct Reynolds stress components: the total Reynolds stress component $\left\langle \tau_{tot_{i,j}} \right\rangle = \langle \overline{u_i u_j} \rangle - \langle u_i \rangle \langle u_j \rangle$, the turbulent component $\left\langle \overline{u_i' u_j'} \right\rangle$ and the disc component $\langle u_{d,i} u_{d,j} \rangle$. These components can also be expressed in viscous units by normalization with u_τ^2 leading to $\left\langle \tau_{tot_{i,j}} \right\rangle^+$, $\left\langle \overline{u_i' u_j'} \right\rangle^+$ and $\langle u_{d,i} u_{d,j} \rangle^+$.

4.5.1 Wall-normal distribution

Figure 4.19 shows the Reynolds stresses distribution in outer units for case D180_5 and S180. The total Reynolds stress for the smooth wall case is shown in continuous red line, the total Reynolds stress for the disc-on simulation in the continuous black line. The disc and turbulent component are shown in dashed and dash-dotted lines respectively.

Figures 4.19, 4.20, 4.21 are arranged with panel (a) showing the $\langle \tau_{tot_{uu}} \rangle^+$, $\langle \overline{u'u'} \rangle^+$ and $\langle u_d u_d \rangle^+$ streamwise Reynolds stresses; panel (b) showing the $\langle \tau_{tot_{vv}} \rangle^+$, $\langle \overline{v'v'} \rangle^+$ and $\langle v_d v_d \rangle^+$ wall-normal stresses; panel (c) shows the $\langle \tau_{tot_{ww}} \rangle^+$, $\langle \overline{w'w'} \rangle^+$ and $\langle w_d w_d \rangle^+$ spanwise stresses and panel (d) shows the $\langle \tau_{tot_{uv}} \rangle^+$, $\langle \overline{u'v'} \rangle^+$ and $\langle u_d v_d \rangle^+$ Reynolds stresses.

At Re_τ=180, shown in Figure 4.19, the streamwise total Reynolds stress $\langle \tau_{tot_{uu}} \rangle^+$ for case D180_5 declines to reach a local minimum at $y/h \approx 0.05$ ($y^+ \approx 10$), followed by a slight increase to a local maximum at $y/h \approx 0.12$ ($y^+ \approx 21.6$). This wall-normal coordinate coincides with the center of the inter-disc ejections, seen in Figure 4.8. A similar pattern is followed by the disc Reynolds stress component, which reaches a local minimum at $y/h \approx 0.07$ ($y^+ \approx 12.6$), followed by a local maximum at $y/h \approx 0.15$ ($y^+ \approx 27$). As the distance from the wall increases, the disc Reynolds component decreases monotonically towards zero. At higher Re_τ, the pattern is similar, but the wall-normal scaling in outer units causes a shift in turbulent activity closer to the wall.

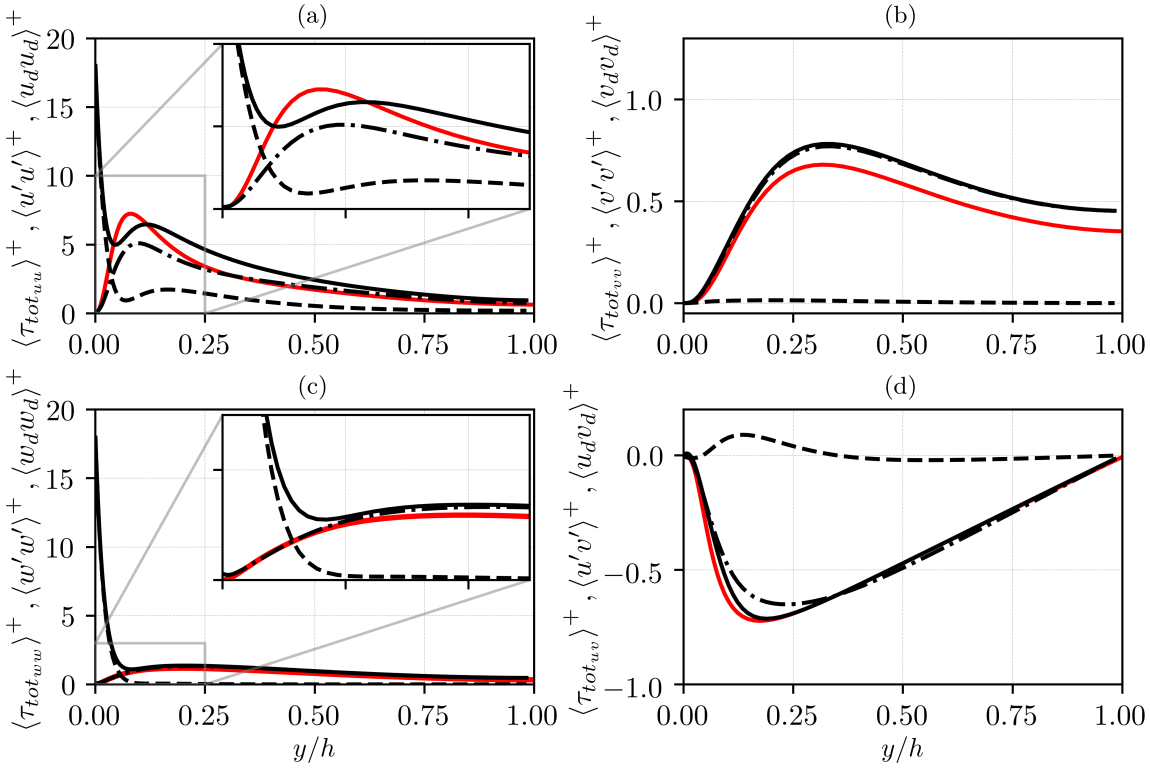

Figure 4.19: Reynolds stresses comparison between the disc case D180_5 and S180 (—). The disc stresses are represented as total stress (—), disc stress (- - -) and turbulent stresses (-·-·) at Re_τ=180.

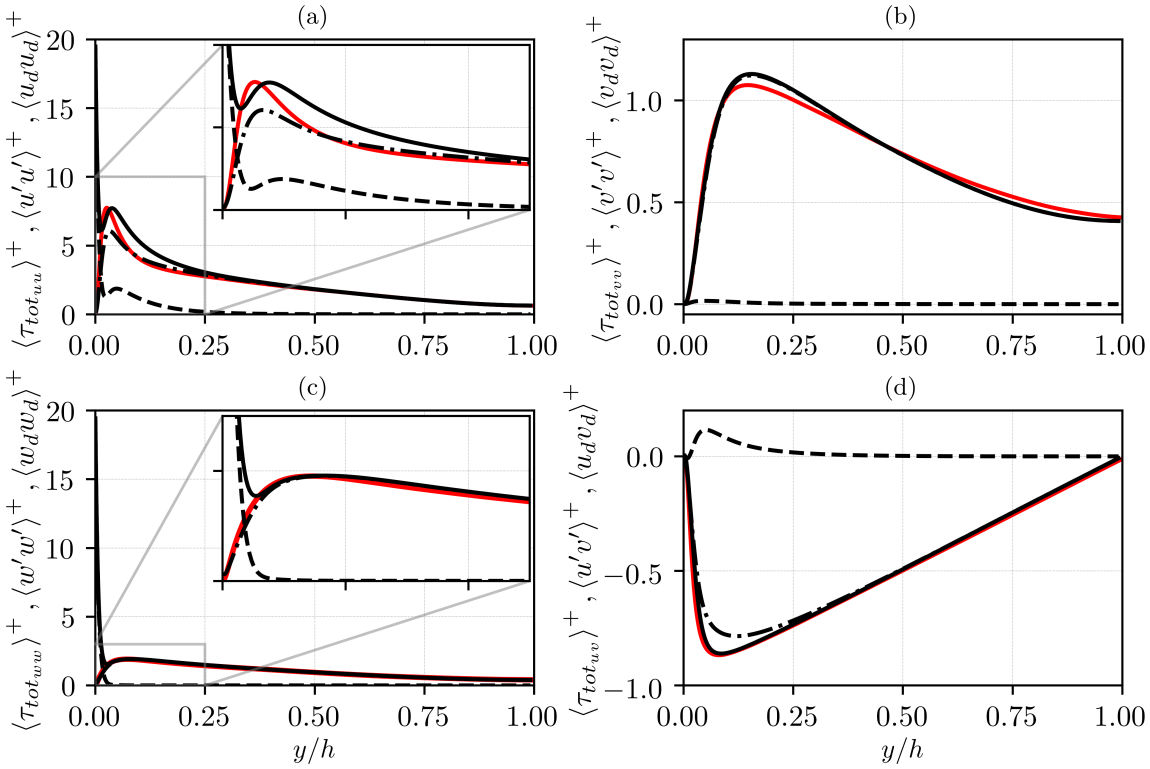

Figure 4.20: Reynolds stresses comparison between the disc case D550_5 and S550 (—). The disc stresses are represented as total stress (—), disc stress (- - -) and turbulent stresses (-·-·) at Re_τ=550

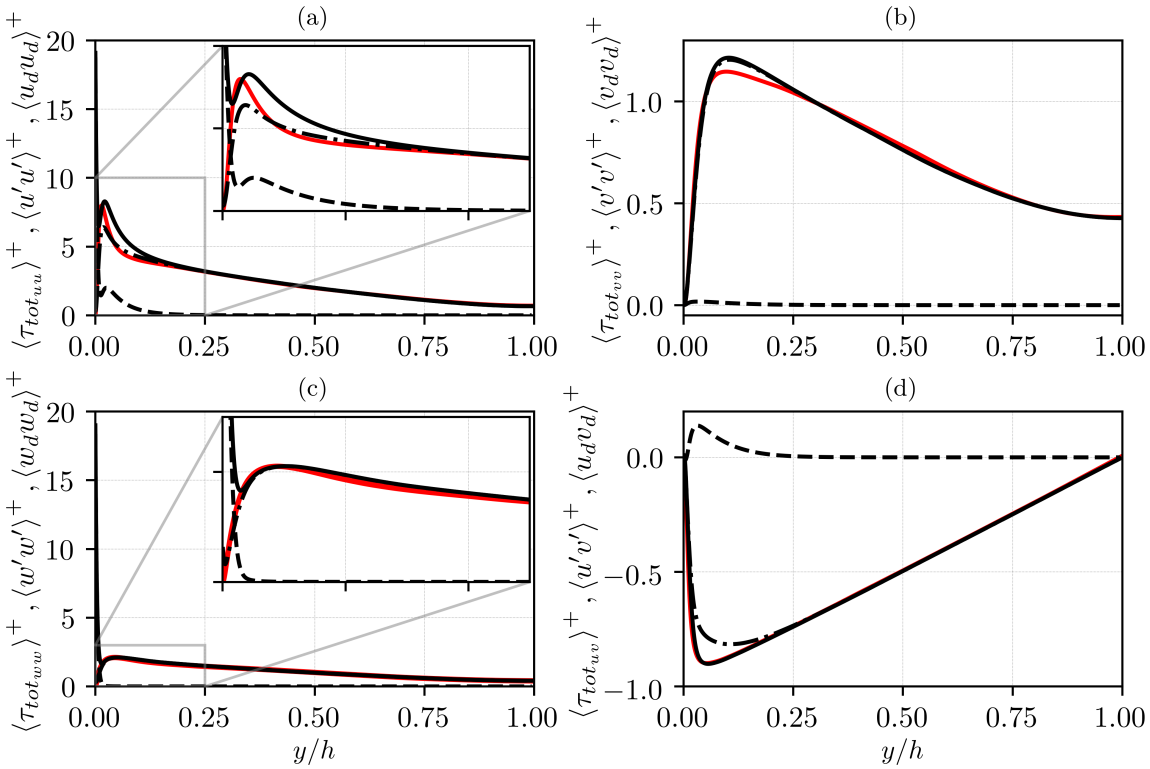

Figure 4.21: Reynolds stresses comparison between the disc case D1000_5 and S1000 (—). The disc stresses are represented as total stress (—), disc stress (- - -) and turbulent stresses (-·-·) at Re_τ=1000

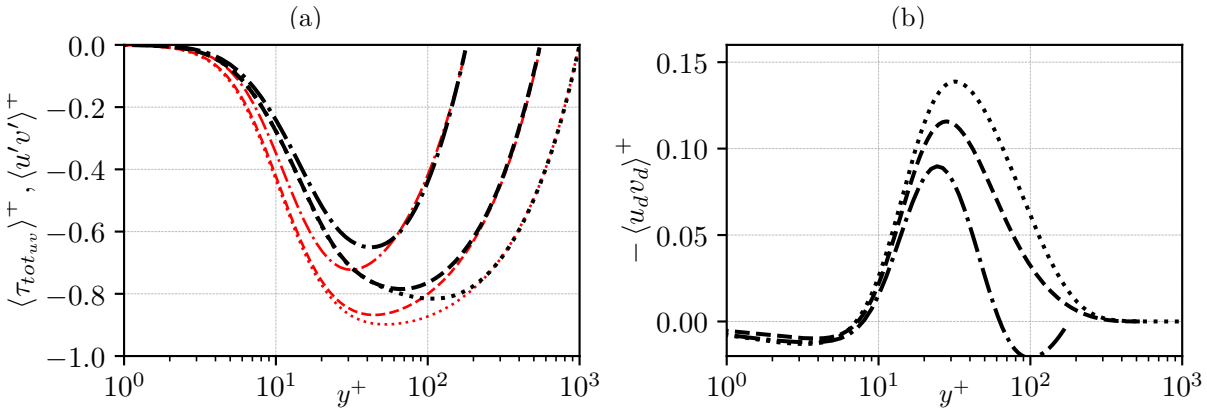

Figure 4.22: Reynolds stress components for disc case $D^+ = 546, W^+ = 10.5$ at Re_τ=180 (-·-·-), Re_τ=550 (- - -), Re_τ=1000 (·····). Panel (a) shows the turbulent $\langle \overline{u'v'} \rangle^+$ stress for the disc-on (black) and smooth-wall (red). Panel (b) shows instead the disc Reynolds stress $\langle u_d v_d \rangle^+$.

The wall-normal total Reynolds stress $\langle \tau_{tot_{vv}} \rangle^+$ is mostly influenced by the turbulent component, with the disc flow component $\langle v_d v_d \rangle^+$ being barely noticeable. This was expected, as the actuators do not induce particularly large velocity fluctuations in the y direction, exception made for the inter-disc ejections at the lateral disc edges. Compared to case S180, the total wall-normal Reynolds stress for D180_5 is higher, which is caused by increased turbulent component. Cases D550_5 and D1000_5 show a similar behaviour for higher Re_τ.

The total spanwise Reynolds stress $\langle \tau_{tot_{ww}} \rangle^+$ for D180_5 show a similar behavior with respect to the streamwise total stress at the wall, with a peak of similar magnitude. This peak at the wall is driven by the disc component, which rapidly drops to zero at $y/h \approx 0.11$ ($y^+ \approx 18$). Above this coordinate, the total spanwise Reynolds lines for the disc-on case matches the smooth wall total Reynolds stress line. Similarly to the streamwise and wall normal stress components, the behavior remains similar with increasing Re_τ, only at lower y/h.

Lastly, the total $\langle \tau_{tot_{uv}} \rangle^+$ Reynolds stresses for cases S180 and D180_5 are similar. The disc component however has a positive value, peaking at $y/h \approx 0.14$ ($y^+ \approx 25$), after reducing around zero above $y/h \approx 0.44$ ($y^+ \approx 80$). This behaviour is maintained across the Re_τ range, as shown in Figures 4.20 and 4.21, with the wall-normal locations of maxima and minima remaining constant when considered in wall units. This will be better explained in the following subsection, where wall-normal stress distributions will be shown in wall units.

The decomposition of the drag reduction presented in Section 4.3 has highlighted that the turbulent stresses are the main driver of the decrease in drag reduction performance with increasing Re_τ. Figure 4.22 shows the Reynolds stress components profiles for disc case $D^+ = 546, W^+ = 10.5$ at Re_τ=180 (dashed line), Re_τ=550 (dotted line) and Re_τ=1000 (dash-dotted line). Panel (a) shows the turbulent $\langle \overline{u'v'} \rangle^+$ stress for the disc-on (black) and smooth-wall. By plotting these quantities in viscous units, it's possible to notice that for $Re_\tau = 550$ and 1000, the disc-on turbulent stresses collapses back onto the smooth wall total stresses in the region $y^+ \approx 250$. Furthermore the turbulent stresses for those two Re_τ follow the same profile before splitting at $y^+ \approx 50$. Panel (b) shows instead the disc Reynolds stress $\langle u_d v_d \rangle^+$. The disc stresses peak shows a progressive increase in magnitude as Re_τ increases. This is a hint that the inter-disc structures, which are the main contributor to the disc stresses become more prominent with increasing Re_τ. However, this increase does not affect the disc component of the drag reduction, as the increase is proportional to the smooth wall turbulent stresses.

4.5.2 Field Reynolds stress visualizations

The spatial distribution of the Reynolds stress levels is presented in this subsection, this will help better understand the characteristics of the flow over the disc actuators, and the location of the characteristic flow structures that have been previously identified. To achieve this, local distributions of the total stress $\overline{uu}$ and $\overline{uv}$ split in their components are shown on lateral $z-y$ slices, taken through the disc center, as well as through a wall-parallel $x-z$ plane at $y^+ = 30$.

Figure 4.23 shows the distribution of the local total Reynolds stress $\tau^+_{tot_{uu}}$, turbulent $\overline{u'u'}^+$, and disc $-(u_d u_d)^+$ Reynolds stresses in the first, second and third columns respectively. The fourth column shows the spatially averaged $\langle \tau_{tot_{uu}} \rangle^+$, $\left\langle \overline{u'u'} \right\rangle^+$ and $\langle u_d u_d \rangle^+$ streamwise Reynolds stresses seen in Figures 4.19(a), 4.20(a) and 4.21(a). The rows show results for the D180_5, D550_5 and D1000_5 simulations respectively.

The near-wall region is characterized by a region of high total Reynolds stress intensity, especially on the left hand side of the disc. There, the disc moves against the mean flow direction. On the right side, the intensity of the total stress is smaller. The inter-disc ejections are identified by a region of negative stress, centered at y^+=35 across the Re_τ range. A region of high stress is present at the same height above the disc center. This height corresponds to a local maximum for the total averaged Reynolds stress and its disc component. The topology of the Reynolds stresses remains unchanged across the Re_τ range. For the turbulent stress component, the intensity is concentrated on the disc edges, with higher intensity on the right hand side edge of the disc, which coincides with the disc half moving in the same direction as the flow. Overall, the total local stress is topologically very similar to the disc stresses, shown in the third column. Panels (d),(h),(l) show the averaged stress distribution in wall units. the local minimum in the disc stress seen at $y^+ \approx 12$ in the spatial average plots of disc and total stress, is caused by the buffer region separating the zone that separates the zone where the disc influence is strong and the inter-disc structures.

Figure 4.24 shows the distribution of the local $\tau^+_{tot_{uv}}$, turbulent $\overline{u'v'}^+$, and disc $-(u_d v_d)^+$ Reynolds stresses in the first, second and third columns respectively. The fourth column shows the spatially averaged Reynolds stress components $\langle \tau_{tot_{uv}} \rangle^+$, $\left\langle \overline{u'v'} \right\rangle^+$ and $\langle u_d v_d \rangle^+$ seen in Figures 4.19(d), 4.20(d) and 4.21(d). The rows show results for the D180_5, D550_5 and D1000_5 simulations respectively.

The topology of the $\tau^+_{tot_{uv}}$ stresses is quite different from the $\tau^+_{tot_{uu}}$ stresses presented before. The total stresses carry a large similarity to the disc component. The disc stress is positive on the domain edges, where the disc velocity in the wall-normal direction is positive. In the central portion of the domain the stress is negative, with the exception for a positive $-(u_d v_d)^+$ patch centered around $y^+ \approx 100$, which is solely visible at Re_τ=180. This region is connected to the secondary velocities, shown in Figure 4.10.

In Figure 4.24 at Re_τ=550 and Re_τ=1000, the secondary velocities and the positive disc stress move upstream of the disc center region and thus appear reduced. The turbulent stresses shown in the middle column are weaker in the center of the domain. Comparing the spatially averaged wall-normal distributions in the fourth column, the disc action reduces the intensity of the turbulent stress peak, and moves it away from the wall. This goes to show that the action of the disc is effective in reducing the turbulent $\overline{u'v'}^+$ stresses in the central disc region.

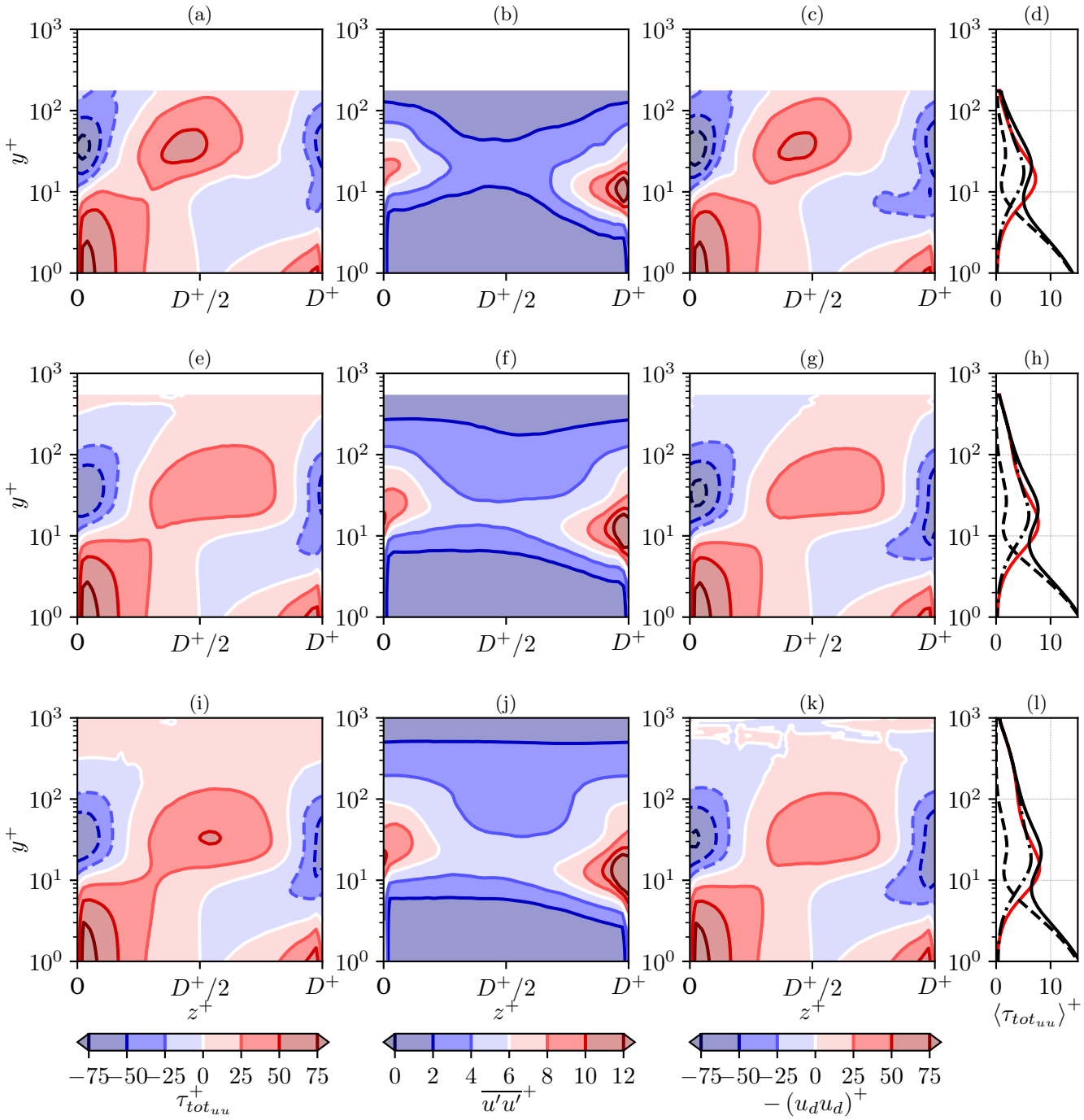

Figure 4.23: Field view of the ensemble averaged $\tau^+_{tot_{uu}}$ Reynolds stresses on a $z-y$ plane through the disc center for case D180_5. The first row shows the stresses for Re_τ=180, the second for Re_τ=550 and the last one for Re_τ=1000. The first column shows the total Reynolds stresses. The second column shows the turbulent component $\overline{u'u'}^+$, the third column shows the disc component $-(u_d u_d)^+$. The fourth column shows the spatially averaged Reynolds stresses for the total component (——), turbulent component (-·-·-), disc component (- - -), and the smooth wall total Reynolds (——).

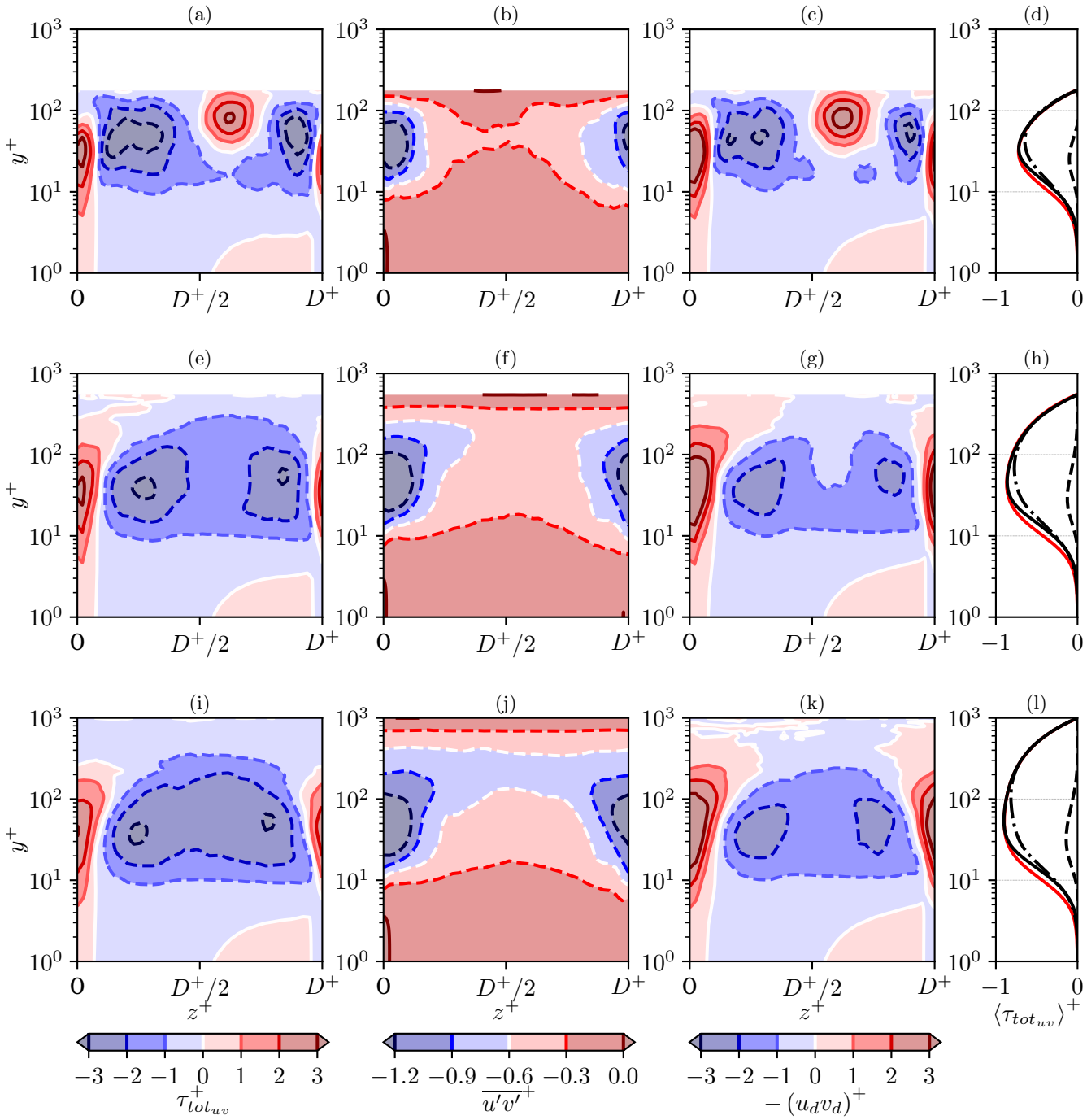

Figure 4.24: Field view of the ensemble averaged $\tau^+_{tot_{uv}}$ Reynolds stresses on a $z-y$ plane through the disc center for case D180_5. The first row shows the stresses for Re_τ=180, the second for Re_τ=550 and the last one for Re_τ=1000. The first column shows the total Reynolds stresses. The second column shows the turbulent component $\overline{u'v'}^+$, the third column shows the disc component $-(u_d v_d)^+$. The fourth column shows the spatially averaged Reynolds stresses for the total component (——), turbulent component (-·-·), disc component (- - -), and the smooth wall total Reynolds (——).

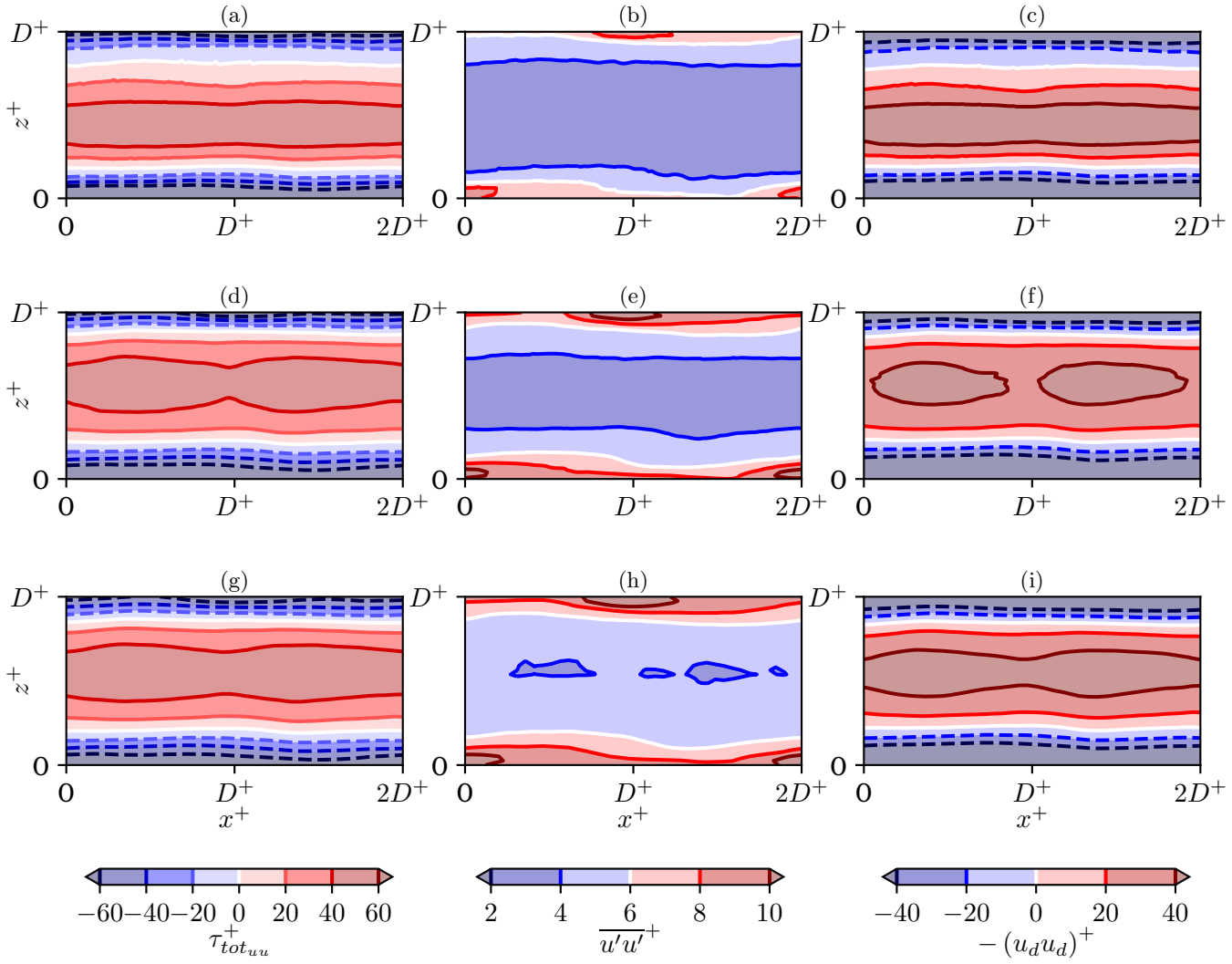

Figure 4.25: Field view of the ensemble averaged Reynolds $\tau^+_{tot_{uu}}$ stresses on a wall-parallel $x-z$ plane at y^+=30 for case D180_5. The first row shows the stresses for Re_τ=180, the second for Re_τ=550 and the last one for Re_τ=1000. The first column shows the total $\tau^+_{tot_{uu}}$ Reynolds stresses.The second column shows the turbulent component $\overline{u'u'}^+$, the third column shows the disc component $-(u_d u_d)^+$.

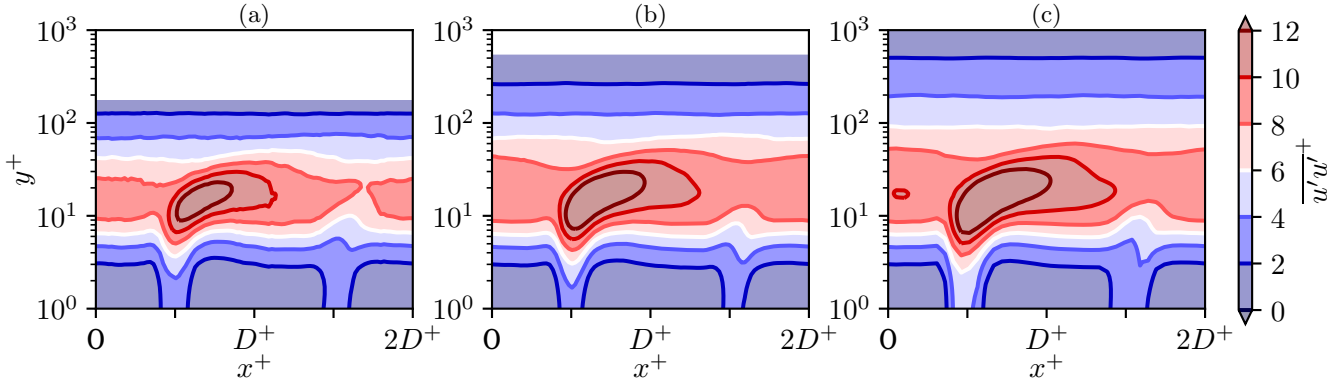

Figure 4.26: Field view of the ensemble averaged turbulent Reynolds stress $\overline{u'u'}^+$ on a $x-y$ plane taken at $z^+ = D^+$ for cases D180_5, D550_5 and D1000_5.

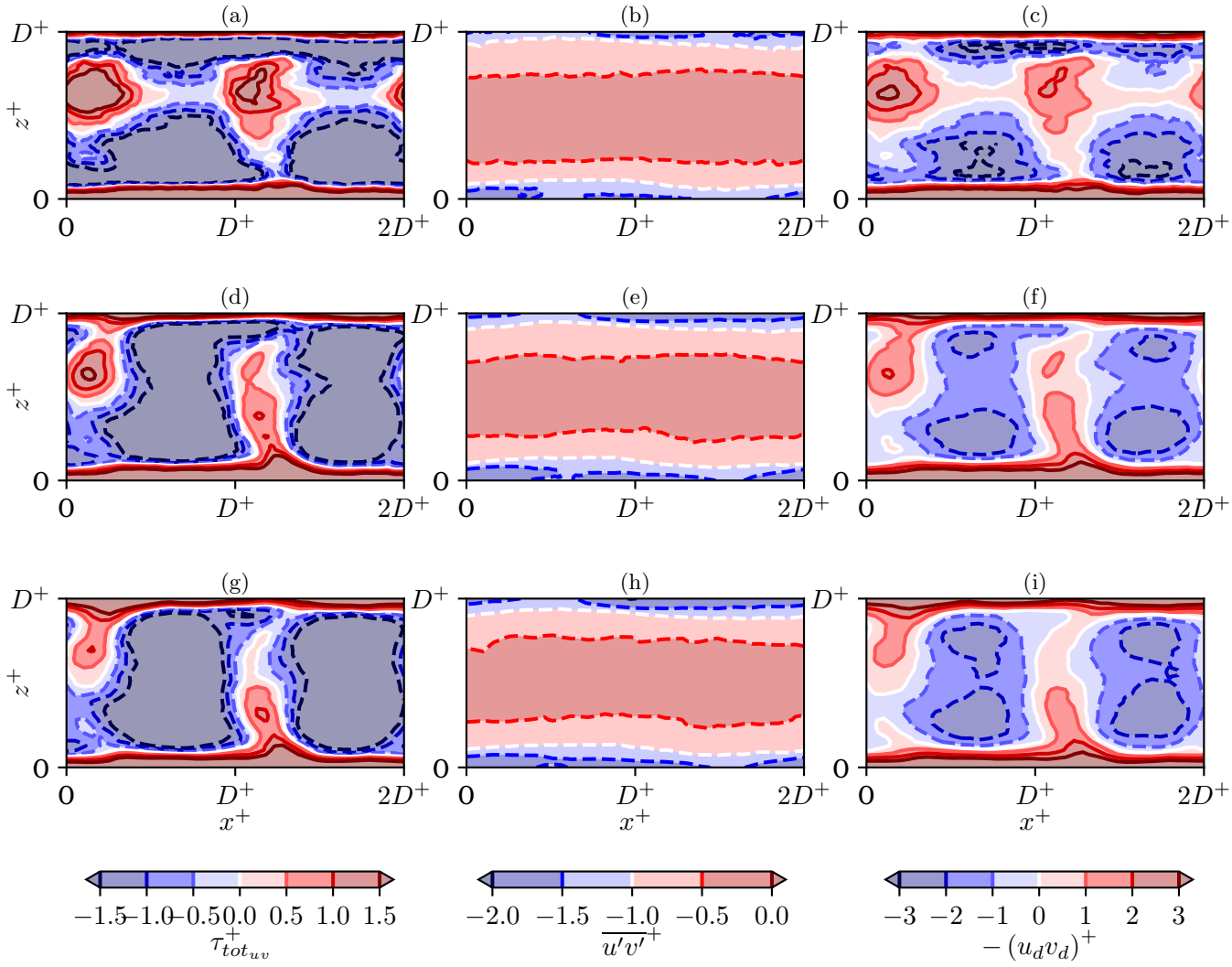

Figure 4.27: Field view of the ensemble averaged Reynolds $\tau^+_{tot_{uv}}$ stresses on a wall-parallel $x-z$ plane at y^+=30 for case D180_5. The first row shows the stresses for Re_τ=180, the second for Re_τ=550 and the last one for Re_τ=1000. The first column shows the total $\tau^+_{tot_{uv}}$ Reynolds stresses.The second column shows the turbulent component $\overline{u'v'}^+$, the third column shows the disc component $-(u_d v_d)^+$.

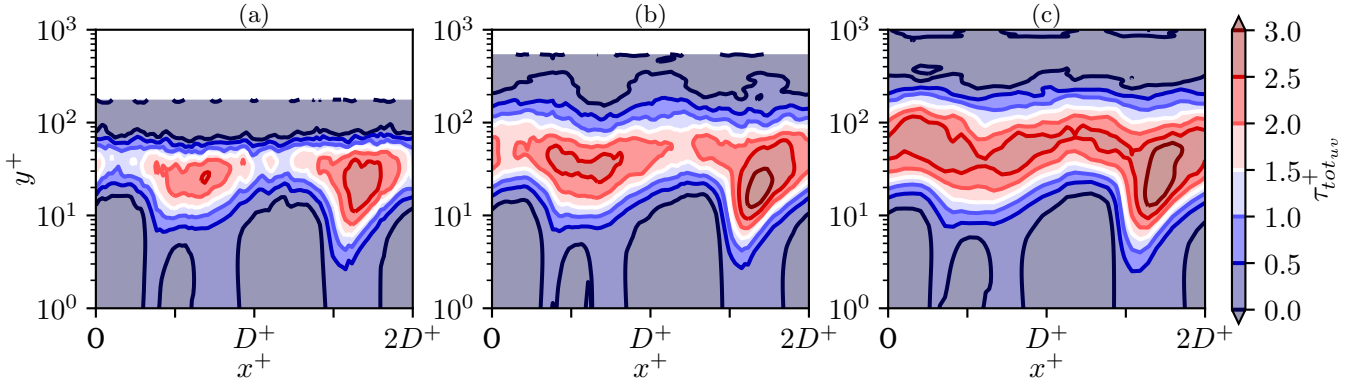

Figure 4.28: Field view of the ensemble averaged turbulent Reynolds stress $\tau^+_{tot_{uv}}$ on a $x-y$ plane taken at $z^+ = D^+$ for cases D180_5 (a), D550_5 (b) and D1000_5 (c).

The $z-y$ planes shown in Figure 4.23 have highlighted $y^+ = 30$ as an active region for the stresses across the Re_τ. Figure 4.25 shows how the streamwise Reynolds stress and its components are distributed on a wall-normal parallel plane at $y^+ = 30$ for cases D180_5, D550_5 and D1000_5. The first column shows that the total Reynolds stress $\tau^+_{tot_{uu}}$ is largely independent of the streamwise position for the whole Re_τ range. The simulation at Re_τ=180 shows a slight bias in the total stress to one side of the domain, which moves to the center of the domain for the simulations at higher Re_τ. The turbulent stress shows two notable features for all three Re_τ tested. As previously observed, turbulent Reynolds stress intensity is higher on the disc edges. There are three spots of high intensity regions are located $\approx 1/8D^+$ behind the lateral edge of the disc, on the side where the disc tip velocity is against the mean channel flow motion.

Figure 4.26 shows a $x-y$ slice of $\overline{u'v'}^+$ plotted at $z^+ = D^+$. The contours of the turbulent stress component show the origin of the turbulent intensity at the disc interface, where there is a large velocity discontinuity between two spanwise adjacent discs. This sharp jump in velocities was identified by Ricco and Hahn (2013) as the main mechanism generating the inter-disc ejections. The intensity of these structures appears to increase with increasing Re_τ. At the same time, the turbulent stresses in the central region decrease in intensity with increasing Re_τ.

Figure 4.27 shows the $\tau^+_{tot_{uv}}$, $\overline{u'v'}^+$, $-\overline{u_d v_d}^+$ stresses on the wall-parallel plane at $y^+ = 30$. The topology varies significantly in the streamwise and spanwise directions. First, the total stress $\tau^+_{tot_{uv}}$ plot shows a significant change of the distribution with increasing Re_τ, due to influence from the disc stresses. At Re_τ=180 the positive $\tau^+_{tot_{uv}}$ patches at the disc center extend for the whole domain in the x direction. These patches are correspond to the secondary velocities seen in Figure 4.10. As Re_τ increases the secondary velocities are still present, however they decrease in intensity and are located closer to the interface between the two streamwise aligned discs, leaving a large portion of negative Reynolds stress above the discs. Figure 4.28 shows a $x-y$ slice of $\tau^+_{tot_{uv}}$ plotted at $z^+ = D^+$. The total stress contours appear to increase in intensity with increasing Re_τ, which can be correlated to the worsening of drag reduction performance at higher Re_τ.

4.5.3 Comparison with experimental results

This thesis project has been running in parallel with a twin graduation project, aimed at investigating the disc actuator performance in a physical environment via means of windtunnel testing (Sem, 2021). The experiment was performed for a boundary layer flow, at $Re_\tau \approx$912, with data collection by means of Particle Image Velocimetry. A direct quantitative comparison cannot be made, since the layout of the disc actuators used in the experimental setup features a gap of $D^+/2$ in x and z directions between the discs, instead of being placed directly adjacent to each other. The experiment used disc diameter $D^+ = 560$ and tip velocity $W^+ = 10.4$ Sem (2021). This subsection will provide a qualitative comparison between case D1000_5 and the experimental results in terms of turbulent $\overline{u'u'}$ Reynolds stresses.

Figure 4.29 displays the $\overline{u'u'}^+$ Reynolds stresses for a wall-parallel plane at $y^+ \approx$70; the experimental results are shown in panel (a), while the computational results are shown in panel (b). Overall, there is a good agreement between the two data-sets despite the slightly different disc arrangement. The experimental results appear to confirm the concentration of higher intensity turbulent Reynolds stresses at the disc edges, already seen for all displayed cases so far. Furthermore, the magnitude range of the turbulent stresses is similar, with slightly weaker intensity seen for the experimental results. This may be a consequence of the increased lateral distance between the disc edges.

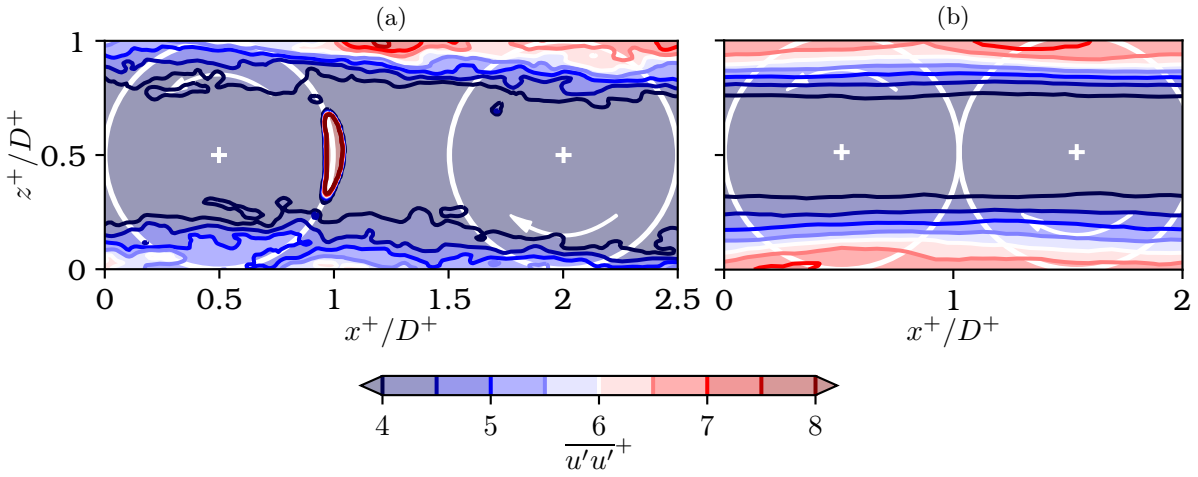

Figure 4.29: Turbulent Reynolds stresses $\overline{u'u'}^+$ on a wall-parallel $x-z$ plane at y^+=70 for the experimental results from Sem (2021) for $D^+ = 560$, $W^+ = 10.4$ at Re_τ=912 (a) and case D1000_5 (b).

4.6 Power Balance

For a successful implementation of the disc actuators, the power needed to actuate the system will necessarily have to be smaller than the power needed for the disc actuation. This subsection will introduce and discuss the results in terms of power balance for the disc actuators. The power required to move the discs against the viscous resistance of the fluid is (Quadrio, 2004)

$$\mathcal{W} = L_x L_z \mu \left\langle \overline{u}_{y=-h} \left.\frac{\partial \overline{u}}{\partial y}\right|_{y=-h} + \overline{w}_{y=-h} \left.\frac{\partial \overline{w}}{\partial y}\right|_{y=-h} \right\rangle. \tag{4.25}$$

For a channel flow, the power required to drive the fluid in x-direction $\mathcal{P}_x$ is obtained by multiplying the wall shear stress by the wall area and the bulk velocity, leading to

$$\mathcal{P}_x = -2U_b L_x L_z \mu \left.\frac{\partial \langle u \rangle}{\partial y}\right|_{y=-h}, \tag{4.26}$$

Ricco and Hahn (2013) define $\mathcal{P}_{sp,t}(\%)$ is the percentage of power spent $\mathcal{W}$ to move the discs with respect to the power $\mathcal{P}_x$ required to drive the flow within the channel for the smooth-wall case:

$$\mathcal{P}_{sp,t}(\%) = \frac{100\mathcal{W}}{\mathcal{P}_x}. \tag{4.27}$$

Finally, the net power saved $\mathcal{P}_{net}$ is the difference between the power saved due to disc rotation, which at constant massflow rate is equal to the drag reduction, and the power spent (Ricco & Hahn, 2013). If the net power balance is positive, there is a net power saving in the actuation of the device:

$$\mathcal{P}_{net}(\%) = \mathcal{DR}(\%) - \mathcal{P}_{sp,t}(\%). \tag{4.28}$$

Figure 4.30 displays the results for the turbulent power spent in panel (a) and the net power balance in panel (b). The results show a clear distinction in the performance of the two disc parameter families tested. The $D^+ = 801$ family, indicated by the dash-dotted line in Figure 4.30(b), shows a positive net power saving at both Re_τ tested achieving $\mathcal{P}_{net} = 1.982\%$ at Re_τ=550. The $D^+ = 546$ family instead shows a negative net power balance across the three

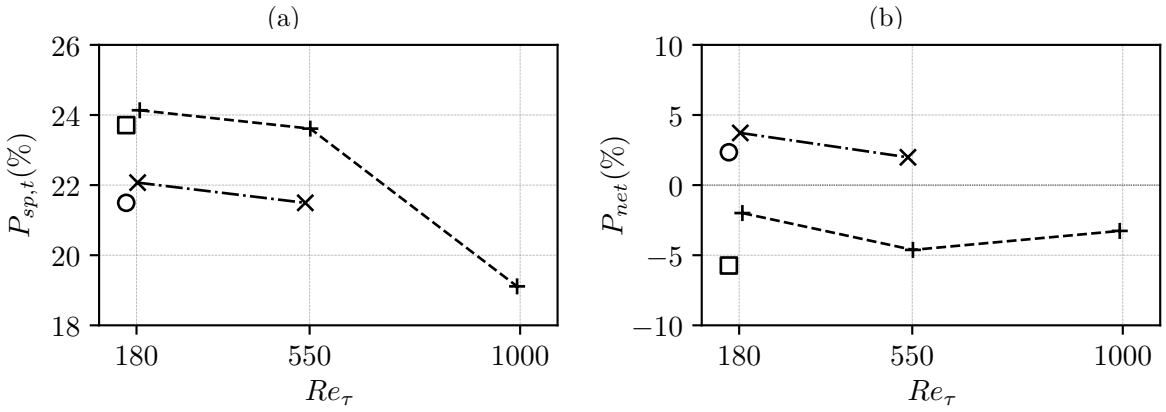

Figure 4.30: Turbulent power spent $\mathcal{P}_{sp,t}$ (a) and net power balance $\mathcal{P}_{net}$ (b) plots for $D^+ = 801, W^+ = 11$ (-·-·) and $D^+ = 546, W^+ = 11$ (- - -). The empty circle and empty square indicate the results for cases RH158_8 and RH158_5 respectively, from Ricco and Hahn (2013).

values of Re_τ tested.

Looking at the power spent $\mathcal{P}_{sp,t}$ in panel (a), there is an $\approx 0.5\%$ decrease for both disc families in the window between Re_τ=180 and Re_τ =550. Information on the power balance at Re_τ=1000 is only available for case D1000_5. Between Re_τ =550 and Re_τ =1000, $\mathcal{P}_{sp,t}$ drops by 4.5%. This drop in $\mathcal{P}_{sp,t}$ is 9 times higher than the decrease between Re_τ=180 and Re_τ =550. This results in a small but noticeable recovery in $\mathcal{P}_{net}$, however insufficient to reach positive net power balance. This recovery may seem promising for disc configurations that have a positive net power balance lower Re_τ. This result is, however, not conclusive and further investigations at higher Re_τ for the $D^+ = 801$ family would be needed to confirm this observation. To better characterize the power balance performance locally on the discs, the local power spent can be calculated within the domain.

To identify the locations where the largest amount of power is spent on the disc, the local power spent $\mathcal{P}_{loc}$ is expressed as

$$\mathcal{P}_{loc}(x,z) = \mu \left(\overline{u}_{y=-h} \left.\frac{\partial \overline{u}}{\partial y}\right|_{y=0} + \overline{w}_{y=-h} \left.\frac{\partial \overline{w}}{\partial y}\right|_{y=0} \right), \tag{4.29}$$

which is related to the total power to move the disc $\mathcal{W} = 2L_xL_z \langle \mathcal{P}_{loc} \rangle$. The local ensemble-averaged power spent is shown in Figure 4.31 for the three Re_τ cases.

The locations where $\mathcal{P}_{loc}(x,z)$ is positive indicate that in those locations, the flow is exercising work onto the disc. The locations where this occurs are delimited by the blue region, and are localized within a circular region on the upstream half of the disc, where the disc velocity moves with the mean channel flow. As the flow and disc are moving in the same direction, the local velocity gradient in the streamwise direction makes it such that the fluid layers above the disc are locally exerting work on the discs. Conversely, the red regions dominate the actuator and show locations where work is exerted by the disc onto the flow. From the figure it is possible to derive that the work spreads radially from the global maximum of $\mathcal{P}_{loc}(x,z)$. Furthermore, as Re_τ increases, the $\mathcal{P}_{loc}(x,z)$ extremes reduce, in a similar fashion to the skin-friction coefficient. The power budget of the discs is summarized in Table 4.2.

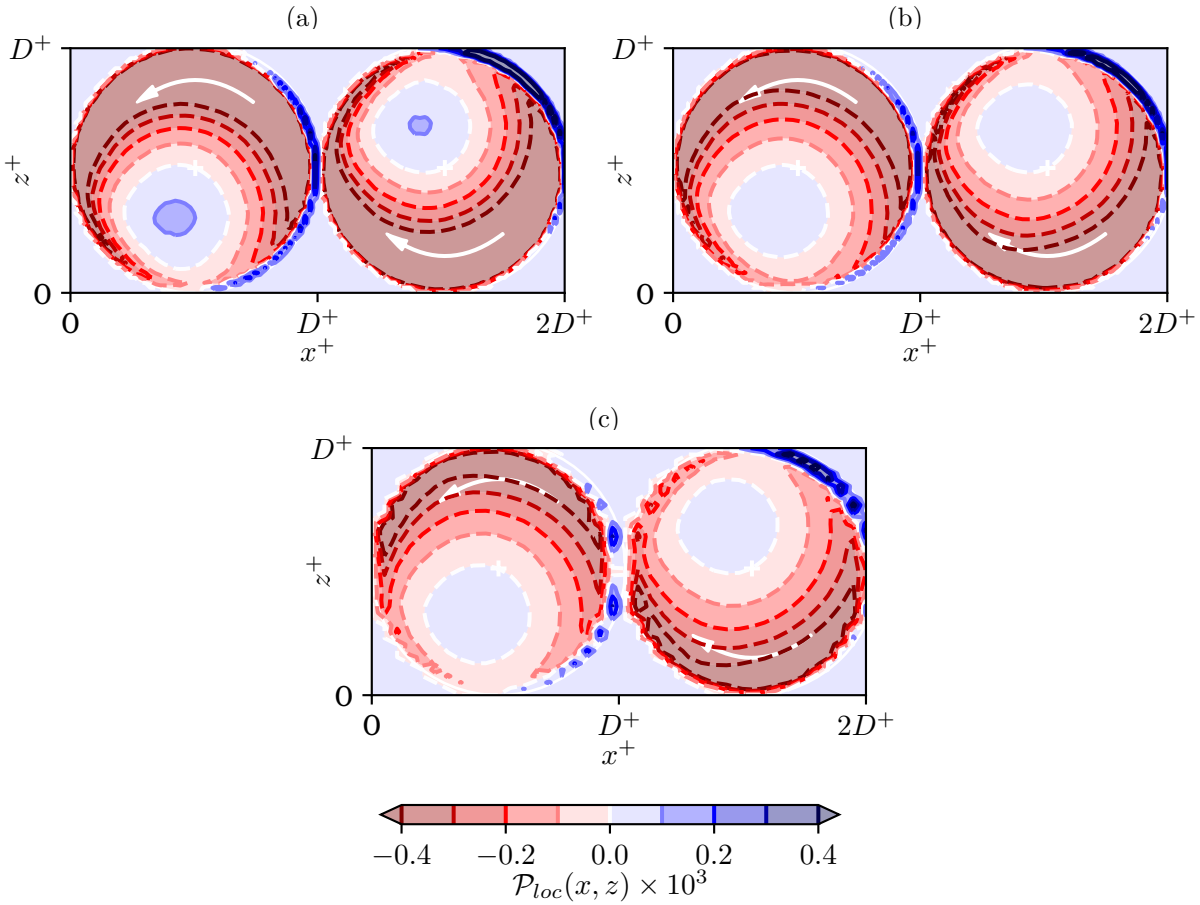

Figure 4.31: Local turbulent power spent $\mathcal{P}_{loc}(x,z)$ for the D180_5 (a), D550_ (b) and D1000_5 (c) cases.

Case	Re_τ	D^+	W^+	$\mathcal{P}_{sp,t}(\%)$	$\mathcal{P}_{net}(\%)$
S180	180	-	-	-	-
RH158_8	158	801.0	10.2	21.494	2.341
RH158_5	158	546.0	10	23.711	-5.734
D180_8	182	801.0	10.72	22.070	3.721
D180_5	186	545.4	10.46	24.134	-1.993
S550	555	-	-	-	-
D550_8	541	803.0	11.24	21.494	1.982
D550_5	551	544.5	10.93	23.611	-4.621
S1000	1008	-	-	-	-
D1000_5	1001	550.0	10.59	19.111	-3.267

Table 4.2: Power budget summary. $\mathcal{P}_{sp,t}(\%)$ is the turbulent power spent as defined in Equation (4.27). $\mathcal{P}_{net}(\%)$ is the net power balance as defined in Equation (4.28).

4.7 Instantaneous Flow Visualization

In this section, a qualitative analysis of lateral, longitudinal and wall-normal planes of instantaneous streamwise and wall-normal velocity is presented for cases D180_5, D550_5 and D1000_5, and their smooth wall counterparts. The instantaneous snapshot shown here can help to better identify the arrangement of the flow and common turbulent structures such as streaks and ejections, under the influence of disc actuators. First, instantaneous velocity at wall-parallel $x-z$ planes are shown for y^+=12. Figure 4.32 shows the location of the lateral and longitudinal slice planes within the domain: one lateral $z-y$ plane passing through the disc center of counter-clockwise rotating discs (plane AA), and two longitudinal planes. Time averaged velocity visualizations have highlighted a strong difference in flow between the disc center and the lateral disc edge. Planes BB and CC show these two regions.

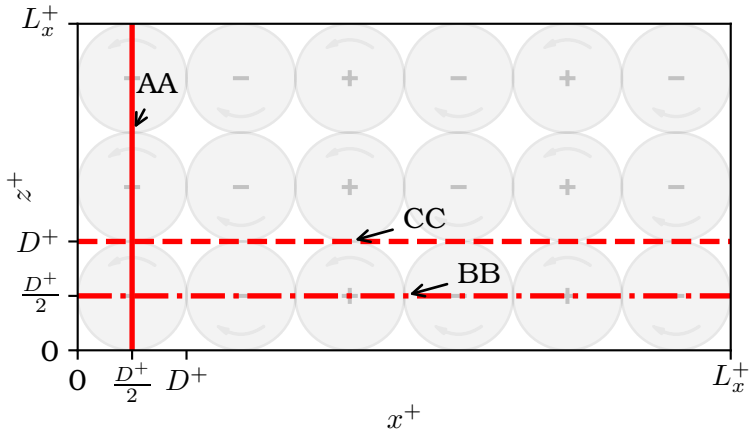

Figure 4.32: Location of the slice planes on the domain. Lateral planes AA passes through the disc center. Longitudinal planes BB and CC pass through the disc center and disc interface.

4.7.1 Wall parallel x-z slices

Figure 4.33 shows the instantaneous streamwise (a,b) and wall-normal (c,d) velocities at y^+=12 for cases S180 and D180_5. The first two rows of disc are displayed for clarity on the positioning of the discs, with plus and minus signs on the disc center representing counter-clockwise and clockwise disc rotation. The disc-on case shows higher velocity in the zone located above the disc centers with a visible reduction in low speed streak activity when comparing with its smooth-wall counterpart. The lateral edges of the discs are characterized by lower streamwise velocity structures and higher velocity fluctuations, caused by the inter-disc ejections previously described. The same reduction in fluctuation intensity is seen in the wall-normal instantaneous velocity plots, shown in Figure 4.33 (c), (d). Lower wall normal fluctuations are seen above the discs, while fluctuations are more intense at the disc interface. These observations are consistent with the averaged statistics shown in Section 4.4 and are connected to the upward shift in the log-law region seen in Figure 4.1.

Figure 4.34 shows the same $x-z$ wall-parallel plane for case D550_5 and S550. The observations made for the Re_τ=180 case hold also for the simulations at Re_τ=550. Turbulent activity is reduced above the disc centers, while retaining smooth-wall levels at the lateral disc interface both in the streamwise and wall-normal velocity visualizations. Figure 4.35 shows the same instantaneous flow visualizations for cases D1000_5 and S1000. For this figure the domain shown has been clipped to allow better identifications of the discs. At Re_τ=1000, the effect of the discs is visually similar to what was reported for the lower Reynolds numbers cases.

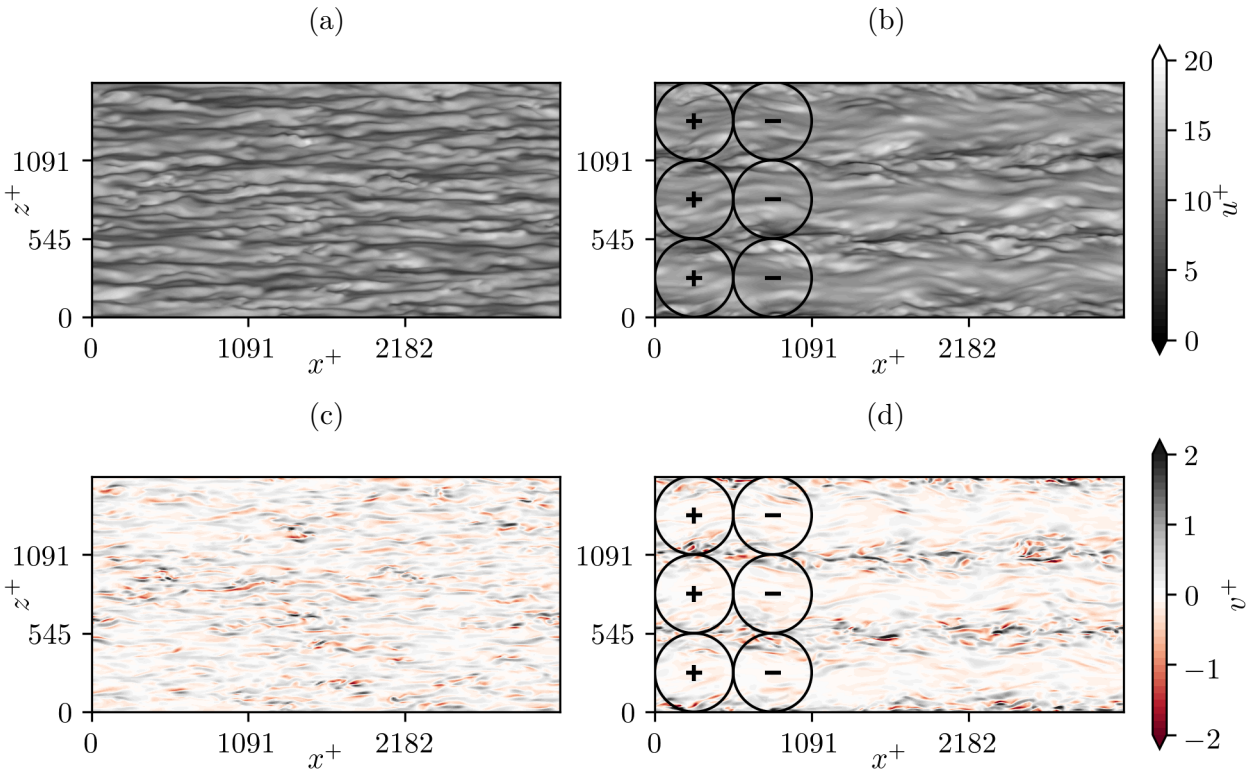

Figure 4.33: Comparison of instantaneous u^+ and v^+ visualizations on a wall-parallel plane at y^+=12, for cases S180 (a),(c) and D180_5 (b),(d).

4.7.2 Lateral z-y slices

Figure 4.36 shows the instantaneous u^+ distribution on the lateral $z-y$ plane AA for case S180 (a) and case D180_5 (b). The dashed lines running across the y/h axis on panel (b) indicate the location of the disc edges, whereas the small vertical black ticks indicate the location of the disc center. Thee central portion of the disc-on channel shows a clear increase in local velocity compared to the smooth wall case. Furthermore, the actuation of the discs results in a visible reduction of the extension of low speed fluctuations in the near-wall region. This effect is maximized at the disc centers, while the lateral disc interface see low speed pockets extending further away from the wall. There is also a visible difference on the flow velocity just above the discs. Looking at the bottom wall, the left hand side of the discs, where the disc rotation is moving against the mean channel flow, has a visibly higher velocity than the right hand side.

Figure 4.37 shows the instantaneous streamwise velocity for the S550 and D550_5 cases. The features observed are similar to the Re_τ=180. The velocity at the center of the channel for the disc-on case is visibly higher than its smooth wall counterpart, which is a clear hint of drag reduction. Furthermore, in the near-wall region the low speed structures are confined to the lower layers of the channel flow, with pockets that extend further away from the wall at the interface between adjacent discs. The results for cases S1000 and D1000_5 are shown in Figure 4.38, where the observations made for the simulations at lower Re_τ are valid.

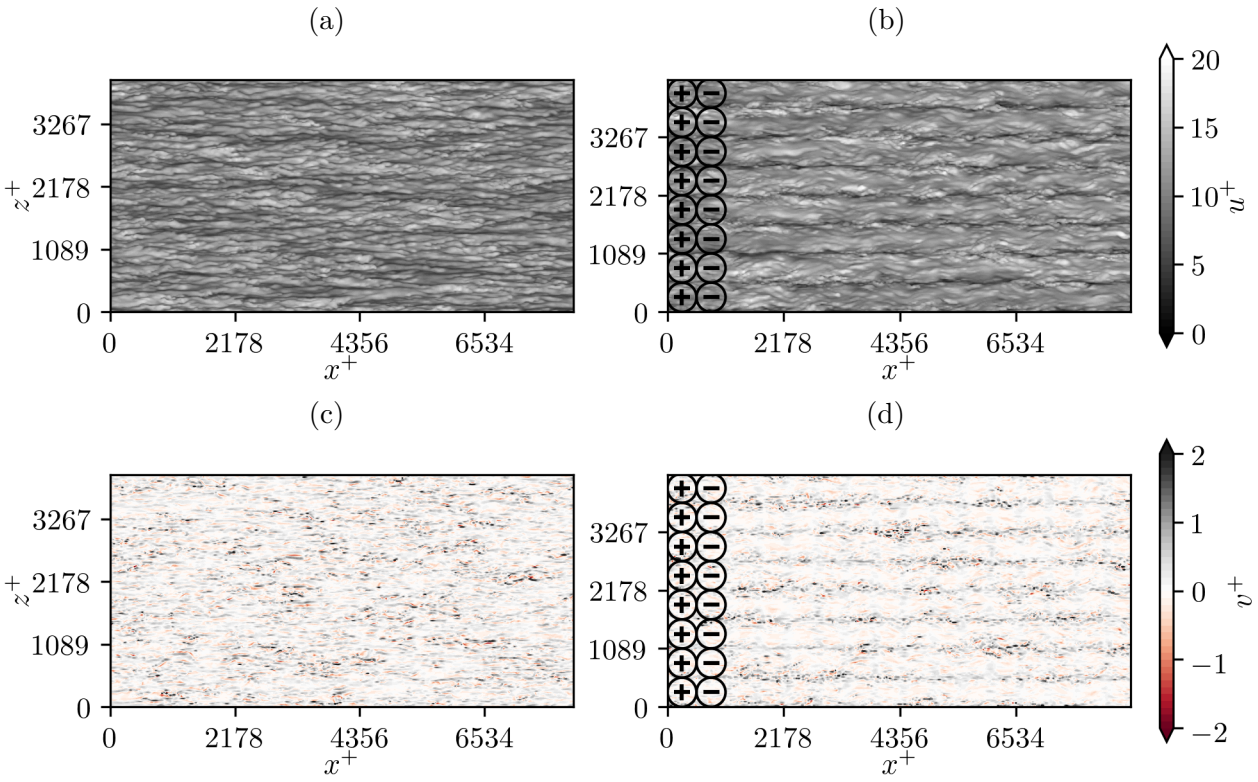

Figure 4.34: Comparison of instantaneous u^+(a),(b) and v^+(c),(d) visualization on a wall-parallel plane at y^+=12, for cases S550 and D550_5.

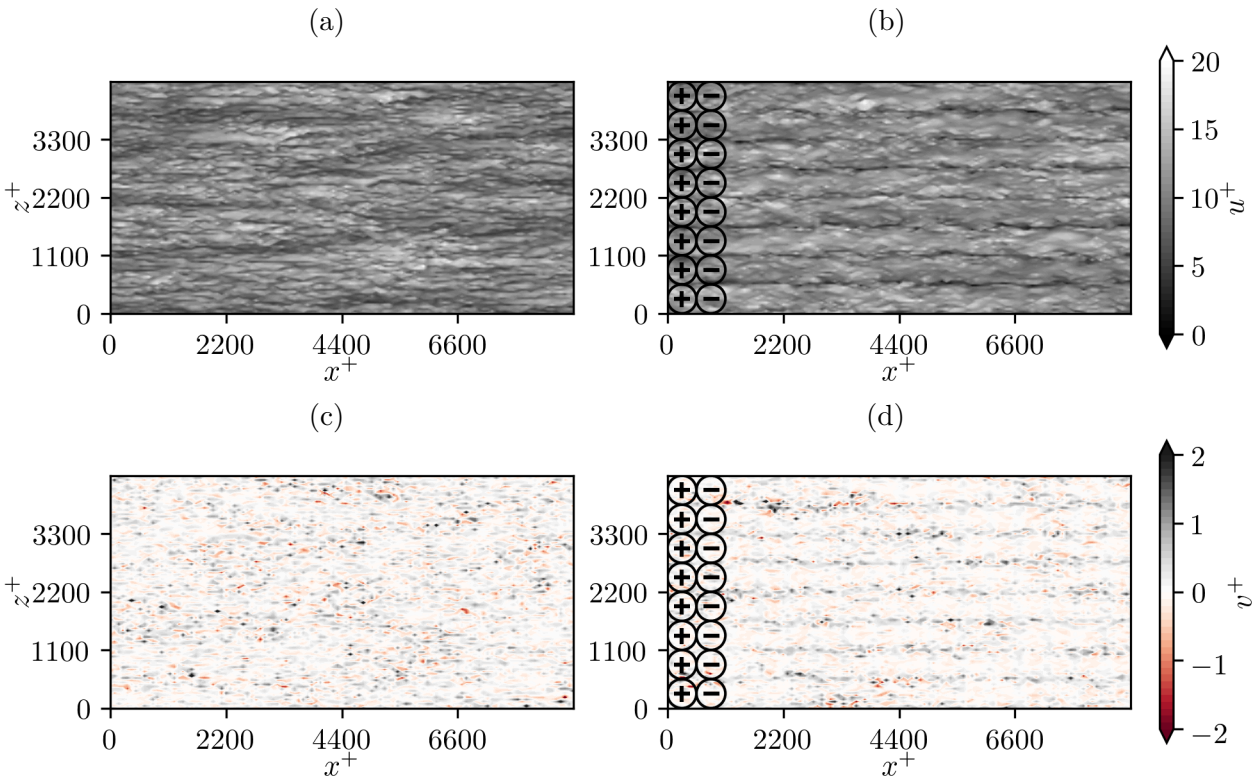

Figure 4.35: Comparison of instantaneous u^+(a),(b) and v^+(c),(d) visualization on a wall-parallel plane at y^+=12, for cases S1000 and D1000_5.

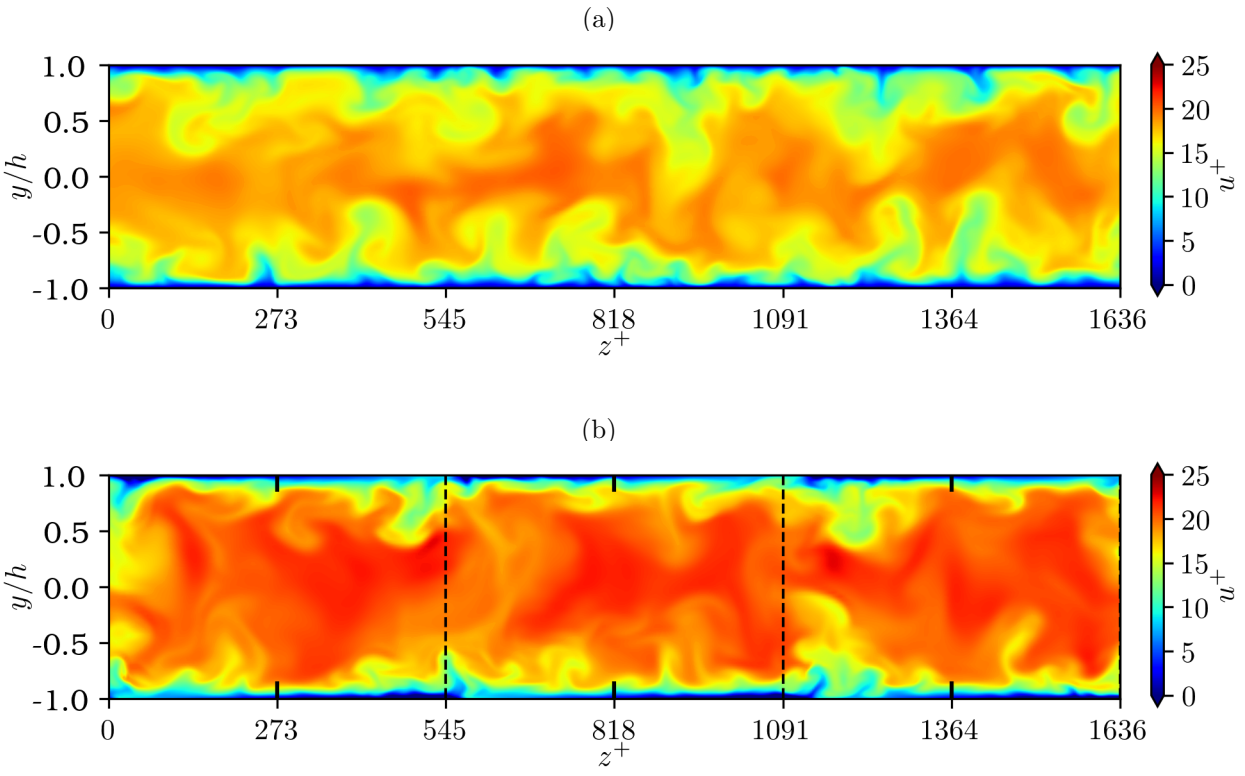

Figure 4.36: Comparison of instantaneous u^+ visualization on lateral $z-y$ planes for case S180 (a) and D180_5 (b).

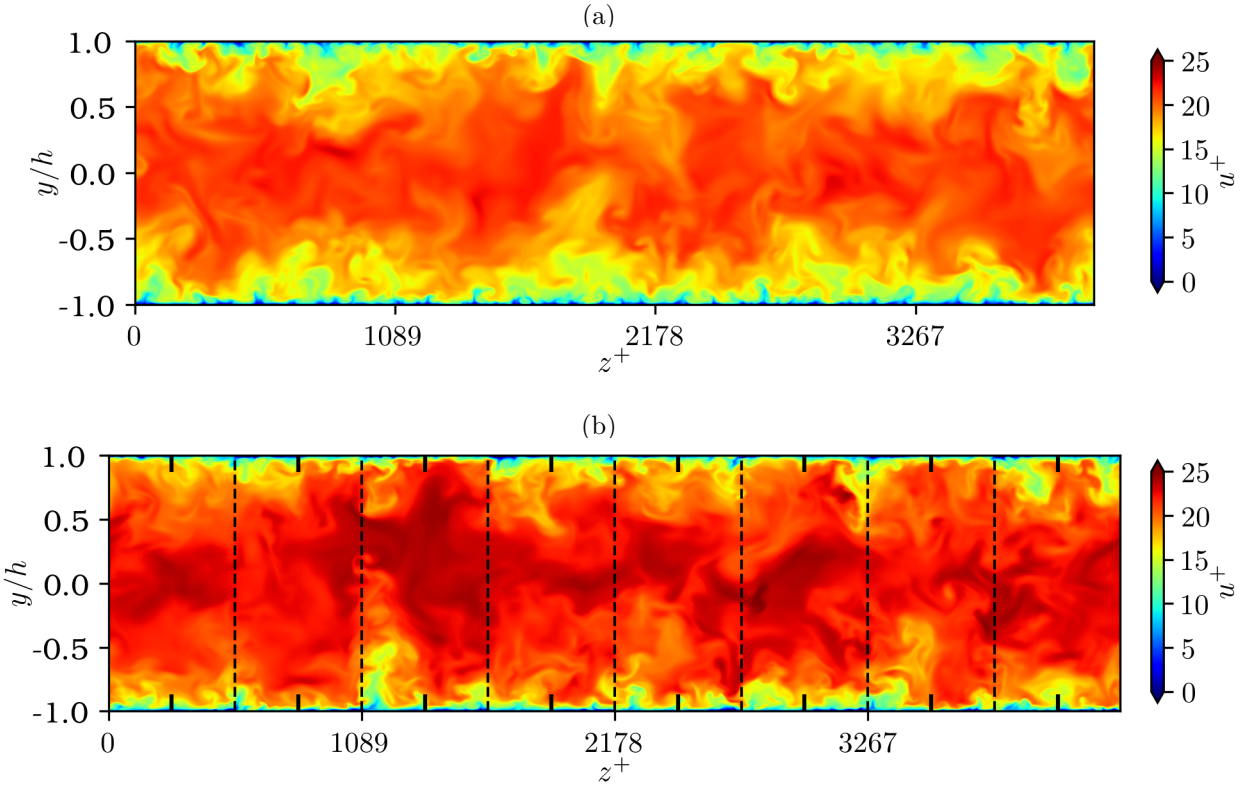

Figure 4.37: Comparison of instantaneous u^+ visualization on lateral $z-y$ planes for case S550 (a) and D550_5 (b).

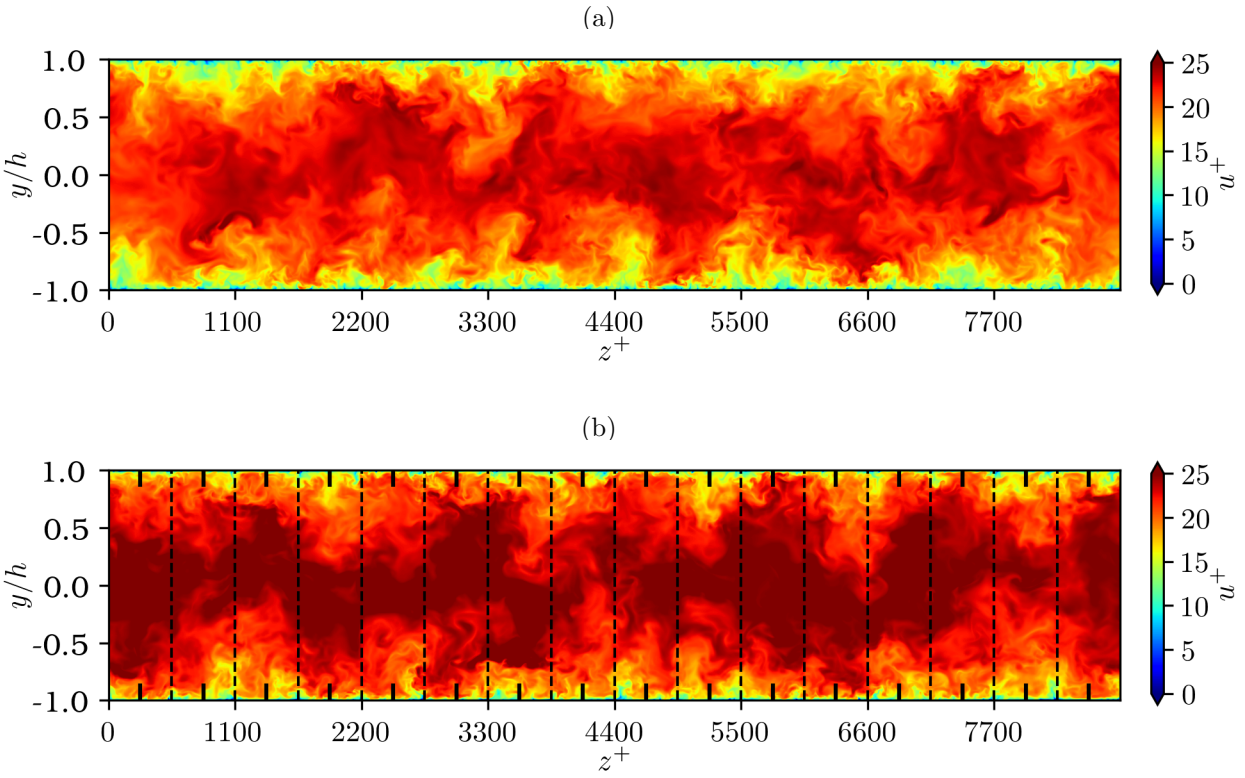

Figure 4.38: Comparison of instantaneous u^+ visualization on lateral $z-y$ planes for case S1000 (a) and D1000_5 (b).

4.7.3 Longitudinal x-y slices

The disc velocity distribution analysis, performed in Section 4.4, as well as the instantaneous field visualizations on $x-z$ planes have highlighted a clear difference in the flow between the disc center and the interface between spanwise adjacent discs. The following Figures will show instantaneous longitudinal $x-y$ slices on planes BB and CC, for the disc cases and their smooth wall counterparts.

Figure 4.39 displays the streamwise velocity distribution for case S180 and disc-on case D180_5. The difference in the instantaneous streamwise velocity between the smooth wall simulation, plane BB (passing through the disc center) and plane CC (passing through the disc edge) is clearly visible. The instantaneous velocity at plane BB shows small velocity fluctuations compared to the same quantity visualized on plane CC. This correlates to the inter-disc ejections caused by the sharp velocity discontinuity at the disc lateral edges. A further observation is that even on plane CC, where the turbulent activity is more intense, the center channel velocity is higher than the smooth wall simulation result. Furthermore, as it was seen for the lateral $z-y$ planes, the disc-on case has a higher center-channel velocity for the disc-on case.

Figure 4.40 shows planes BB and CC of case D550_5 compared against the longitudinal $x-y$ plane for the S550 case. The features observed are very similar to what was commented for the visualizations at $Re_\tau = 180$: a faster center channel region for the disc-on case, as well as faster flow in the near wall regions for plane BB, at the disc center. At the disc edge interface (plane CC), the near-wall region the flow appears slower than smooth-wall levels at some locations, however the center channel velocity is still visibly as fast as plane BB. The same quantity on the same planes is shown in Figure 4.41 for cases S1000 and D1000_5. The increase in center

channel velocity is clearly visible, however at this Re_τ the difference between plane BB and plane CC are not as clearly noticeable as before, and the two planes look fairly similar to each other.

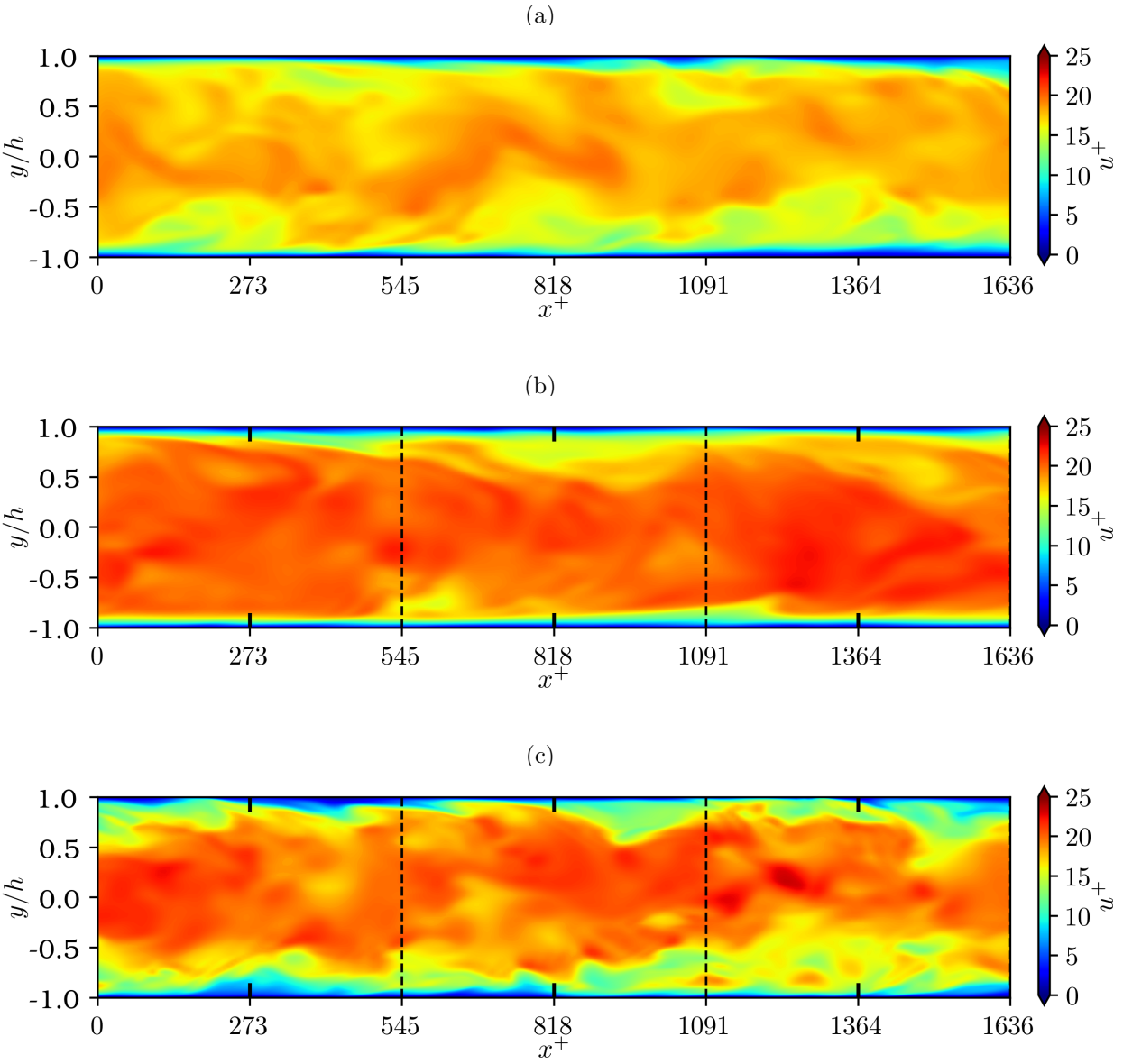

Figure 4.39: Comparison of instantaneous u^+ velocity visualization on longitudinal $x-y$ planes for cases S180 (a) and D180_5 taken through plane BB (b) and plane CC (c).

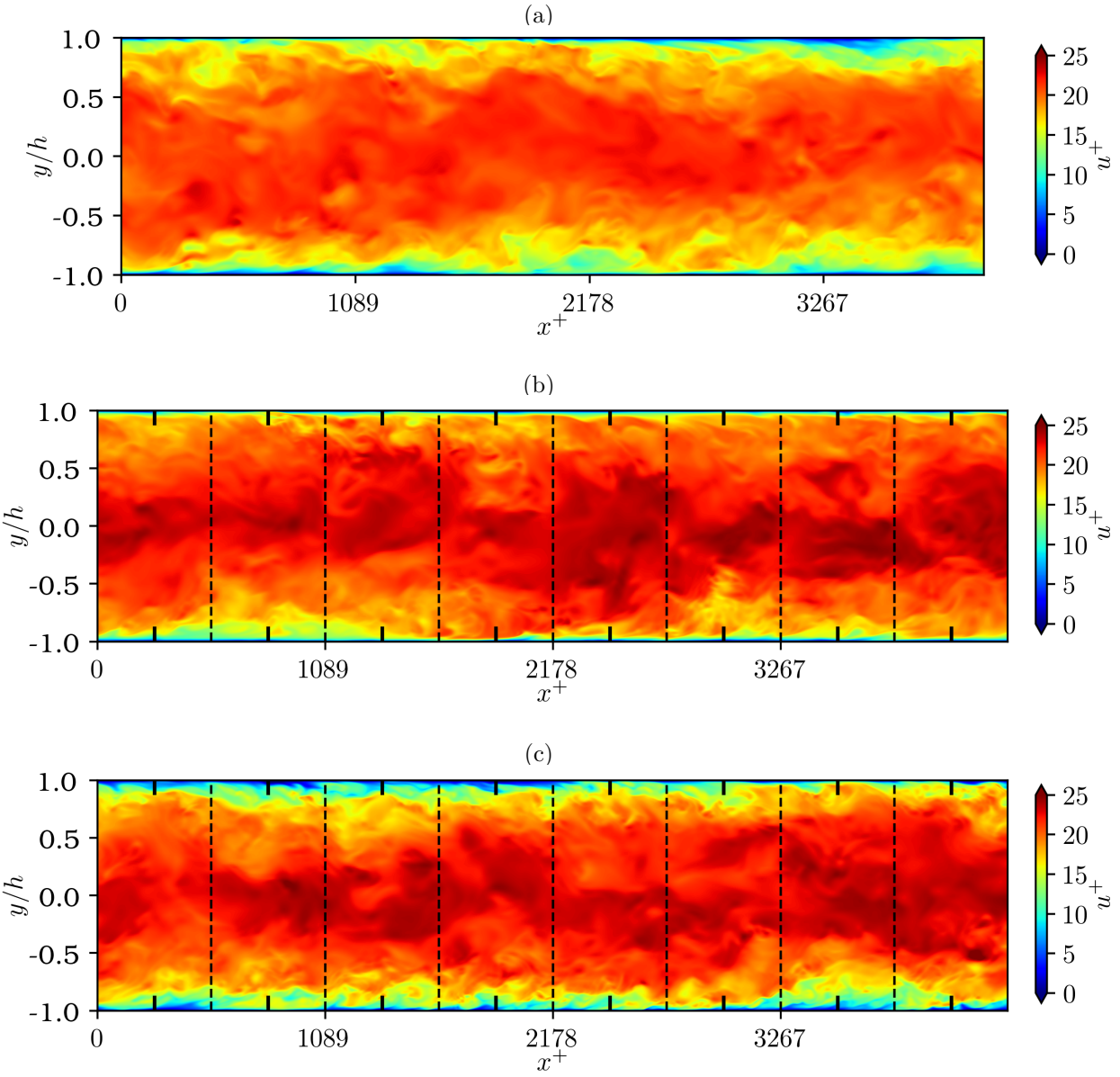

Figure 4.40: Comparison of instantaneous u^+ velocity visualization on longitudinal $x-y$ planes for cases S550 (a) and D550_5 taken through plane BB (b) and plane CC (c).

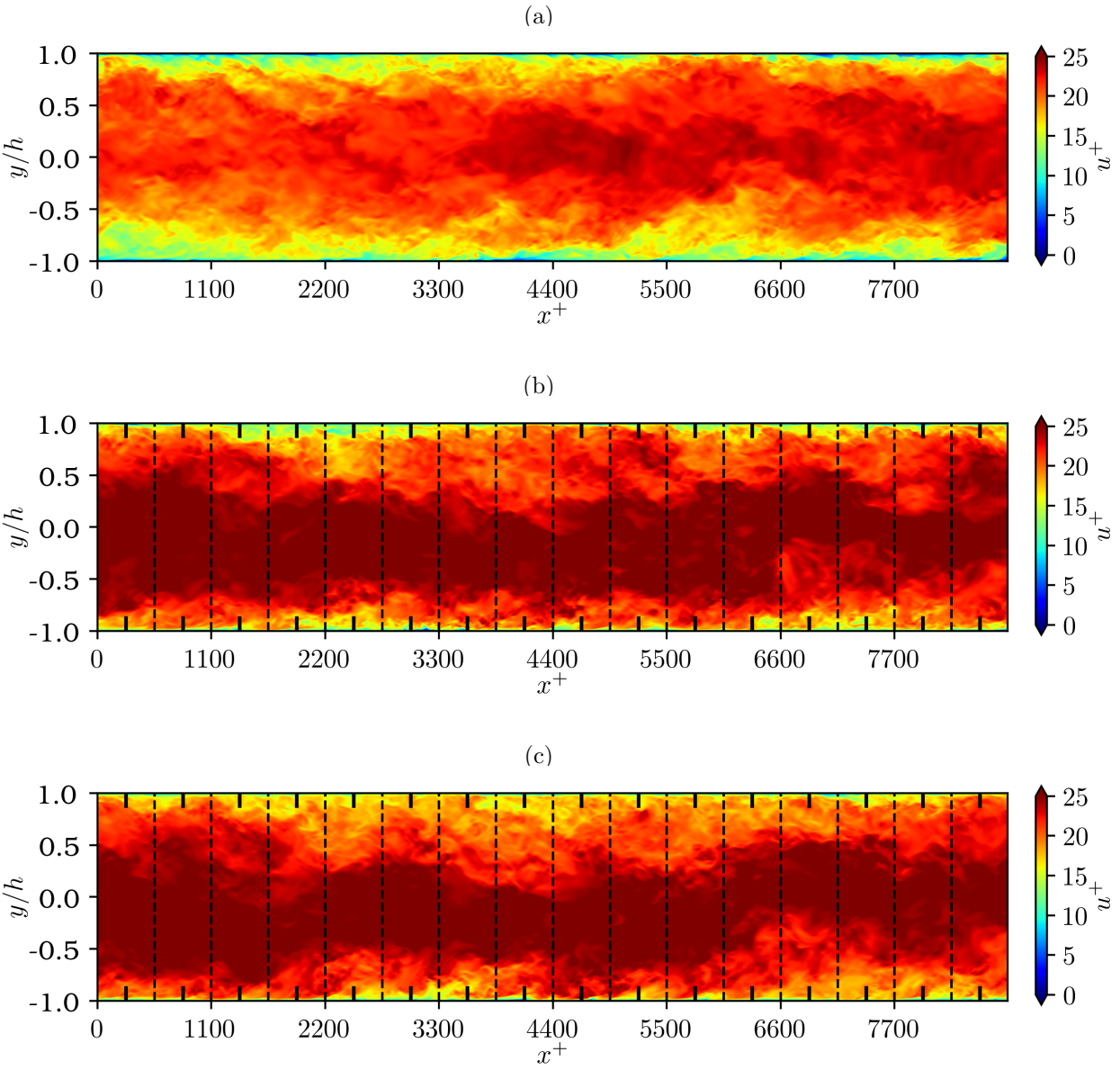

Figure 4.41: Comparison of instantaneous u^+ velocity visualization on longitudinal $x-y$ planes for cases S1000 (a) and D1000_5 taken through plane BB (b) and plane CC (c).

5

Conclusion and Recommendations

Skin-friction drag constitutes approximately half the total drag for a commercial aircraft, and even a small reduction could lead to industry-wide savings in the order of billions US Dollars per year, as well as reduction in CO2 emissions in the order of hundreds of million metric tonnes. Research on flow control techniques to achieve skin-friction drag reduction has been an active topic for several decades. Recent advancements were made in the field of rotating disc actuators for turbulent skin-friction drag reduction which have shown good drag reduction and power savings (Ricco & Hahn, 2013). The current state of the research on these actuators, however, is limited to computational studies at low friction Reynolds numbers ($Re_\tau = 180$), and many authors have highlighted the need for research in more representative conditions for real world applications.

This thesis project was created with the goal of analyzing the performance of rotating disc actuators at friction Reynolds numbers up to $Re_\tau = 1000$ with the use Direct Numerical Simulation. The work reported in this thesis pursues the following project objective:

"To investigate how the skin-friction drag reduction performance of rotating discs scale with increasing Reynolds number.

For this project, the following research questions have been pursued:

RQ1 How does the skin-friction drag reduction performance of rotating disc actuators change with increasing friction Reynolds number?

RQ2 How does the net power balance performance of rotating disc actuators change with increasing friction Reynolds number?

Disc actuators have been simulated using an incompressible turbulent channel flow solver previously used by Bernardini et al. (2014), modified to implement the disc actuators. Two combinations of viscous-scaled disc diameter and disc tip velocity have been investigated: $D^+ = 801$, $W^+ = 11$, and $D^+ = 546$, $W^+ = 10.5$. Simulations have been carried out at Re_τ=180, Re_τ=550 and Re_τ=1000. Due to limited computational resources, only the $D^+ = 546$, $W^+ = 10.5$ was simulated at Re_τ=1000. Validation of the code implementation shows agreement with reference smooth wall simulations from Hoyás and Jiménez (2006), as well as the reproductions of the simulations from Ricco and Hahn (2013).

As Re_τ increases the drag reduction performance is negatively affected, with a monotonic decrease of $\mathcal{DR}$ from 21.59% at Re_τ=180 to 16.01% at Re_τ=1000. Decomposition of the drag reduction into its turbulent, laminar and disc components via the use of the FIK identity has shown that the disc contribution $\mathcal{DR}_d$ is roughly independent of Re_τ, and has shown to be always detrimental. The negative trend of drag reduction was found to be primarily driven by the

decrease in the turbulent $\mathcal{DR}_t$ component with increasing Re_τ. The drag reduction mechanism is closely linked to the reduction of the turbulent stresses under the action of the disc actuators. With increasing Re_τ, the turbulent stresses are affected by the relative decrease in turbulent stresses compared to the total smooth wall stresses, as well as the slight strengthening of the inter-disc structures at higher Re_τ.

Time-averaged velocity bundle distribution in the wall-normal direction have shown that the disc influence extends to the center of the channel at Re_τ=180. This plays a role into the high actuator performance seen at low friction Reynolds number not only for the present study, but for the entire literature on disc actuators. At Re_τ=550 and higher, the local streamwise velocity profiles collapse onto the mean velocity profile in the region $y^+ \approx 400$ for both disc configurations tested. The limited influence of the discs within the channel at high Re_τ is a hint that the dependency of the disc performance on Re_τ at high friction Reynolds number will be lower. Data also suggest that that the drag variation becomes less dependent on the Reynolds number, as Re_τ increases and therefore DNS at higher Reynolds number could provide a more accurate estimate of the drag reduction achievable in flight conditions.

With increasing Re_τ, the net power balance performance is only lightly negatively affected, as the power spent to move the discs and the drag reduction degrade in a similar fashion. Of the two disc configurations tested, only one shows a positive net power balance amounting to $\approx 1.9\%$ at Re_τ=550, which is lower than the power saving/drag reduction offered by passive flow control methods (i.e. riblets) at the same Reynolds number. This is a major roadblock in the implementation of disc actuators in full scale, as passive methods offer similar levels of performance at reduced complexity.

This thesis project has been running in parallel with an experimental testing campaign in a wind-tunnel boundary layer environment, with a similar disc diameter and Re_τ. Although the disc layout was different, qualitative comparison of the turbulent Reynolds stresses on a wall-parallel plane taken at $y^+ = 70$ showed a good agreement, both in terms of flow topology and stress magnitude. This shows that the performance of the discs in computational domain can serve as a good indicator of their experimental counterpart.

A question still open is whether drag reduction and power balance performance scale in viscous or outer units. In this study, disc diameter and tip velocity were scaled in viscous units at higher friction Reynolds number. The consistent trend of drag reduction with increasing Re_τ is a strong hint that the optimal disc velocity and size do scale in viscous units. This is a further issue for practical implementation, since the optimal disc diameter for flight conditions would be in the order of 1mm (Ricco & Hahn, 2013), likely resulting in large manufacturing and maintenance costs, potentially higher than the economic savings from the implementation of the system.

5.1 Recommendations

This research work has shed a first light on the performance of disc actuators at friction Reynolds numbers above 180. The results have shown that the skin-friction drag reduction and power balance performance is positive also for Reynolds numbers higher than the current literature, however not sufficient to outperform passive methods. Here, a couple recommendations for future work are provided.

First, expanding the scope of the dataset would be instrumental in providing more conclusive evidence on the trends of drag reduction and net power balance performance. To do so, a nu-

merical simulation of case yielding positive net power balance should be performed at Re_τ=1000 too. In addition to this, simulations at intermediate Reynolds number values, such as Re_τ=750 can further help to understand the evolution of the performance parameters.

Furthermore, past studies on disc actuator variants such as ring actuators (Olivucci et al., 2019) and studies on different spatial layouts of discs (Wise et al., 2014) have shown that such variants have better drag reduction and net power balance performance than the disc actuators examined in this thesis work. Performing numerical simulations of these actuators at high Re_τ can lead to better performances, as it was shown for the two disc configurations that there are not drastic changes in performance from Re_τ=180 to Re_τ=1000.

The last recommendation is to perform numerical simulations of disc actuators scaled in outer units (i.e. keeping a constant D/δ and W/u_b while increasing Re_τ), such that with those results it will be possible to obtain conclusive evidence on whether disc actuator performance does indeed scales in viscous units.

References

Akhavan, R., Jung, W., & Mangiavacchi, N. (1993). Control of wall turbulence by high frequency spanwise oscillations [AIAA paper 93-3282]. *3rd shear flow conference*.

Baron, A., & Quadrio, M. (1995). Turbulent drag reduction by spanwise wall oscillations. *Appl. Sci. Res.*, *55*, 311–326.

Bechert, D., & Reif, W. (1985). On the drag reduction of the shark skin. *23rd aerospace sciences meeting*.

Bechert, D. W., & Hage., W. (2006). Drag reduction with riblets in nature and engineering. *WIT Trans. State Art Sci. and Eng.*, *4*, 457–469.

Benschop, H., & Breugem, W.-P. (2017). Drag reduction by herringbone riblet texture in direct numerical simulations of turbulent channel flow. *J. Turbul.*, *18*(8), 717–759.

Bernardini, M., Pirozzoli, S., & Orlandi, P. (2014). Velocity statistics in turbulent channel flow up to $re_\tau = 4000$. *J. Fluid Mech.*, *742*, 171–191.

Choi, H., Moin, P., & Kim, J. (1994). Active turbulence control for drag reduction in wall-bounded flows. *J. Fluid Mech.*, *262*, 75–110.

Choi, K., & Graham, M. (1998). Drag reduction of turbulent pipe flows by circular-wall oscillation. *Phys. Fluids*, *10*(1), 7–9.

Choi, K.-S., DeBisschop, J., & Clayton, B. (1998). Turbulent boundary-layer control by means of spanwise-wall oscillation. *AIAA J.*, *36*(7), 1157–1163.

Cousteix, J. (2003). Aircraft aerodynamic boundary layers. In R. A. Meyers (Ed.), *Encyclopedia of physical science and technology (third edition)* (Third Edition, pp. 301–317). Academic Press.

European Commission, D.-G. f. R., & Innovation. (2021). Horizon europe strategic plan (2021 – 2024).

Gad-el-Hak, M. (2000). *Flow control: Passive, active, and reactive flow management*. Cambridge University Press.

García-Mayoral, R., & Jiménez, J. (2011). Drag reduction by riblets. *Philos. Trans. R. Soc. London, Ser. A*, *369*(1940), 1412–1427.

Gatti, D., Deyn, L., Forooghi, P., & Frohnapfel, B. (2020). Do riblets exhibit fully rough behaviour? *Exp. Fluids*, *61*.

Harlow, F. H., & Welch, J. E. (1965). Numerical calculation of time-dependent viscous incompressible flow of fluid with free surface. *Phys. Fluids*, *8*(12), 2182–2189.

Hoyás, S., & Jiménez, J. (2006). Scaling of the velocity fluctuations in turbulent channels up to re_τ=2003. *Phys. Fluids*, *18*(1), 011702.

IATA. (2019). Iata industry statistics fact sheet 2019 [Retrieved on 10/2020]. https://www.iata.org/en/iata-repository/publications/economic-reports/airline-industry-economic-performance-june-2020-data-tables/

ICAO. (2019). 2019 environmental report, aviation and environment [Retrieved on 04/2021]. https://www.icao.int/environmental-protection/Documents/ICAO-ENV-Report2019-F1-WEB%5C%20(1).pdf

Jung, W. J., Mangiavacchi, N., & Akhavan, R. (1992). Suppression of turbulence in wall-bounded flows by high-frequency spanwise oscillations. *Phys. Fluids A: Fluid Dynamics*, *4*(8), 1605–1607.

Kaoru, I., Yuji, S., & Nobuhide, K. (2002). Reynolds number effect on wall turbulence: Toward effective feedback control. *Int. J. Heat Fluid*, *23*(5), 678–689.

Karniadakis, G., & Choi, K.-S. (2003). Mechanisms on transverse motions in turbulent wall flows. *Annu. Rev. Fluid Mech.*, *35*(1), 45–62.

Keefe, L. (1998). Method and apparatus for reducing the drag of flows over surfaces. *U.S. Patent 5,803,409*.

Ketut, I., Utama, I. K., Nugroho, B., Chin, C., Lukman, M., Hakim, M., Prasetyo, F., Yusuf, M., Suastika, K., Monty, J., Hutchins, N., & Ganapathisubramani, B. (2017). A study of skin friction-drag from realistic roughness of a freshly cleaned and painted ship hull.

Luchini, P., Manzo, F., & Pozzi, A. (1991). Resistance of a grooved surface to parallel flow and cross-flow. *J. Fluid Mech.*, *228*, 87–109.

Monty, J. P., Dogan, E., Hanson, R., Scardino, A. J., Ganapathisubramani, B., & Hutchins, N. (2016). An assessment of the ship drag penalty arising from light calcareous tubeworm fouling. *Biofouling*, *32*(4), 451–464.

Olivucci, P., Ricco, P., & Aghdam, S. K. (2019). Turbulent drag reduction by rotating rings and wall-distributed actuation. *Phys. Rev. Fluids*, *4*, 093904.

Perlin, M., Dowling, D. R., & Ceccio, S. L. (2016). Freeman Scholar Review: Passive and Active Skin-Friction Drag Reduction in Turbulent Boundary Layers [091104]. *J. Fluids Eng.*, *138*(9).

Pope, S. B. (2000). *Turbulent flows*. Cambridge University Press.

Quadrio, M. (2004). Critical assessment of turbulent drag reduction through spanwise wall oscillations. *J. Fluid Mech.*, *521*, 251–271.

Raayai-Ardakani, S., & McKinley, G. H. (2019). Geometric optimization of riblet-textured surfaces for drag reduction in laminar boundary layer flows. *Phys. Fluids*, *31*(5), 053601.

Ricco, P. (2004). Modification of near-wall turbulence due to spanwise wall oscillations. *J. Turbul.*, *5*, N24.

Ricco, P., & Hahn, S. (2013). Turbulent drag reduction through rotating discs. *J. Fluid Mech.*, *722*, 267–290.

Ricco, P., & Quadrio, M. (2008). Wall-oscillation conditions for drag reduction in turbulent channel flow. *Int. J. Heat Fluid*, *29*(4), 891–902.

Robert, J. (1992). *Drag reduction: An industrial challenge*. Defense Technical Information Center.

Robinson, S., Kline, S., & Spalart, P. (1992). Quasi-coherent structures in turbulent boundary layers.

Sasamori, M., Mamori, H., Iwamoto, K., & Murata, A. (2014). Experimental study on drag-reduction effect due to sinusoidal riblets in turbulent channel flow. *Exp. Fluids*, *55*.

Schrauf, G. (2006). Key aerodynamic technologies for aircraft performance improvement.

Sem, J. (2021). Rotating discs for turbulent drag reduction: An experimental study. *Delft University of Technology, Delft, The Netherlands*.

Szodruch, J. (1991). Viscous drag reduction on transport aircraft. *29th aerospace sciences meeting*.

Viswanath, P. (2002). Aircraft viscous drag reduction using riblets. *Prog. Aerosp. Sci.*, *38*(6), 571–600.

Walsh, M., & Lindemann, A. (1984). Optimization and application of riblets for turbulent drag reduction. *22nd aerospace sciences meeting*.

Wise, D., Alvarenga, C., & Ricco, P. (2014). Spinning out of control: Wall turbulence over rotating discs. *Phys. Fluids*, *26*, 125107.

Wise, D. J., Olivucci, P., & Ricco, P. (2018). Turbulent drag reduction through oscillating discs – corrigendum. *J. Fluid Mech.*, *856*, 1064–1066.

Wise, D. J., & Ricco, P. (2014). Turbulent drag reduction through oscillating discs. *J. Fluid Mech.*, *746*, 536–564.

Zhou, D., & Ball, K. (2008). Turbulent drag reduction by spanwise wall oscillations. *Int. J. Eng. A*, *21*, 85–104.